Enhanced Diffusion of Silicon and Boron in Thermal Oxides Formed on Silicon Substrates

2004

Shigeto Fukatsu

Abstract

Thermal silicon oxide (SiO_2) is the most important gate insulating material in the silicon (Si) MOSFET technology today. The thermal Si oxide also plays an important role in the development of next generation gate insulator materials (e.g., high dielectric constant materials) because it continues to exist as an interfacial layer between the new gate material and Si wafer. The improvement of MOSFET performance has been achieved in the past by miniaturization. However, with the gate length reaching 100nm and below, it is becoming increasingly difficult to realize thinner gate insulators and smaller channel lengths while maintaining the normal state of device operation. Lack of a precise atomic level picture of thermal oxidation mechanisms is interfering with development of future nanoscale thermal oxides. A phenomenon such as diffusion of boron (B) from the top polycrystalline silicon gate electrode to the Si channel region through SiO_2 gate insulator is smearing the well-defined channel in Si.

In order to overcome these problems, experimental investigations of Si and B diffusions in thermal SiO_2 formed on Si wafers followed by complete numerical modeling of the data were performed in the present study. The precise knowledge of Si self-diffusion in SiO_2 is indispensable for the development of future gate insulator architecture. Understanding of the B diffusion in SiO_2 is important to prevent the smearing of the channel region. In this study, ^{30}Si stable isotopes and B impurities embedded in isotopically enriched $^{28}SiO_2$ were employed as diffusion markers, and the diffusion of Si and B in SiO_2 as a function of the diffusion annealing temperature, annealing time, and thermal oxide thickness were investigated with and without surface silicon nitride (Si_3N_4) layers placed on the SiO_2 films. The depth profiles of ^{30}Si and B before and after annealing were determined by secondary ion mass spectrometry (SIMS). As a result, Si diffusivity obtained without surface nitride does not depend on the thickness of the SiO_2 film and agrees with the previously reported value of Si diffusivity in the bulk quartz. Such Si diffusivity remains the same for a variety of oxygen partial pressures in the annealing atmosphere, when there is no nitride layer on the top. On the other hand, when the nitride layer is placed, the Si diffusivity was found to increase as the thickness of the SiO_2 film is reduced. In order to understand this phenomenon quantitatively, we proposed a new picture in which SiO molecules generated at the SiO_2/Si interface due to $SiO_2+Si \rightarrow 2SiO$ reaction diffuse into the SiO_2 layer and enhance the Si diffusivity. Numerical simulations conducted based

on this model for our variety of experimental conditions yield very good quantitative agreement with the experimental results, supporting the hypothesis used to developed the model. Similar experimental results were obtained for boron diffusion in SiO_2 depending on the presence of the surface nitride layer, and the model assuming SiO enhancing the diffusion of B in SiO_2 reproduce our experimental results quantitatively.

In summary, we have performed experiments probing Si and B diffusion in SiO_2 formed thermally on Si wafers, and discovered that SiO molecules generated at the SiO_2/Si interface enhanced the Si and B diffusion when the nitride cap was placed. A unified mathematical model describing the correlated diffusion of Si and B developed in this study should be incorporated in the next generation Si process simulation software in order to increase the precision of the simulated outcome. It will be also of great interest in the future to develop new nanoscale Si fabrication technique utilizing the role of SiO defects.

Acknowledgement

First of all, I would like to express my sincere gratitude to my research advisor Prof. K. M. Itoh for his sincere guidance, helpful suggestions, and substantial supports, which were certainly the most essential help throughout this work.

I am grateful to Dr. M. Uematsu of NTT Basic Research Laboratories for kind supports and guidance. I have benefited from his keen physical insight and open manner of sharing knowledge.

I would like to extend many appreciations to Prof. E. Ohta, Prof. Y. Fujitani, and Prof. H. Imai for their careful review of this manuscript.

I would like to thank Prof. K. Shiraishi, Dr. H. Kageshima, Dr. A. Fujiwara, Dr. K. Nishiguchi, Prof. Y. Takahashi, and Dr. H. Inokawa for their helpful supports, suggestions, and discussions. They supported my work at NTT basic research laboratories in many ways.

I also learned a lot in discussions with Prof. U. Gösele, Prof. K. Yamada, and Prof. E. E. Haller.

I would like to extend appreciations to Prof. Y. Shiraki and Prof. K. Nakagawa. They accepted me to perform experiments in Prof. Shiraki's group of the University of Tokyo. I acknowledge Dr. T. Ueno, Dr. M. Miura, Dr. K. Kawaguchi, Dr. T. Irisawa, Dr. K. Odaira, H. Miura, K. Sawano, S. Tokumitsu, and S. Otake, of Shiraki's group, for their kind support and encouragement.

I thank A. Takano for SIMS measurement.

I acknowledge A. Fujimoto and T. Mitani for TEM measurements, SIMS measurements, and their kind support.

I acknowledge kind supports by members in Prof. Itoh's research group: Dr. T. Sekiguchi, Dr. K. Morita, Dr. J. Kato, T. Arai, K. Takyu, T. Morita, Y. K. Kato, T. Itoh, A. Kurokawa, Z. Miyazaki, T. Ishikawa, E. Abe, T. Takahashi, T. Kojima, K. Kojima, T. Yamada, R. Nebashi, T. Ohya, Y. Matsuki, Y. Shimizu, S. Yoshida, D. Tsurumi, M. Tsuchiya, and many others. The present work would not have been possible without their generous help.

Finally I would like to extend my deepest appreciation to my family for their warm support along the way.

Contents

Chapter 1

Introduction

The progress of silicon technology has enabled ultralarge-scale integration (ULSI) to the point that one integrated circuit (IC) chip contains over 10 million transistors, resistors, and capacitors. With the ULSI technology, the price of electronic products has decreased while enhancing the functionality and performance. There are two major types of silicon-based transistors: the metal oxide semiconductor field effect transistor (MOSFET) and bipolar transistor. Because of its advantages in device miniaturization, low power consumption, and high yield, the sales volume of the Si MOSFET based ICs has increased steadily and in 2000 occupied ∼90% of all ICs sold worldwide.

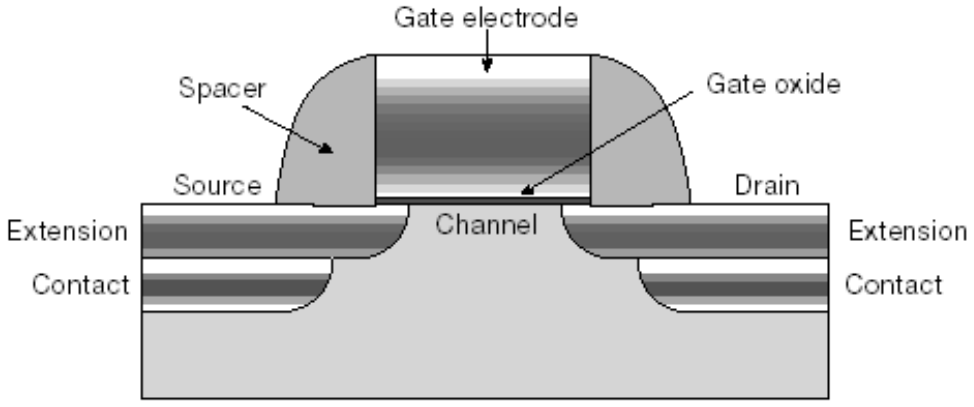

Figure 1.1: The schematic view of MOS structure [1]. The gate electrode is usually highly boron doped poly silicon.

During fabrication process of MOSFET, silicon dioxides (SiO_2) play various important roles. The typical roles of SiO_2 are:

1. mask against implantation or diffusion of dopant into silicon
2. passivation of surfaces,
3. isolation of devices,
4. gate insulators in MOS structures, and
5. electrical isolation of multi-level metallization systems.

There are several techniques to form SiO_2, e.g., thermal oxidation, wet anodization, chemical vapor deposition, and plasma oxidation. At the heart of MOS devices the thermally grown SiO_2 gate insulator forms a nearly ideal interface with the underlying silicon substrate. Therefore, the thermally grown SiO_2 is one of the most important materials for Si semiconductor devices. Understanding of Si self-diffusion mechanism in SiO_2 is also essential phenomenon for the investigation of the oxide growth mechanism [2, 3, 4].

As mentioned above, SiO_2 is used for the mask against diffusion of dopant. In addition, during high temperature processing, boron can diffuse out of the doped polycrystalline-Si gate electrodes, through the thin gate dielectric, and into the substrate, causing a shift in the threshold and flat-band voltages of the device [5, 6, 7]. Therefore, understanding and control of diffusion phenomena in SiO_2 are important for ULSI technology.

With the decreasing device dimension, the thickness of the gate oxide must be reduced. It is intuitive that an influence of the interface between Si and SiO_2 on various phenomena in the oxide would become more significant with the reduction of the SiO_2 thickness. Diffusion phenomena in SiO_2 become more important as SiO_2 thickness decreases with scaling down of Si MOS devices. Very little attention has been paid to the influence of the Si/SiO_2 interface on diffusion in SiO_2. Table 1.1 shows the gate length and equivalent oxide thickness (EOT) in relation to the technology node.

The thickness of SiO_2 is now reaching 2 nm and concerns for the rise of the leakage current for thinner SiO_2 gate insulators are debated, while some argue that SiO_2 will continue to be the most useful gate insulating materials, many others now believe that higher permitivity (high-k) dielectrics should be explored as future gate insulators. The results presented in this thesis are of great importance directly for the future development of SiO_2 gate insulators, and indirectly for the research towards reliable high-k gate insulators. It is well known that a thin SiO_2 interfacial layer still exists between the Si

and high-k materials. Therefore, even for high-k gate dielectric research, understanding of diffusion in SiO_2 is important. Because the SiO_2 interfacial layer is less than 1 nm, the influence of the Si/SiO_2 interface on diffusion phenomena, which is the main focus of this thesis, should be significant in such a thin SiO_2 layers.

The objective of this thesis is to study diffusion of silicon and boron in thermally oxidized SiO_2. In particular, this work focuses on the effect of the Si/SiO_2 interface on diffusion of silicon and boron in SiO_2. This thesis is organized as follows.

Chapter 2 shows experimental procedure of this work, including fabrication procedures of samples employed in this study, details of thermal annealing process, and characterization techniques.

Chapter 3 presents an overview of diffusion in silicon and SiO_2.

In chapter 4, measurements of Si self-diffusion in SiO_2 under thermal equilibrium condition are described [9, 10]. Many studies of Si self-diffusion in SiO_2 had been conducted before this work [11, 12, 13, 14]. However, there is more than one order of magnitude difference among the reported values of Si self-diffusivity (D_{Si}^{SD}) [11, 12, 13, 14]. In order to solve this puzzle, we have employed $^{nat}SiO_2/^{28}SiO_2$ (^{nat}Si refers to Si with natural isotopic abundance) isotope heterostructure of 700 nm total thickness to probe directly Si self-diffusion using ^{30}Si stable isotopes as markers. It will be made clear in chapter 4 that the ^{30}Si diffusion in relatively thick SiO_2 ($\sim$700 nm) represents the intrinsic diffusivity under the equilibrium condition. Mathiot *et al.* commented of our experimental results that a small amount of oxygen in an annealing ambient might have retarded Si self-diffusion in SiO_2 [13]. In response, we have investigated Si self-diffusion in SiO_2 as a function of the oxygen partial pressure in an annealing ambient and shown unambiguously that partial pressure does not have an effect on Si self-diffusion [10].

Chapter 5 discusses the effect of the Si/SiO_2 interface on Si self-diffusion in SiO_2.

Table 1.1: Roadmap of technology node, gate length, and equivalent oxide thickness [8].

Year	2002	2005	2008	2011	2014
Technology node (nm)	130	100	70	50	35
Gate length (nm)	85	65	45	32	22
Equivalent oxide thickness* (nm)	1.5-1.9	1.0-1.5	0.8-1.2	0.6-0.8	0.2-0.6

*The capacitance density is specified as the equivalent thickness of a SiO_2 dielectric.

First, we investigate Si self-diffusion in $^{28}SiO_2$ in which ^{30}Si are implanted as a function of the thickness of $^{28}SiO_2$ using both sets of samples with and without SiN capping layers [15]. As a result, Si self-diffusion in SiO_2 depends significantly on the thickness of $^{28}SiO_2$ with the SiN cap but does not without the SiN cap. Specifically, the diffusion profiles of Si become broader as the thickness of the $^{28}SiO_2$ layer decreases. The dependence of Si self-diffusion on the SiO_2 thickness is discussed, and we show that it is due to the effect of the Si/SiO_2 interface. The mechanism is that SiO molecules, which are generated and diffuse into SiO_2, enhance Si self-diffusion in SiO_2. We show convincingly that this tendency is not caused by the implantation damage and/or the stress at the SiN/SiO_2 interface. Based on the experimental finding, we constructed a diffusion model that involves generation of SiO molecules at the SiO_2/Si interface, which enhance Si self-diffusion in SiO_2 at the vicinity of the interface [16]. Using this model, ^{30}Si diffusion profiles are simulated successfully [16]. Moreover, the discrepancies among the reported values of Si self-diffusivity [9, 11, 12, 13] can be explained by taking into account the dependence of Si self-diffusion on the distance from the interface [15]. In addition, using the $^{nat}SiO_2/^{28}SiO_2$ isotope heterostructures, which are different from ^{30}Si-implanted samples, we investigate Si self-diffusion as a function of the distance from the interface. Here we show experimentally that Si self-diffusion does not depend on the oxide thickness, but depends on the distance between ^{30}Si diffusion markers and the Si/SiO_2 interface [17].

Chapter 6 discusses diffusion of boron in SiO_2. This is the natural extension of Si self-diffusion studies of previous chapters, because it is of great interest to investigate the effect of SiO generated at the SiO_2/Si interface on foreign species such as boron. Boron diffusion in SiO_2 has been investigated extensively in the context of boron concentration dependence [18], the effect of fluorine on B diffusion [19], and the time dependence of B diffusion [20]. In parallel, mechanisms of B diffusion have been investigated [21, 22, 24, 23]. For thin gate oxides, it has been reported that B diffusion depends on the thickness of the oxide [25]. We show clearly this dependence by measuring the boron diffusion in 200-, 300-, and 650-nm-thick $^{28}SiO_2$ layers into which ^{30}Si and B were implanted [17, 26]. We develop simulation model for SiO enhanced boron diffusion, very similar to the one developed for Si self-diffusion in chapter 5. Our simulation agrees very well with the experimental results [26, 27].

Chapter 7 presents conclusions and future works.

Chapter 2

Experimental procedures

2.1 Sample preparation

2.1.1 $^{nat}SiO_2/^{28}SiO_2$ isotope heterostructure samples

$^{nat}SiO_2/^{28}SiO_2$ isotope heterostructures were used to investigate Si self-diffusion in SiO_2 under thermal equilibrium conditions. $^{nat}SiO_2$ is consists of natural Si isotopic abundance as shown in Table 2.1 while $^{28}SiO_2$ consists of isotopically enriched ^{28}Si, whose composition is also shown in Table 2.1. In order to monitor the movement of Si in SiO_2, ^{30}Si stable isotopes diffusing from $^{nat}SiO_2$ to $^{28}SiO_2$ were used as diffusion markers.

Isotopically enriched ^{28}Si single crystal epilayers of 800 nm thickness grown by chemical vapor deposition (CVD) on 4-inch highly resistive Si wafers have been provided by Isonics Corp., Colorado, USA. The isotope composition of the ^{28}Si epilayer measured by secondary ion mass spectroscopy (SIMS) is ^{28}Si (99.924%), ^{29}Si(0.073%), and ^{30}Si(0.003%), as summarized in Table 2.1. The ^{28}Si surface of the epilayer was thermally oxidized in dry O_2 at 1100°C for 20 h to form 650 nm thick $^{28}SiO_2$. Subsequently, about 50 nm thick $^{nat}SiO_2$ was deposited on top of the $^{28}SiO_2$ film by low-pressure chemical vapor deposition

Table 2.1: Isotope composition of ^{28}Si epilayer

	^{28}Si	^{29}Si	^{30}Si
^{28}Si epilayer	99.924 %	0.073 %	0.003 %
^{nat}Si	92.2 %	4.7 %	3.1 %

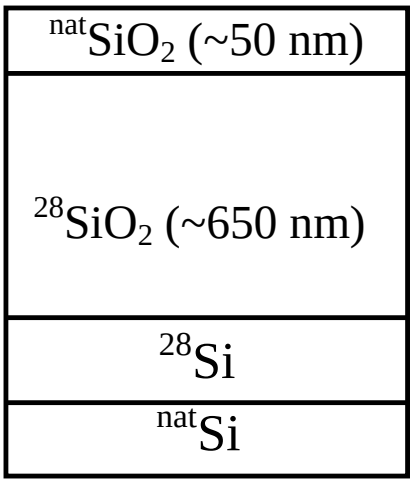

Figure 2.1: The structure of a $^{nat}SiO_2/^{28}SiO_2$ isotope heterostructure

(LPCVD) using tetraethoxysilane (TEOS) at 700°C. The completed structure is shown in Fig. 2.1.

After diffusion annealing, the ^{30}Si profiles, which became broader , were measured by SIMS.

2.1.2 ^{30}Si-implanted samples

In order to investigate the effect of a surface SiN layer and SiO_2 thickness on Si self-diffusion in SiO_2, ^{30}Si-implanted into $^{28}SiO_2$ layers of 200, 300, and 650 nm thick with and without the SiN layer were prepared as follows. Isotopically enriched ^{28}Si single crystal epilayers of 800-nm thickness grown by chemical vapor deposition (CVD) on 4-inch highly resistive Si wafers were obtained from Isonics Corp., Colorado, USA, as mentioned before. The ^{28}Si surface of the epilayer was thermally oxidized in dry O_2 at 1100 °C to form $^{28}SiO_2$ of the thicknesses 200, 300, and 650 nm. After these samples were cut into quarter pieces, these pieces were dipped in the solution consisted of H_2O_2 : H_2SO_4 at 1 : 3 for 5 min, followed by 5-min rinse using ion-exchanged water. Each piece was attached to a 4-inch Si substrate (which serves as a holder during implantation) using an electron wax, and was implanted with ^{30}Si at 50 keV to a dose of 1×10^{14} cm^{-2} or 2×10^{15} cm^{-2}. Because the implantation was conducted simultaneously for every piece, the depth profiles of implanted ^{30}Si were the same for all samples with various thickness of $^{28}SiO_2$ layers.

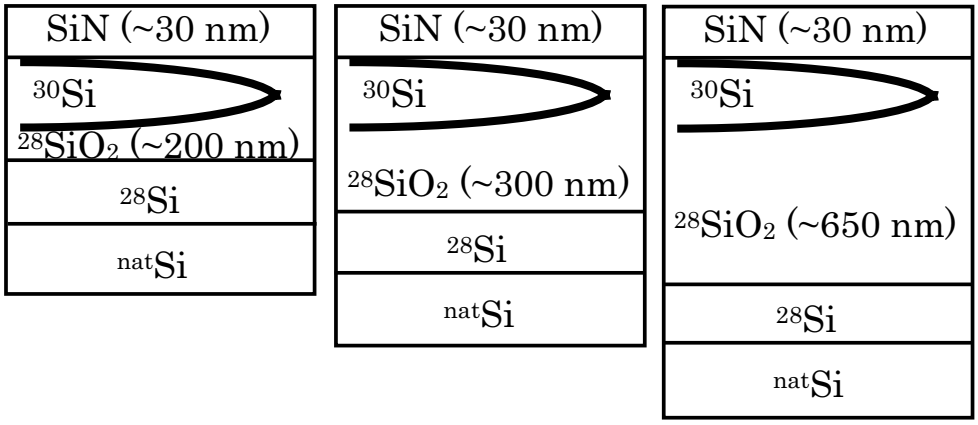

Figure 2.2: Structures of ^{30}Si-implanted $^{28}SiO_2$ with SiN capping layers of ∼30-nm thickness. The thicknesses of $^{28}SiO_2$ layers are 200, 300, and 650 nm in order to investigate an effect of the Si/SiO_2 interface on diffusion of implanted ^{30}Si.

The quarter wafer samples were cut further into half, 1/8 size pieces, and each one of half pieces was capped with a ∼30 nm-thick silicon nitride layer by rf magnetron sputtering for protection of the SiO_2 layer from oxygen during annealing. The ^{30}Si-implanted samples with and without silicon nitride were cut into 5×5 mm^2 pieces for the heat treatment. The final structures, i.e., the silicon-nitride-capped samples, are shown in Fig. 2.2.

2.1.3 Isotope heterostructures with a constant total oxide thickness

This set of samples was used for investigating the influence of Si/SiO interfaces on Si self-diffusion in SiO_2. The $^{nat}SiO_2/^{28}SiO_2$ isotope heterostructures were grown in a manner similar to that described in § 2.1.1. ^{28}Si epilayers were thermally oxidized in dry O_2 to form $^{28}SiO_2$ of 200-, 300-, and 650-nm thickness. $^{nat}SiO_2$ of 550-, 450-, and 100-nm thickness were deposited on the surfaces of $^{28}SiO_2$ of 200-, 300-, and 650-nm thickness, respectively, by LPCVD using TEOS at 700°C. Each sample had the same total SiO_2 thickness (∼750 nm). Finally, a 30-nm-thick silicon nitride layer was deposited on top of the samples by means of rf magnetron sputtering, as shown in Fig. 2.3.

In these samples, the total thicknesses of $^{28}SiO_2$ were same. Therefore, we can investigate purely the effect of the distance between ^{30}Si diffusers and the $^{28}SiO_2/^{28}$Si interface on Si self-diffusion in SiO_2 without influence of the total oxide thickness.

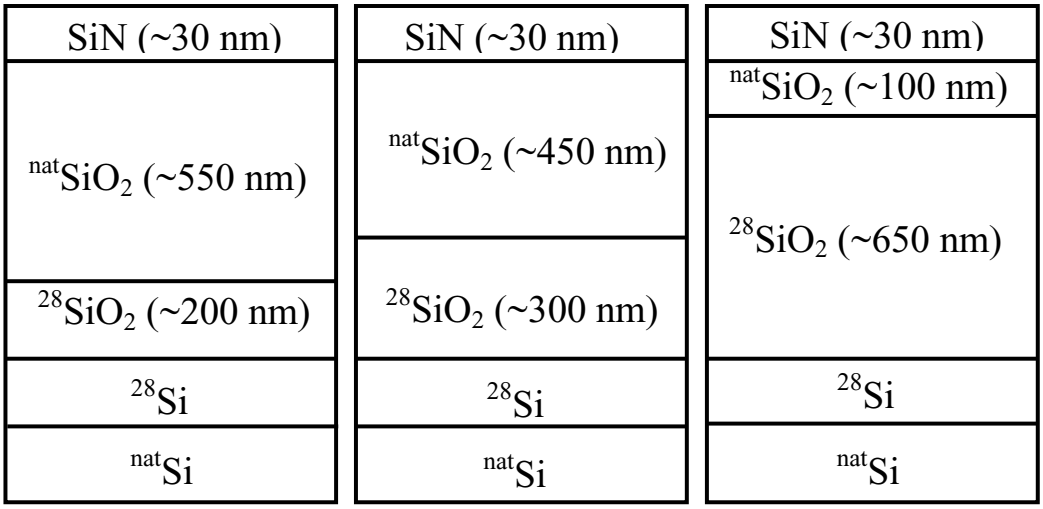

(a) (b) (c)

Figure 2.3: Schematics of $^{nat}SiO_2/^{28}SiO_2$ isotope heterostructures. The distance between the $^{nat}SiO_2/^{28}SiO_2$ and $^{28}SiO_2/^{28}Si$ interface in each sample is different from each other while the total oxide thicknesses are constant.

2.1.4 ^{30}Si and B co-implanted samples

In order to investigate the effect of Si/SiO_2 interfaces on boron diffusion in SiO_2 , B and ^{30}Si implanted samples were prepared as follows. The thermally grown $^{28}SiO_2$ layers of 200, 300, and 650 nm thicknesses were implanted with ^{30}Si at 50 keV to a dose of 2×10^{15} cm^{-2} and capped with a ∼30-nm-thick silicon nitride layer by rf magnetron sputtering. Subsequently, the samples were implanted with ^{11}B at 25 keV to a dose of 5×10^{13} cm^{-2}. The final structures are shown in Fig. 2.4.

2.2 Annealing procedures

Annealing procedures employed in this study is as follow.

The samples grown on the 4-inch wafer were cut into 5×5 mm^2 pieces, which enables us to use the same structures for different annealing conditions. Each piece was dipped in the solution consisted of H_2O_2 : H_2SO_4 at 1 : 3 for 5 min, followed by 5-min rinse using ion-exchanged water. This process was repeated twice for each sample. After drying, samples were placed on a quartz boat at the exit of a quartz tube located in a resistive

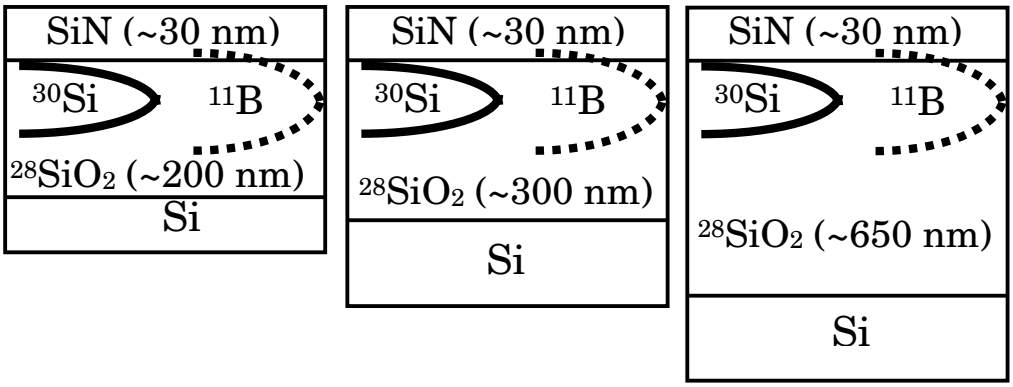

Figure 2.4: Sample structures of ^{30}Si- and B-implanted $^{28}SiO_2$ layers of 200, 300, and 650 nm thicknesses with SiN capping layers.

furnace. The furnace was prefired to stabilize at the target temperature. The boat was inserted into the quartz tube, where annealing ambient gas was flowing. Semiconductors processing grade quartz tubes and gas sources (argon and oxygen) were employed for maintaining the sample as clean as possible. After appropriate time of annealing, the boat was pulled to the edge of the quartz tube, whose temperature is room temperature. The sample temperature immediately went down to ∼100 °C in flowing annealing ambient gas after pulling.

2.2.1 Annealing apparatuses

Figure 2.5 shows a picture of a quartz boat located at the edge of the quartz tube. The quartz boat was equipped with a port for inserting a thermocouple in order to measure accurately the sample temperature during thermal annealing. A well-calibrated thermocouple located in the clean quartz port was placed right next to the sample. The temperature was monitored and recorded automatically by PC throughout the course of annealing. The fluctuation of temperature was found to be less than ± 2°C.

Samples cut into 5×5 mm^2 and cleaned were put on the boat. In order to prevent air from flowing in, a quartz cap was placed at the exit of a quartz tube, through which an semiconductor processing grade annealing ambient gas was flowing.

Before annealing, the quartz tube and boat were dipped in the solution (HF : HNO_3

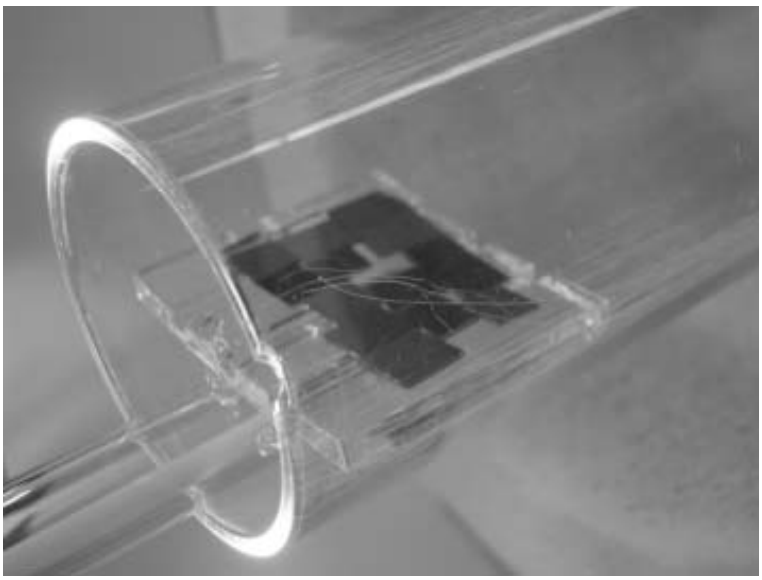

Figure 2.5: Picture of a quartz sample boat equipped with a port for inserting a thermocouple. The boat, on which samples cut into 5×5 mm^2 are put, is being inserted into the quartz tube.

= 1 : 3) for 5 min and were rinsed with ion-exchanged water for ∼10 min to keep them as clean as possible. Then, they were dried in flowing semiconductor processing gas at room temperature, followed by degassing at 1250 °C.

After many high temperature annealing cycles, devitrification of the sample holder took place, and caused discrepancy of measured values of the diffusivity. In order to prevent the error due to the devitrification of the quartz holder, we used the simple isotope heterostructure as the reference samples to check the influence of the holder.

Fig. 2.6 shows a resistive furnace which was used for the diffusion annealing. The furnace can provide maximum temperature of 1500 °C.

2.2.2 Annealing conditions

The duration of annealing (diffusion time) was chosen so that it leads to diffusion length 2 $\sqrt{Dt}$=10-20 nm in order to retain a plateau of diffusion profile of $^{nat}SiO_2/^{28}SiO_2$ isotope heterostructures in the $^{nat}SiO_2$ layer. For each temperature, two periods of diffusion time have been employed.

For the annealing ambient, flowing argon with 1% oxygen was used. The oxygen was

Figure 2.6: Resistive furnace employed in this work.

mixed into argon in order to prevent SiO_2 from decomposition, which tends to occur at higher temperatures and for lower oxygen partial pressures. This oxygen not only prevents decomposition but also oxidizes ^{28}Si at the interface $^{28}SiO_2/^{28}Si$ and forms additional $^{28}SiO_2$. In order to decrease the rate of oxidation, the least amount of oxygen, which turns out to be 1%[28], needed for SiO_2 to remain composed at 1300°C was chosen. Every time thermal annealing was conducted, a piece of Si substrate was annealed in the same furnace, and its oxide thickness was measured by ellipsometry in order to check the accuracy of temperature.

2.3 SIMS measurements

The depth profiles of ^{30}Si, B, and SiH(mass = 31) have been measured with ATOMIKA SIMS 4000, which is equipped with a quadrupole mass spectrometer that analyzes secondary ions within a defined range of energy, using O_2^+ for a primary ion beam with acceleration energy 5 keV. An incident angle of the primary ion beam was 45°. An electron beam was irradiated during the measurement in order to prevent samples from charge accumulation. Crater depths resulted by sputtering were measured with a typical surface profilometer (Talystep of Taylor Hobson) with the accuracy of ± 10%. The main cause of the error in depth profiles determined by the SIMS measurements was the error of measurements of the crater depths. In order to minimize the error, we conducted SIMS measurements for each sample twice, and the reproducibility of SIMS measurements was always checked.

2.3.1 Insulator effects

The analysis of insulators using SIMS has traditionally been difficult because of the electrical charge buildup associated with the bombardment of the sample with a charged particle beam. The secondary ion energy distribution can be affected by charging of an insulating sample during analysis. Sample charging has the effect of producing an unknown offset on the sample and can move the energy distribution partially or even totally out of the energy window with the result that fewer or even no secondary ions are detected.

Many approaches have been attempted to reduce sample charging, but electron beam charge neutralization was applied at an early stage in instrument development and has proved to be most successful for almost every matrix attempted.

2.3.2 Surface effects

Several effects at the surface or in the near surface region must be accounted for to properly interpret data at the beginning of a depth profile.

A native oxide is present on many samples. In Si, a native oxide will begin forming almost immediately after a fresh surface is exposed and will reach a final thickness of 1 to 1.5 nm. For SIMS depth profiles, the surface oxide will cause a surface peak for many species.

Until the depth corresponding to the projected range of the primary beam has been eroded away by sputtering, the atom density of the primary species in the sample is not at equilibrium. The equilibration depth is related to the penetration of the primary species and increases with primary energy but decreases with angle of incidence from normal.

C and O present as surface contamination can require a significant depth of sputtering to be removed. As a result, much of the information in this part of the profile can be lost. Other contaminants, such as Al, may be present at the surface and cause secondary ion yield changes or mass interferences.

Clean handling of the samples is very important. Samples that have dust often have contaminants that preclude the analysis of many important elements either directly or as the result of mass interferences.

Chapter 3

An overview of diffusion in solids

In this chapter, an introduction to basics of diffusion in Si and SiO_2 is given. In addition, this chapter introduces analyses of diffusion in the isotope heterostructures and implanted samples employed in this study.

3.1 Diffusion basics

Diffusion is the process by which matter is transported from one part of a system to another as a result of random microscopic (i.e., atomic-scale) motions [29, 30, 31], and the concentration of the matter is relaxed to its equilibrium concentraion.

3.1.1 Fick's first law

Fick established the mathematical model of diffusion in isotropic substances based on the hypothesis that the mass flux **J**, which is the rate of transfer per unit area, is proportional to the concentration gradient measured normal to the section, i.e.

$$\mathbf{J} = -D\nabla C, \tag{3.1}$$

where C is the concentration of diffusing substance and D is called the diffusion coefficient. The negative sign in eq. (3.1) arises because diffusion occurs in the direction to that of decreasing concentration.

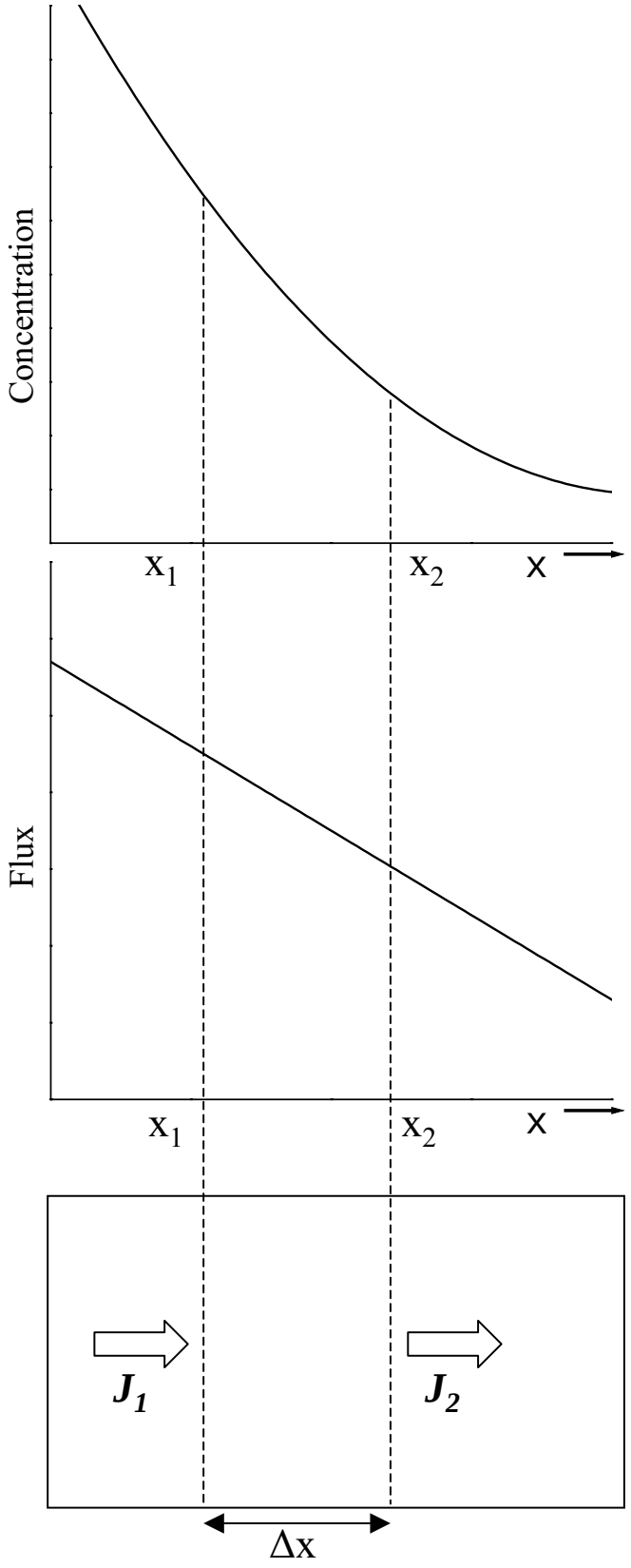

Figure 3.1: (a) concentration and (b) flux of diffusing species as a function of position x. Schematics of flux is shown in (c).

3.1.2 Fick's second law

Unless a steady state exists, that is, the concentration at some point is changing with time, eq. (3.1) is still valid. In order to obtain more useful relation, we derive differential equations of diffusion in an isotropic substance from eq. (3.1) as follows. Mass conservation is a general physical constraint that may be imposed on diffusing systems. Mass is conserved at all points in the medium, even under the action of a diffusion flux. Thus the mass balance may be expressed as

$$\text{accumulation rate} = \text{inflow} - \text{outflow}. \tag{3.2}$$

Consider a bar of unit cross sectional area with the x axis along its center. An element Δx along the x axis has flux J_1 to one side and J_2 to the other, as shown in Fig. 3.1. If Δx is very small J_1 can be accurately described by

$$J_1 = J_2 - \Delta x\Big(\frac{\partial J}{\partial x}\Big). \tag{3.3}$$

The volume of the element is $1{\cdot}\Delta x$ (unit area times the thickness), so the net increase in matter in the element can be described by any part of

$$J_1 - J_2 = \Delta x\Big(\frac{\partial C}{\partial t}\Big) = -\Delta x\Big(\frac{\partial J}{\partial x}\Big). \tag{3.4}$$

Such procedure is done for y and z directions.

$$\Delta x\Delta y\Delta z\Big(\frac{\partial C}{\partial t}\Big) = -\Delta x\Delta y\Delta z\Big(\frac{\partial J_x}{\partial x} + \frac{\partial J_y}{\partial y} + \frac{\partial J_z}{\partial z}\Big), \tag{3.5}$$

or

$$\frac{\partial C}{\partial t} = -\nabla\mathbf{J}. \tag{3.6}$$

Substituting eq. (3.1) into eq. (3.6), we can obtain Fick's second law:

$$\frac{\partial C}{\partial t} = -\nabla\cdot\big(-D\nabla C\big). \tag{3.7}$$

If the diffusivity D is a constant, the divergence operator commutes only with ∇C, and eq. (3.7) simplifies to the linear form of Fick's second law,

$$\frac{\partial C}{\partial t} = D\nabla^2 C. \tag{3.8}$$

3.2 Diffusion in silicon

Atomic diffusion processes in silicon play an important role in the fabrication of electronic devices in various areas. Silicon is one of the most important materials, and a considerable number of studies on diffusion in Si has been conducted, therefore, a significant progress has been made in understanding point defects and diffusion mechanisms in Si.

Boron doping is an important process in the fabrication of silicon based semiconductor devices. As dimensions shrink to nanometer scales, it becomes critical to obtain precise control of doping profiles. Therefore, a great deal of efforts is being devoted to understanding and controlling diffusion of boron during implantation and annealing [32].

Elements diffusing in semiconductors are classified into slow or fast diffusers in relative manners [33]. Fast diffusers have diffusivity that is many orders magnitude larger than that of slow diffusers. The large difference between fast and slow diffusers is caused by the difference in different diffusion mechanisms, which are closely related to their incorporation in the lattice.

Slow diffusers, such as common group III and group V dopants, are substitutionally dissolved and require intrinsic point defects (vacancies and/or self-interstitials) for their diffusion process, while fast diffusers, such as Cu, Li, H, or Fe, are predominantly interstitially dissolved and move by jumping from one interstitial site to another interstitial site without any contribution of intrinsic point defects.

Figure 3.2 shows some common atomic diffusion models in a solid [33, 34], using a simplified two-dimensional crystal structure. At elevated temperatures the lattice atoms vibrate around the equilibrium lattice sites. Occasionally a host atom acquires sufficient energy to leave the lattice site, becoming a self-interstitial and creating a vacancy. When a neighboring atom migrates to the vacancy site, it is called vacancy mechanism, as schematically shown in Fig. 3.2(a).

Suppose elements A are placed at interstitial (A_i) and substitutional (A_s) sites. Kick-out mechanism involves self-interstitial (I) for interchanging between (A_i) and (A_s) via the reaction

$$A_i \leftrightarrow A_s + I, \tag{3.9}$$

as shown in Fig. 3.2(a).

In the interstitialcy mechanism, a self-interstitial replaces a substitutional atom which

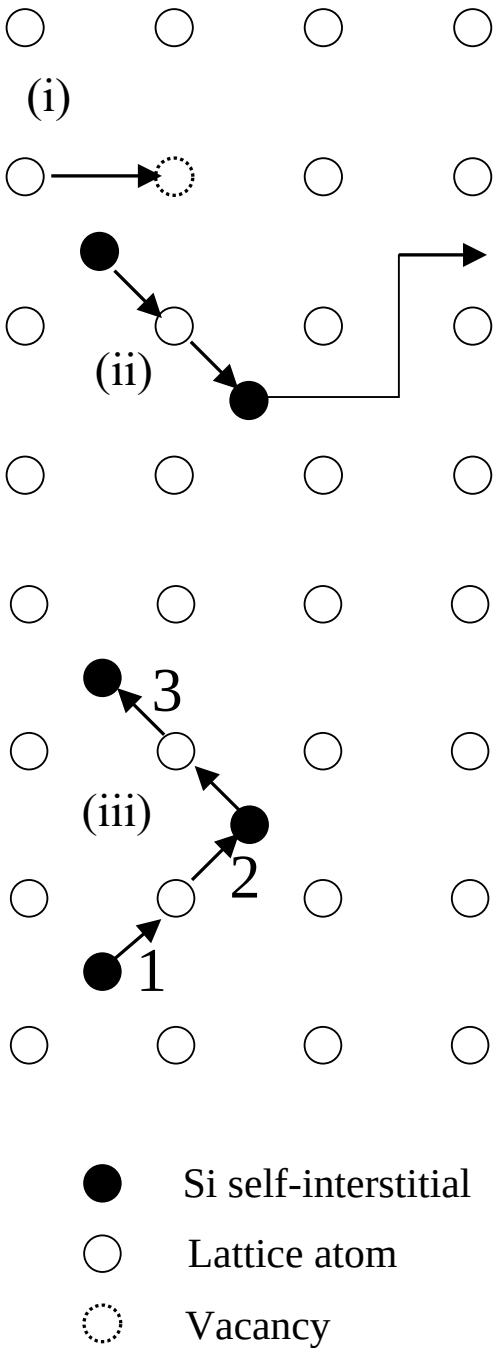

Figure 3.2: Models of atomic diffusion for a two-dimensional lattice. (i) Vacancy, (ii) kick-out, and (iii) interstitialcy mechanisms.

then in return replaces a neighboring lattice atom, as shown in Fig. 3.2(b).

3.2.1 Silicon self-diffusion in silicon

Silicon is a host atom in crystalline silicon, therefore, Si self-diffusion has to be mediated by point diffects. Ural *et al.*, reported that Si self-diffusion in crystalline silicon is enhanced during nitridation and oxidation[35], as shown in table. 3.1. Therefore, it is known that Si self-diffusion in Si involves self-interstitials and vacancies. In addition, it was reported that Si diffuses in Si via direct exchange mechanism [36]. However, it is generally thought that the contribution of the direct exchange mechanism is very small.

Table 3.1: Summary on oxidation and nitridation effect on stacking fault and diffusion behaviors. (see ref. 32 for detail)

	Oxidation $I \uparrow V \downarrow$	Nitridation $I \downarrow V \uparrow$
Stacking faults	Grow	Shrink
P,B diffusion		
intrinsic	Enhanced	Retarded
extrinsic	Enhanced	Retarded
Sb diffusion		
intrinsic	Enhancement precedes retardation.	Enhanced
As diffusion		
intrinsic	Enhanced	Enhanced
extrinsic	Retarded or no effect	Enhanced
Si self-diffusion	Enhanced	Enhanced

3.2.2 Boron diffusion in silicon

As mentioned above, boron is one of group III dopants and is dissolved almost entirely on substitutional sites. Therefore, boron diffusion is mediated by intrinsic point defects. Boron diffusion is retarded during nitridation and enhanced during oxidation[37], as shown in table 3.1. Moreover boron diffusion mainly involves self-interstitials [38].

B diffusion is known to be retarded by nitridation [39, 40], which induces vacancy supersaturation. Using the degree of retardation, the fractional diffusion component related to self-interstitials f_I of B has been estimated to be close to unity [39]. In addition, due to the Fermi level effect, doping with p-type impurities increases the equilibrium concentration of self-interstitials, while it decreases that of vacancies [41]. In the extrinsic region of B profiles, therefore, the vacancy contribution is very minor because the self-interstitial and the vacancy contribution to the Si self-diffusion under intrinsic conditions [39] are close to each other. In the intrinsic region, the supersaturation of self-interstitials induced by the kick-out reaction:

$$B_i \leftrightarrow B_s + I, \tag{3.10}$$

induces an undersaturation of vacancies, and hence the vacancy contribution is again smaller than the interstitial contribution. This minor contribution of vacancies compared to that of self-interstitials in both the extrinsic and intrinsic regions retards both the Frank-Turnbull [33, 41] and the vacancy mechanisms. Consequently, B diffusion is primarily governed by the kick-out mechanism.

3.2.3 Diffusion during oxidation of silicon

Oxidation of silicon is one of the most important processes in fabrication of Si based electronic devices. Therefore, a considerable number of studies on oxidation of silicon has been reported. It is known that oxidation of Si leads to enhanced diffusion of the common substitutionally dissolved B, In, Al, Ga, P, As, and Si, and to nucleation and growth of interstitial-type dislocation loops containing stacking faults (oxidation-induced stacking faults: OSF). These phenomena can be explained by self-interstitials injection into Si substrate from the Si/SiO_2 interface during thermal oxidation. Injection of self-interstitials leads to supersaturation of self-interstitials. Therefore, diffusion of atoms which are mediated by silicon self-interstitials is enhanced, and oxidation-induced stacking faults are grown during thermal oxidation.

Table 3.1 summarizes some of the results from oxygen and NH_3 treatments on the diffusion, including the growth or shrinkage of oxidation-induced stacking faults (OSF).The NH_3 ambient is known to inject vacancies and lead to an undersaturation of self-interstitials. Therefore, diffusion involving interstitials is retarded and stacking faults shrink.

The driving force for self-interstitial injection during oxidation is the volume expansion of about a factor of two associated with the SiO_2 formation at the SiO_2/Si interface.

No vacancies have to be involved for understanding oxidation-enhanced diffusion (OED). The explanation of the observed oxidation-retarded diffusion (ORD) of Sb under the same oxidation-conditions requires the presence of a second type of point defects. The simultaneous occurrence of retarded and enhanced diffusion phenomena can be explained by a model which assumes that Sb diffuses predominantly via vacancies but oxidation-induced self-interstitials partly recombine with vacancies according to

$$\mathrm{I} + \mathrm{V} \leftrightarrow 0, \tag{3.11}$$

where 0 denotes the undisturbed lattice. Under thermal equilibrium conditions vacancies and self-interstitials will possess their equilibrium concentrations $\mathrm{C_V^{eq}}$ and $\mathrm{C_I^{eq}}$, respectively. If the local dynamical equilibrium is established, this process leads to an undersaturation of vacancies ($\mathrm{C_V} < \mathrm{C_V^{eq}}$) associated with a supersaturation of self-interstitials ($\mathrm{C_I} > \mathrm{C_I^{eq}}$) via mass action law

$$\mathrm{C_V C_I} = \mathrm{C_V^{eq} C_I^{eq}}. \tag{3.12}$$

In eq.(3.12), $\mathrm{C_V}$ and $\mathrm{C_I}$ are the concentrations of vacancies and self-interstitials, respectively. For a quantitative treatment, the diffusivity D under thermal equilibrium conditions for intrinsic point defects ($\mathrm{C_V} = \mathrm{C_V^{eq}},\ \mathrm{C_I} = \mathrm{C_I^{eq}}$) is expressed in terms of a diffusion component D_I involving self-interstitials and a diffusion component D_V via vacancies:

$$D^{eq} = D_\mathrm{I} + D_\mathrm{V}. \tag{3.13}$$

For non-equilibrium conditions D changes to

$$D = D_\mathrm{I}\frac{C_I}{C_I^{eq}} + D_\mathrm{V}\frac{C_V}{C_V^{eq}}. \tag{3.14}$$

3.3 Diffusion in SiO_2

3.3.1 Point defects in SiO_2

Compositional and structural transition layers exist between bulk SiO_2 and crystalline Si substrate. In addition, stoichiometric bulk SiO_2 possesses a variety of point defects [42, 43]. The dangling orbital or paramagnetic centers have been the subjects of extensive research in thermal SiO_2 as well as crystalline silica. Electron spin resonance (ESR) is the powerful tool for study of these centers.

The P_b center, corresponding to an unpaired Si-electron or Si-dangling bond, is characteristic of the SiO_2/Si interface.

The excess-oxygen center, called non-bridging-oxygen hole center (NBOHC), i.e., $O_3 \equiv Si - O \cdot \ldots H - O - Si \equiv O_3$ and the peroxy radical ($O_3 \equiv Si - O - O\cdot$) are important centers. They do not exist in quartz, since they would require a severe local distortion of the lattice.

The essential element of the very important E' center is the moiety ($O_3 \equiv Si\cdot$). There are two main subtypes, i.e., E'$_\gamma$ ($O_3 \equiv Si \cdot \ldots^+ Si \equiv O_3$) and E'$_s$ ($O_3 \equiv Si\cdot$). They have been most often and most clearly observed.

3.3.2 Diffusion in SiO_2

Oxygen diffusion in SiO_2 is a great importance in thermal oxidation of silicon. Therefore, extensive studies have been given to oxygen diffusion in SiO_2 [44, 45]. It was reported that oxygen diffusion has two different, parallel and probably non-correlated diffusion mechanisms [46]. In one of them, oxygen is transported through the oxide network without interacting with it. In the other, oxygen is incorporated in the near-surface region, mostly by exchange for oxygen atoms from the near-surface oxide network via interstitialcy mechanism [46].

Boron diffusion in SiO_2 is also important for device fabrication process. Fair reported that boron diffusion is mediated by peroxy-linkage defects ($O_3 \equiv Si - O - O - Si \equiv O_3$) [47]. Otani *et al.* reported first-principle total-energy calculations that provide stable and metastable geometries and diffusion mechanisms of boron in SiO_2 with point defects which contain O vacancies and O interstitials, and found that a boron atom forms various (meta)stable geometries in SiO_2 with point defects, depending on its charge state [21, 22, 23].

3.4 Analysis of diffusion profiles

This section describes the solutions which will be used in the later chapters to analyze our experimental results.

3.4.1 Instantaneous planar diffusion source in an infinite medium

Let us consider the problem of instantaneously releasing a quantity of diffuser M, at the plane $x = 0$ at $t = 0$, as shown in Fig. 3.3. The diffuser is allowed to spread into the two adjacent material occupying the half-spaces $0 < x < \infty$ and $-\infty < x < 0$. Both materials have equal and constant diffusivities, D. For example, this situation corresponds to delta doping of impurity atoms in semiconductors.

Application of the Laplace transform procedure to Fick's second law (eq. (3.3)) yields;

$$\int_0^\infty \exp(-pt)\frac{\partial^2 C}{\partial x^2}dt - \frac{1}{D}\int_0^\infty \exp(-pt)\frac{\partial C}{\partial t}dt = 0. \tag{3.15}$$

The first integral appearing in eq.(3.15) may be determined by transposing the order of the differentiation and integration:

$$\int_0^\infty \exp(-pt)\frac{\partial^2 C}{\partial x^2}dt = \frac{\partial^2}{\partial x^2}\int_0^\infty C\exp(-pt)dt = \frac{d^2\tilde{C}}{dx^2}, \tag{3.16}$$

where the image function $\tilde{C}$ produced on the right-hand side of eq. (3.16) is the *Laplace transform of the concentration field*, defined operationally by the integral

$$\tilde{C} \equiv \int_0^\infty C\exp(-pt)dt. \tag{3.17}$$

The second integral in eq. (3.15) arising in the transform procedure for Fick's second law can be evaluated by using partial integration

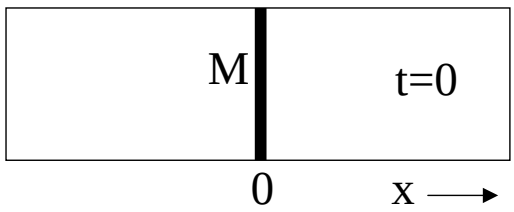

Figure 3.3: Flow of an instantaneous source M released into surrounding semi-infinite media.

$$\int_0^\infty \exp(-pt)\frac{\partial C}{\partial t}dt = \Big[C(x,t)\exp(-pt)\Big]_0^\infty - p\int_0^\infty -C(x,t)\exp(-pt)dt \\ = 0 - C(x,0) + p\tilde{C}. \tag{3.18}$$

Equations (3.16) and (3.18) are inserted into eq. (3.15), and we can obtain an ordinary deferential equation (ODE)

$$\frac{p}{D}C(x,p) - \frac{d^2C(x,p)}{dx^2} = \frac{C(x,0)}{D}, \tag{3.19}$$

subjects to the initial condition at time t=0, C(x,0)=0 for all $x \neq 0$ and the boundary condition C($\pm\infty$,t)=0, so the finite mass of diffuser M released by the source cannot alter the composition of this infinitely long bar of material far away from the source's location. The diffusion process is overall subject to the integral mass constraint

$$\int_{-\infty}^{\infty} C(x,t)dx = M, \tag{3.20}$$

which accounts for the diffuser spreading with time over all space. The initial condition reduces the Laplace-transformed Fick's second law

$$\frac{p}{D}C(x,p) - \frac{d^2C(x,p)}{dx^2} = 0, \tag{3.21}$$

since the right-hand side of eq. (3.19) vanishes at $t = 0$ for all x, except for the source plane itself at $x = 0$. Now eq. (3.21) is a well-known ODE, and the solution of this ODE is

$$\tilde{C} = A\exp\Big(\sqrt{\frac{p}{D}}x\Big) + B\exp\Big(-\sqrt{\frac{p}{D}}x\Big). \tag{3.22}$$

The boundary condition specified above indicates that both terms appearing in the eq. (3.22) will be needed to provide solutions for the left- and right-going diffusion fields. Therefore, the right-going diffusion field is

$$\tilde{C} = B\exp\Big(-\sqrt{\frac{p}{D}}x\Big), \qquad x > 0 \qquad (A = 0), \tag{3.23}$$

and the left-going diffusion field is

$$\tilde{C} = A\exp\Big(\sqrt{\frac{p}{D}}x\Big), \qquad x > 0 \qquad (B = 0). \tag{3.24}$$

Symmetry requires that diffusion flow left and right equally, so the global mass constraint for the half-space $x > 0$ can be formulated by eq. (3.23) into eq. (3.20) as

$$\int_0^\infty C(x,t)dx = \frac{M}{2}. \tag{3.25}$$

Now, applying the Laplace transform to eq. (3.25), we obtain

$$\mathrm{L}\left\{\int_0^\infty C(x,t)dx\right\} = \mathrm{L}\left\{\frac{M}{2}\right\} \tag{3.26}$$

or

$$\int_0^\infty e^{-pt}\int_0^\infty C(x,t)dxdt = \int_0^\infty e^{-pt}\frac{M}{2}dt. \tag{3.27}$$

From eq. (3.27), we obtain the expression for the image function

$$\int_0^\infty \tilde{C}(x,p)dx = \frac{M}{2p}. \tag{3.28}$$

Now, substituting eq. (3.23) into the left-hand side of eq. (3.28) for $x > 0$ shows that

$$\int_0^\infty B\exp\Big(-\sqrt{\frac{p}{D}}x\Big)dx = \frac{M}{2p} \tag{3.29}$$

and

$$\left[-\frac{B}{\sqrt{p/D}}\exp\Big(-\sqrt{\frac{p}{D}}x\Big)\right]_0^\infty = \frac{M}{2p}. \tag{3.30}$$

Solving eq. (3.30) for B gives

$$B = \frac{M}{2\sqrt{pD}}. \tag{3.31}$$

Substituting eq.(3.31) into eq. (3.29) gives the transform solution,

$$\tilde{C}(x,p) = \frac{M}{2\sqrt{D}}\frac{\exp\Big(-\frac{x}{\sqrt{D}}\sqrt{p}\Big)}{\sqrt{p}}. \tag{3.32}$$

The transform solution can be inverted to find the concentration field $C(x,t)$:

$$\mathrm{L}^{-1}\{\tilde{C}\} = C(x,t) = \frac{M}{2\sqrt{D}}\mathrm{L}^{-1}\left\{\frac{e^{-a\sqrt{p}}}{\sqrt{p}}\right\} \tag{3.33}$$

where $a = \frac{x}{\sqrt{D}}$.

Reffering to the table of Laplace transforms, we use the following relation:

$$\mathrm{L}^{-1}\left\{\frac{e^{-a\sqrt{p}}}{\sqrt{p}}\right\} = \frac{1}{\sqrt{\pi t}}\exp\left(-\frac{a^2}{4t}\right) \tag{3.34}$$

to obtain the diffusion solution:

$$C(x,t) = \frac{M}{2\sqrt{\pi Dt}}\exp\left(-\frac{x^2}{4Dt}\right). \tag{3.35}$$

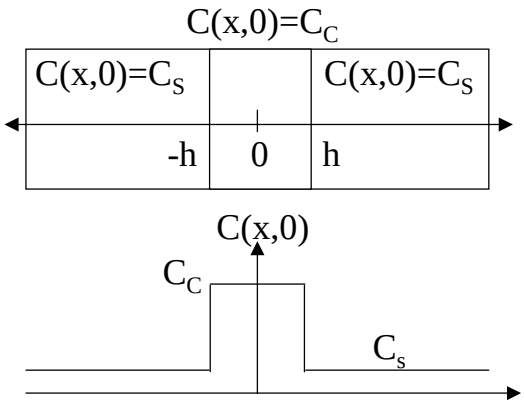

Figure 3.4: Configuration of a composite slab and the concentration as a function of x.

3.4.2 Solution for isotope heterostructures

In this section, the solution of Fick's second law for isotope hetero structures will be given. The linearity of the diffusion equation permits the use of superposition to produce new solutions for different geometric arrangements of the sources. A basic solution found for the release of an instantaneous amount of diffusers from a planar source into an infinite system, can be superposed to develop new solutions. This procedure requires that the boundary conditions for the new solutions are identical to those for the basic solution.

Now, consider the semi-infinite system as shown in Fig. 3.4. A slab of width $2h$ having a uniform initial concentration C_c is joined as two long bars having a uniform concentration C_s. The central slab and the long bars are the same phase and have equal diffusivities. The initial concentration may be interpreted as a continuous distribution of instantaneous, differential, planar sources of strength $dM = C_c d\hat{x}$ and $dM = C_s d\hat{x}$, spread uniformly over the central slab and both side bars, respectively.

The concentration response at any location $-\infty < x < \infty$, at any future time $t > 0$, is the unknown field $C(x,t)$. This concentration field may be thought of as the sum, or integral, of all the sources released instantaneously at $t = 0$, from locations $-\infty < \hat{x} < \infty$. The total response occurring at any plane x at some later time t is given by the superposition, or source integral,

$$\begin{aligned} C(x,t) = C_s \int_{-\infty}^{-h} \frac{\exp(-\frac{(x-\hat{x})^2}{4Dt})}{\sqrt{4\pi Dt}} d\hat{x} + C_c \int_{-h}^{h} \frac{\exp(-\frac{(x-\hat{x})^2}{4Dt})}{\sqrt{4\pi Dt}} d\hat{x} \\ + C_s \int_{h}^{\infty} \frac{\exp(-\frac{(x-\hat{x})^2}{4Dt})}{\sqrt{4\pi Dt}} d\hat{x}. \end{aligned} \tag{3.36}$$

The integrand of the superposition integral corresponds to the instantaneous source solution as described by

$$C(x,t) = \frac{M}{2\sqrt{\pi Dt}} \exp\Big(-\frac{x^2}{4Dt}\Big). \tag{3.37}$$

Equation (3.36) is evaluated using the variable substitution

$$u = \frac{x - \hat{x}}{2\sqrt{Dt}}. \tag{3.38}$$

The total differential of u is

$$du = \frac{-d\hat{x}}{2\sqrt{Dt}} \qquad (x = \text{const}). \tag{3.39}$$

The source integral, eq. (3.36), may be written in terms of the new variable $u(\hat{x}, t)$ as

$$\begin{aligned} C(x,t) &= \frac{C_s}{\sqrt{\pi}} \int_{\infty}^{\frac{x+h}{2\sqrt{Dt}}} -e^{-u^2} du + \frac{C_c}{\sqrt{\pi}} \int_{\frac{x+h}{2\sqrt{Dt}}}^{\frac{x-h}{2\sqrt{Dt}}} -e^{-u^2} du + \frac{C_s}{\sqrt{\pi}} \int_{\frac{x-h}{2\sqrt{Dt}}}^{-\infty} -e^{-u^2} du \\ &= -\frac{C_s}{\sqrt{\pi}} \left[\int_0^{\frac{x+h}{2\sqrt{Dt}}} e^{-u^2} du - \int_0^{\infty} e^{-u^2} du \right] - \frac{C_c}{\sqrt{\pi}} \left[\int_0^{\frac{x-h}{2\sqrt{Dt}}} e^{-u^2} du - \int_0^{\frac{x+h}{2\sqrt{Dt}}} e^{-u^2} du \right] \\ &\quad - \frac{C_s}{\sqrt{\pi}} \left[\int_0^{-\infty} e^{-u^2} du - \int_0^{\frac{x-h}{2\sqrt{Dt}}} e^{-u^2} du \right] \\ &= -\frac{C_s}{2} \left[\operatorname{erf}\left(\frac{x+h}{2\sqrt{Dt}} \right) - \operatorname{erf}\Big(\infty \Big) \right] - \frac{C_c}{2} \left[\operatorname{erf}\left(\frac{x-h}{2\sqrt{Dt}} \right) - \operatorname{erf}\left(\frac{x+h}{2\sqrt{Dt}} \right) \right] \\ &\quad - \frac{C_s}{2} \left[\operatorname{erf}\Big(-\infty \Big) - \operatorname{erf}\left(\frac{x-h}{2\sqrt{Dt}} \right) \right], \end{aligned} \tag{3.40}$$

where $\operatorname{erf}(z)$ is the error function as defined by

$$\operatorname{erf}(z) = \frac{2}{\sqrt{\pi}} \int_0^z \exp\Big(-\eta^2\Big) d\eta. \tag{3.41}$$

Then we can obtain the solution of Fick's second law for this problem as described by

$$C(x,t) = C_s + \frac{C_c - C_s}{2}\left[\mathrm{erf}\left(\frac{x+h}{2\sqrt{Dt}}\right) - \mathrm{erf}\left(\frac{x-h}{2\sqrt{Dt}}\right)\right]. \tag{3.42}$$

For this solution it is assumed that the medium, which diffusion takes place in, is infinitely long. Since $\frac{\partial C}{\partial x} = 0$ at $x = 0$ in this solution, it can be used for the isotope heterostructure shown in Fig. 2.1.

$$C(x) = C_{^{28}\mathrm{SiO_2}} + \frac{C_{^{\mathrm{nat}}\mathrm{SiO_2}} - C_{^{28}\mathrm{SiO_2}}}{2}\left[\mathrm{erf}\left(\frac{x+h}{2\sqrt{Dt}}\right) - \mathrm{erf}\left(\frac{x-h}{2\sqrt{Dt}}\right)\right]. \tag{3.43}$$

3.4.3 Analysis of ion-implanted samples

Each implanted ion has a random path as it moves through the target, losing energy by nuclear and electronic stopping. The depth distribution of ions can be approximated as Gaussian with standard deviation σ_p. Far from a mask edge, we can neglect lateral motion and approximately write the implanted ion concentration $C(x)$ as

$$C(x) = C_0 \exp\left(\frac{-(x-R_p)^2}{2\sigma_p^2}\right), \tag{3.44}$$

where R_p is the average depth of the implanted ions and called the projected range, and C_0 is the peak concentration. If the total dose is Φ, then the C_0 is expressed by

$$C_0 = \frac{\Phi}{\sqrt{2\pi}\sigma_p}. \tag{3.45}$$

One may notice that eq. (3.44) is equivalent to eq. (3.37), which is the solution for the instantaneous diffusion source. If after t_1, the diffusion profile is identical with the initial distribution of implanted ions, described as

$$C(x,0) = C_0 \exp\left(\frac{-(x-R_p)^2}{2\sigma_p^2}\right) = \frac{M}{2\sqrt{\pi D t_1}} \exp\Big(-\frac{(x-R_p)^2}{4Dt_1}\Big), \tag{3.46}$$

the distribution of implanted ions after t is the same distribution as the instantaneous diffusion source after $t + t_1$. Therefore, the diffused distribution of implanted ions $C(x,t)$ is given by

$$C(x,t) = \frac{M}{2\sqrt{\pi D(t_1+t)}} \exp\Big(-\frac{(x-R_p)^2}{4D(t_1+t)}\Big). \tag{3.47}$$

In eq. (3.47), t_1 and M have the relation:

$$\begin{aligned} t_1 &= \frac{\sigma_p^2}{2D}, \\ M &= C_o \sigma_p \sqrt{2\pi}. \end{aligned} \tag{3.48}$$

However, depth profiles of implanted ions very often deviate from eq. (3.44)[48]. Therefore, more complicated analytical models have been proposed. These models, Fick's second law cannot be solved analytically. Thus, in this work, we have used numerical approximation technique to solve Fick's second law for implanted samples. The numerical approximation technique employed is described in Appendix A.

Chapter 4

Si self-diffusion in SiO_2 under equilibrium condition

4.1 Measurement of Si self-diffusion in argon with 1% oxygen ambient

4.1.1 Introduction

Atomic-level understanding of the oxidation mechanism is becoming increasingly important for the reason described in Chapter 1. While the rate of oxygen arriving at the Si/SiO_2 interface dominantly determines the speed of thermal oxidation when SiO_2 thickness is much larger than 100 nm [49], more recent oxidation models mostly for much thinner cases point out the importance of silicon self-diffusion processes for the thermal formation of SiO_2 [2, 3, 39, 50, 51, 52]. Therefore, self-diffusion of Si in thermally-grown SiO_2 is a fundamental physical phenomenon that needs to be understood in order to achieve a complete understanding of thermal oxidation processes.

To our knowledge, there have been a few experimental investigations on Si self-diffusion performed with SiO_2 formed thermally on semiconductor silicon [14, 53]. In one of them, ^{30}Si isotopes have been ion-implanted into isotopically enriched $^{28}SiO_2$ layers, and their diffusion profiles have been measured by secondary ion mass spectrometry (SIMS) after appropriate annealing procedures [14]. Because of the thin SiO_2 layer employed, the diffusion coefficient reported in ref. 14 represents the non-equilibrium condition (see chapter 5 in detail). In the other experiment, self-diffusion has been studied indirectly by monitoring the formation of defects that are believed to be triggered by self-diffusion of Si in

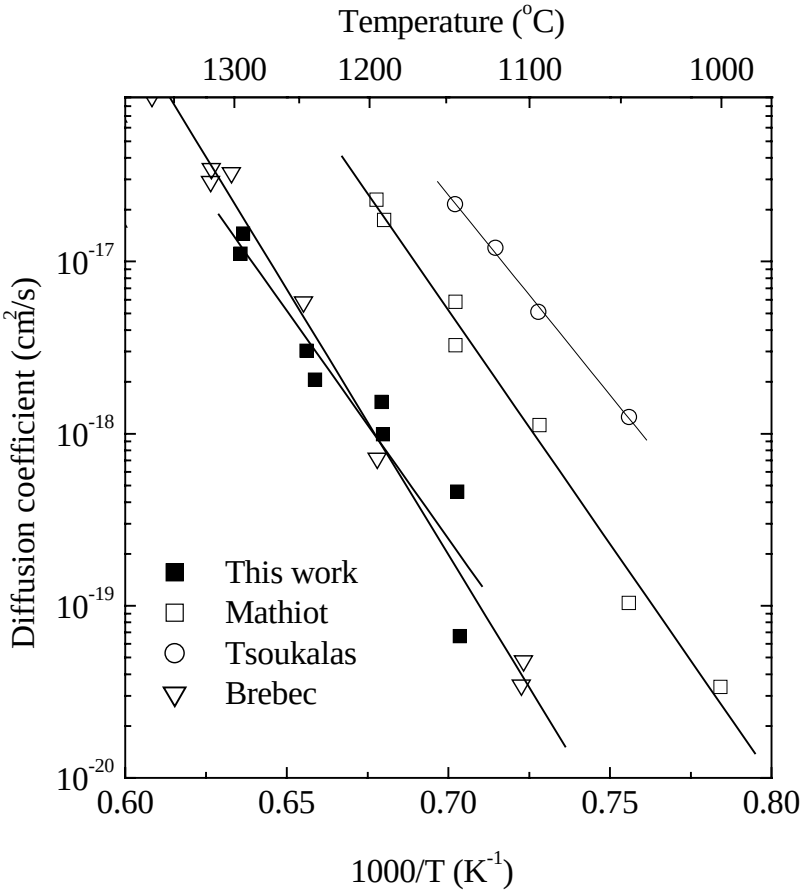

Figure 4.1: Diffusivity of Si in SiO_2 Ref 13 (□), Ref 14 (○), and Ref 11 (▽). ■ represents the results of this work.

SiO_2 [53]. This experiment has also been performed under the non-equilibrium condition since the diffusing Si species have been produced in excess by oxidation. Equilibrium self-diffusion properties of Si in SiO_2, on the other hand, have been measured not with thermal oxides on semiconductor silicon but with other types of SiO_2 such as fused silica [11] and quartz [12]. The self-diffusion constants as a function of temperatures found in these studies are summarized in Fig. 4.1. What has been missing clearly is an experiment performed under the equilibrium condition using thermal oxides grown directly on semiconductor grade silicon wafers. The Si self-diffusion coefficients previously measured with semiconductor-grade thermally grown SiO_2[14, 53] are 2 to 3 orders of magnitude higher than the values measured with fused silica [11] and quartz [12]. Whether this large

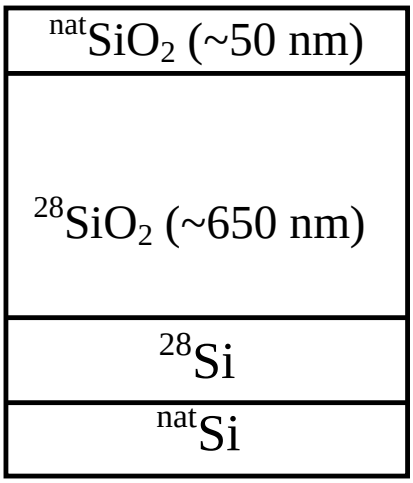

Figure 4.2: The schematic of a $^{nat}SiO_2/^{28}SiO_2$ isotope heterostructure

difference in the diffusion coefficients is owning to the non-equilibrium vs. equilibrium conditions and/or to the subtle differences in the structural properties of thermally grown SiO_2, fused silica, and quartz are not obvious.

In order to provide the answers to these concerns, the present work reports on self-diffusion experiments of Si in thermally grown SiO_2 under equilibrium condition. The investigation has been performed using a isotope heterostructure ($^{nat}SiO_2/^{28}SiO_2$) shown in Fig. 4.2. $^{nat}SiO_2$ and $^{28}SiO_2$ indicate SiO_2 composed of natural Si and isotopically enriched ^{28}Si, respectively. Such a stable isotope heterostructure is suitable for the study of self-diffusion and has been used for Si self-diffusion in Si[35, 54], Ge self-diffusion in Ge[55] and Ga self-diffusion both in GaAs[56] and GaP[57].

Subsequent to heat treatments at desired diffusion temperatures, SIMS measurements of the diffusion depth profile of the ^{30}Si isotope concentration across $^{nat}SiO_2$ and $^{28}SiO_2$ layers have allowed for accurate determination of Si self-diffusion coefficients under equilibrium conditions. Isotope heterostructures are clearly the ideal systems to study self-diffusion under equilibrium condition because the concentrations of constituents (Si and O) and native defects remain at equilibrium values throughout the course of experiments.

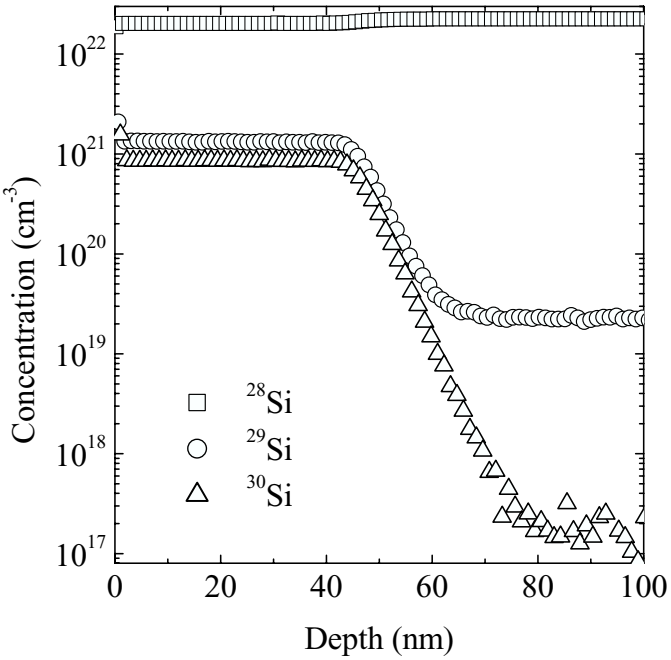

Figure 4.3: SIMS depth profiles of as grown $^{nat}SiO_2/^{28}SiO_2$ isotope heterostructure

4.1.2 Experiment

Samples employed in this chapter have been prepared as mentioned in § 2.1.1. The sample grown on the 4-inch wafer was cut into 5×5 mm^2 pieces. An each piece was annealed at temperatures between 1150 and 1300°C. For the annealing ambient, flowing argon with 1% oxygen was used, as mentioned before. The oxygen oxidizes ^{28}Si at the interface $^{28}SiO_2/^{28}$Si and forms additional $^{28}SiO_2$. The thickest $^{28}SiO_2$ of all heat procedures in the present experiment was formed by 1150°C annealing for 540 h in which the thickness of the $^{28}SiO_2$ increased from 650 nm to 780 nm. However, this oxidation takes place at more than 650 nm away from the $^{nat}SiO_2/^{28}SiO_2$ interface where ^{30}Si self-diffusion takes place, i.e., the two regions are well separated in order not to affect each other. One may think that flow of oxygen molecules through the oxide could affect on Si self-diffusion in the oxide. We will show that the oxygen diffusion in the oxide does not have an influence on Si self-diffusion in § 4.2.

4.1.3 Results and discussions

The typical depth profiles of ^{30}Si before an annealing are shown in Fig. 4.3. The interface $^{nat}SiO_2/^{28}SiO_2$ of the as-grown sample that should be a complete step function is broadened. This broadening is inherent to SIMS measurement and is caused by ion mixing and surface roughening due to ion sputtering. The depth profiles of ^{30}Si in annealed samples are theoretically described by (§3.4.2):

$$C(x) = C_{^{28}SiO_2} + \frac{C_{^{nat}SiO_2} - C_{^{28}SiO_2}}{2}\left[erf\left(\frac{x+h}{2\sqrt{D^{SD}_{Si\,(th)}t}}\right) - erf\left(\frac{x-h}{2\sqrt{D^{SD}_{Si\,(th)}t}}\right)\right], \quad (4.1)$$

where $x = 0$ is the surface of the samples, $C_{^{28}SiO_2}$ and $C_{^{nat}SiO_2}$ are the concentrations of ^{30}Si in the $^{28}SiO_2$ layer and $^{nat}SiO_2$ layer, respectively, and h and t are the depth of the $^{nat}SiO_2/^{28}SiO_2$ interface and time. The thickness of the $^{28}SiO_2$ layer is regarded as infinite because no ^{30}Si reaches the interface $^{28}SiO_2/^{28}Si$ by the present annealing process. The only fitting parameter in eq. (4.1) is the self-diffusion coefficient $D^{SD}_{Si(th)}$. In order to minimize the error caused by SIMS broadening, eq. (4.1) has been corrected by the method called MRI calculation (Appendix B) [58, 59]. The MRI calculation takes SIMS broadening into account using two parameters; atomic mixing and surface roughness. The obtained diffusion coefficients are approximately 20% smaller than those obtained without MRI calculation.

The self-diffusion coefficients $D^{SD}_{Si(th)}$ for the temperature range 1150-1300°C obtained in the present study are shown in Fig. 4.1. $D^{SD}_{Si(th)}$ for 1% oxygen can be described by Arrhenius equation

$$D^{SD}_{Si(th)} = 0.8\exp\Big(-\frac{5.2\text{ eV}}{kT}\Big)\text{cm}^2/\text{s}. \quad (4.2)$$

The error of activation energy 5.2 eV was $\pm$ 0.8 eV. One may point out that the diffusion constants measured across the CVD grown $^{nat}SiO_2$ and the thermally formed $^{28}SiO_2$ do not represent the intrinsic values of the Si self-diffusion constants in thermally formed oxides. Such concern, in principle, is true but the excellent fit of eq. (4.1) to the experimentally measured profiles shown in Fig.4.4 and to the results of all the other annealing durations and temperatures indicates that the diffusion constant remain unchanged across the CVD and thermally grown oxides. Therefore our data represent very well the intrinsic values of Si self-diffusion constants in thermally formed SiO_2 grown directly on semiconductor grade Si wafers.

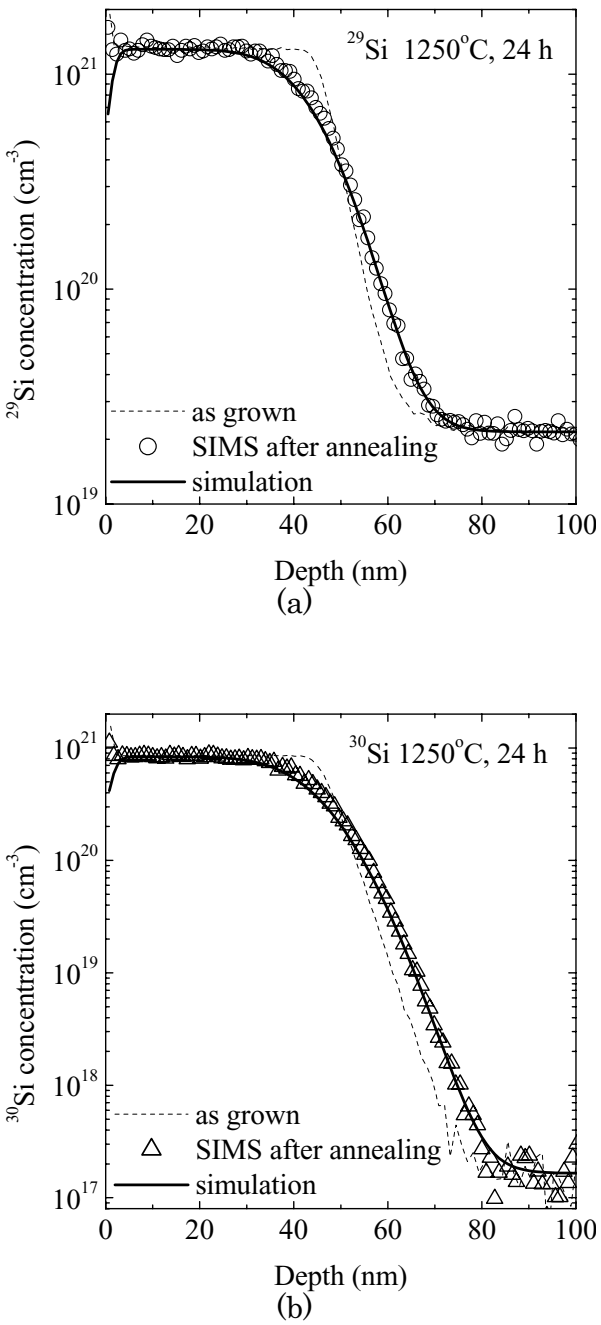

Figure 4.4: SIMS depth profiles of before and after annealing at 1250°C for 24 h (a) ^{29}Si and (b) ^{30}Si in the $^{nat}SiO_2/^{28}SiO_2$ isotope heterostructure.

The self-diffusion coefficients determined in this study agree very well with those determined with a fused silica under equilibrium condition [11]. Thermally formed SiO_2 on Si and fused silica are both amorphous silicon dioxide and share many properties in common. It is therefore understandable to obtain the same self-diffusion constants though it was not obvious prior to this study. The diffusion coefficients of the present work are 2 orders of magnitude lower than the diffusion coefficients determined by Tsoukalas *et al.* under non-equilibrium condition [14].

Recently, Mathiot *et al.* reported that the diffusion coefficients, which were obtained using a isotope heterostructure capped with a SiN layer, were about one order of magnitude larger than that of this work as shown in Fig. 4.1. Mathiot *et al.* argued that the residual oxidation totally blocks Si diffusion in SiO_2, and, that was the reason for the low diffusivity we obtained. The influence of the oxygen in an annealing ambient on Si self-diffusion is discussed in the next section to show that the residual oxygen in the annealing ambient does not influence the Si diffusivity in SiO_2. Therefore, $D^{SD}_{Si(th)}$ obtained in this section represents the intrinsic thermal equilibrium diffusivity of Si in SiO_2 formed thermally of semiconductor silicon wafers.

4.2 Influence of partial pressure of oxygen in argon on Si self-diffusion

At high temperature and low oxygen partial pressure, SiO_2 tends to decompose. In order to prevent decomposition of SiO_2, Ar gas with 1 % oxygen added has been used as the annealing ambient in the previous section [9, 15]. Mathiot *et al.* argued that annealing in an oxygen-containing ambient leads to lower self-diffusivity of Si [13] . In this section, we investigate Si self-diffusion in SiO_2 as a function of the partial pressure of oxygen in the annealing ambient and found that Si self-diffusion does not depend on the partial pressure of oxygen [10].

4.2.1 Experiment

The simple isotope heterostructure shown in Fig. 2.1 was cut into 5×5 mm^2 samples and annealed at 1200 and 1250°C under flowing Ar with 1, 10, 50, and 100 % oxygen fractions. The diffusion profiles were obtained by SIMS using the measurement condition described in § 2.3.

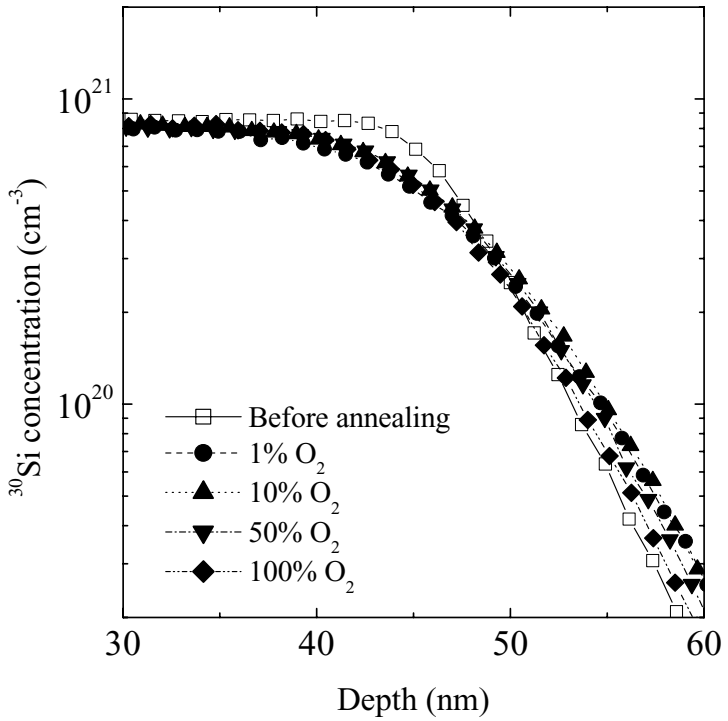

Figure 4.5: SIMS profiles of before and after annealing the $^{nat}SiO_2/^{28}SiO_2$ isotope heterostructure with different fraction of oxygen in the argon ambient at 1200°C for 48 h.

4.2.2 Results and discussions

The SIMS profiles of ^{30}Si are shown in Fig. 4.5. The results of various partial pressures of oxygen in the annealing ambient have almost the same profiles. This tendency was observed for the annealing at 1250°C. In order to estimate Si self-diffusivity in SiO_2, eq. (4.1) was used to fit the depth profiles. $D^{SD}_{Si\,(th)}$, which is the Si self-diffusivity in SiO_2, is the only fitting parameter. Solid curves in Fig. 4.5 are the calculated ^{30}Si profiles.

$D^{SD}_{Si(th)}$ obtained by fitting for various oxygen concentrations in the ambient is shown in Fig. 4.6. Our earlier data (Fig. 4.1) that correspond to the values for 1% oxygen are also shown for comparison. $D^{SD}_{Si(th)}$ depends very little on the oxygen concentration in the ambient and agrees nicely with our earlier data with 1% oxygen. The error in the broadening correction procedure is estimated to be about ±2%. This error is much smaller than about ±30% error arising from the SIMS mass separation and depth measurements. Also fitting with eq. (4.1) leads to an error of a couple percent. By adding these three major

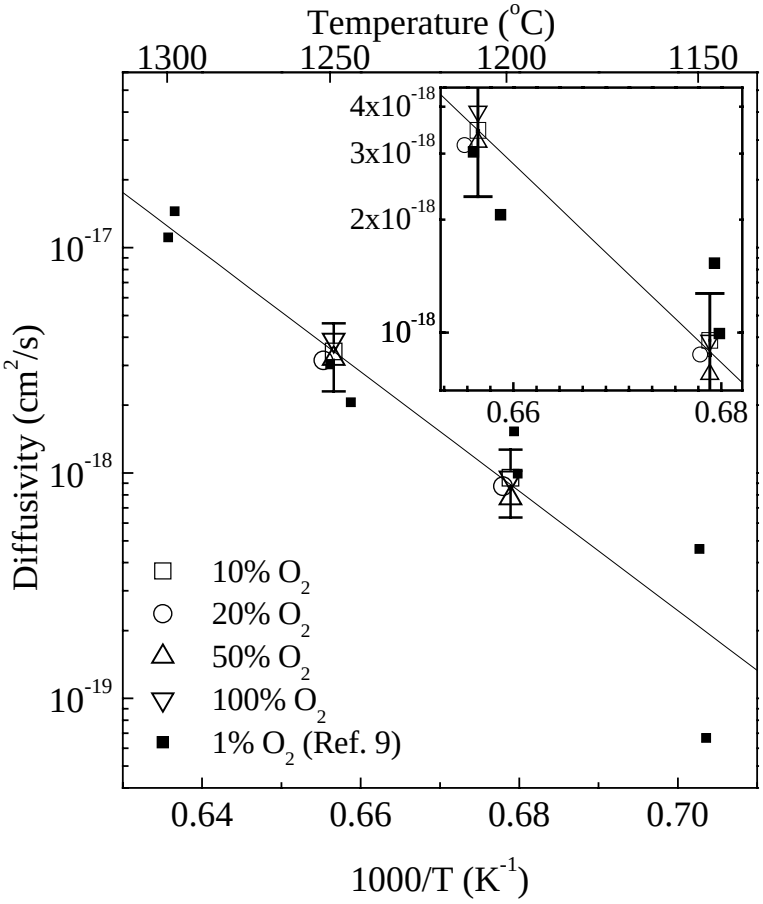

Figure 4.6: Diffusivity of Si self-diffusion using the $^{nat}SiO_2/^{28}SiO_2$ isotope heterostructure as a function of the oxygen partial pressure

sources of errors, we arrive at our total error bar of about ±33%. It is clear in Fig. 4.6 that $D^{SD}_{Si(th)}$ does not depend on the oxygen concentration within our experimental error of ±33%.

Let us now discuss why the oxygen partial pressure in the annealing ambient does not influence the Si self-diffusion in SiO_2 significantly. The diffusion coefficient of oxygen in SiO_2 is at least four orders of magnitude larger than the self-diffusion coefficient of Si for the temperatures 1200 and 1250°C [4, 61]. Therefore, a fraction of oxygen atoms in the annealing ambient enters SiO_2 from the front surface and diffuse across the thickness of the SiO_2 film to reach the Si/ SiO_2 interface and forms additional SiO_2 bonds by reacting with

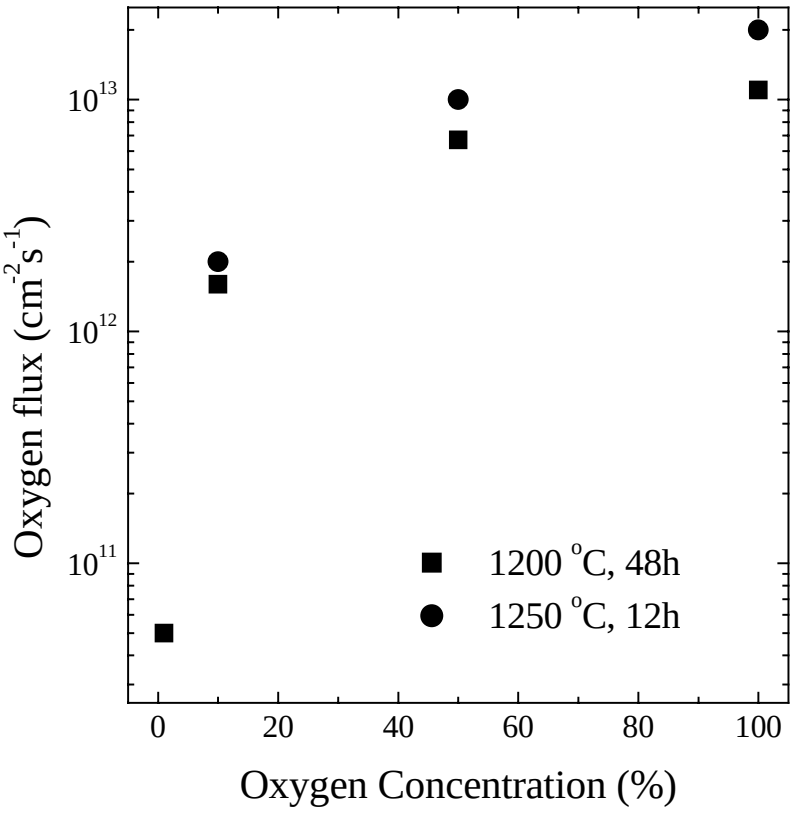

Figure 4.7: Average oxygen flux in SiO_2, which was estimated from the change in the oxide thickness, as a function of the oxygen concentration in the annealing ambient.

the Si substrate [62]. There are some Si species going up from the Si/SiO_2 interface to SiO_2 as was confirmed in ref. 15. However, ^{30}Si diffusers (the $^{nat}SiO_2/^{28}SiO_2$ interface) in our experiment situate so far away (650 nm) from the Si/SiO_2 interface that practically no Si species emitted from the Si/ SiO_2 interface reaches the region where ^{30}Si diffusion is taking place. Consequently, we need to focus on the effect of oxygen species going through in the direction from the top surface to the Si/SiO_2 interface on the diffusion of ^{30}Si. Theory predicts that the majority of oxygen in SiO_2 diffuses in the form of O_2 molecules and the minority in the form of atomic oxygen [63, 64, 65, 66]. None of these theories of oxygen diffusion in SiO_2 predicts strong interaction of diffusing oxygen with silicon atoms forming the SiO_2 network. The average flux of oxygen in SiO_2 during our diffusion annealing can be estimated simply from the total annealing time and the change of the oxide thickness before and after the annealing. The thickness change was measured accurately using an optical interferometer. As shown in Fig. 4.7, the average flux of oxygen going through the SiO_2 changes by an order of magnitude between 1 and 100% oxygen fractions in Ar. However, the oxygen flux as large as 10^{13} $cm^{-2}s^{-1}$ for 100% oxygen annealing was not significant enough to change $D^{SD}_{Si(th)}$ by the amount larger than our experimental error of 33%. This observation is in accordance with the above-mentioned theories which predict little interaction between the diffusing oxygen and silicon forming the network. It should be also pointed out that our recent experiment[15] has indicated that SiO molecules diffuse much faster than substitutional Si atoms in SiO_2, because SiO molecules diffuse predominantly through interstitial sites with frequent atomic exchange interactions with the substitutional Si atoms as implied by the recent first-principle calculation of boron diffusion in SiO_2 [22].

The results are consistent with the theoretical prediction that oxygen diffuses rapidly through predominantly the interstitial sites without interacting with Si atoms formed SiO_2 network [63]. Our experimental results, which contradict Mathiot's argument, indicate that oxygen in an annealing ambient does not have an influence on SiO_2.

So far, we have determined the accurate values of Si self-diffusivity in SiO_2 under thermal equilibrium condition using the $^{nat}SiO_2/^{28}SiO_2$ isotope heterostructures. As mentioned above, Mathiot *et al.* recently reported Si self-diffusivity in SiO_2 was obtained using the method similar to ours [13]. However, their values are still much higher than the values obtained in this chapter. Although Mathiot *et al.* argued that the origin of the difference between our and their values was the oxygen including in the annealing ambient, it was shown in this section that the oxygen concentration does not have influence on Si self-

diffusion in SiO_2. Therefore, the cause of the difference of Si self-diffusivity is not oxygen in the annealing ambient. Next chapter discusses an effect of the Si/SiO_2 interface on Si self-diffusion in SiO_2 and shows that the difference of Si self-diffusivity can be explained by the effect of the interface.

Chapter 5

Effect of the Si/SiO_2 interface on Si self-diffusion

5.1 Effect of the interface in ^{30}Si-implanted $^{28}SiO_2$

5.1.1 Introduction

We shall solve the discrepancies among Si self-diffusivity reported by several authors [9, 10, 11, 13, 14, 15] (shown in Fig. 4.1) in this chapter. Candidates of the cause of these discrepancies are differences in oxide thickness, SiN cappings, and Si diffusion markers.

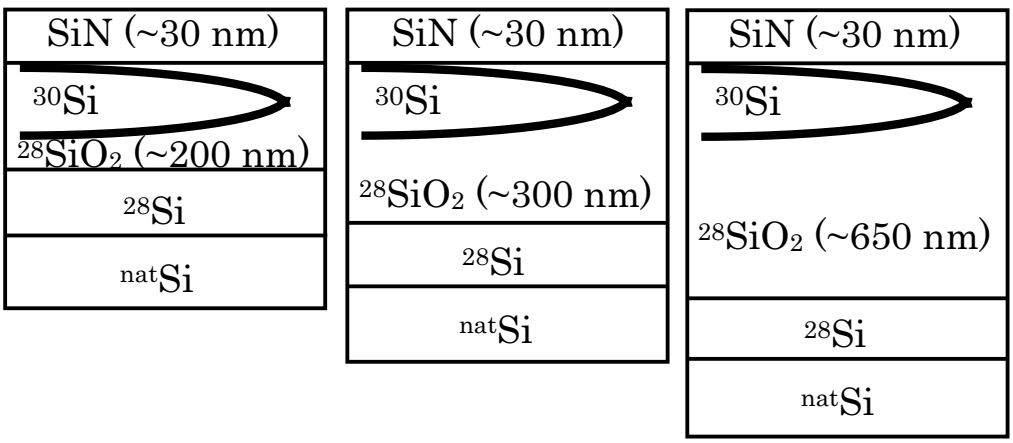

Figure 5.1: Structures of ^{30}Si-implanted samples

Table 5.1: Experimental method

	This work	Jaoul[12]	Tsoukalas[14]	Mathiot[13]
Oxide thickness	650 nm	Bulk	170 nm	200 nm
SiN capping	w/o	w/o	w/	w/
Si diffusion marker	Heterostructure	Heterostructure	Implanted ^{30}Si	Heterostructure

Little attention has been given to the oxide thickness, in the case of SiO_2 on the Si substrate, but we should not overlook the fact that the difference in the oxide thickness could influence the Si self-diffusion in the oxide. In this chapter, Si self-diffusion in SiO_2 was studied using ^{30}Si-implanted $^{28}SiO_2$ layer of the thicknesses 200, 300, and 650 nm with and without ∼30 nm thick SiN layers.

5.1.2 Experiment

These six samples prepared as described in § 2.1.2 were annealed at temperatures between 1150 and 1250°C in flowing Ar with 1% oxygen, followed by SIMS measurement.

5.1.3 Results and discussions

Figures 5.2 and 5.3 show the ^{30}Si depth profiles of samples before and after diffusion annealings of 24 h at 1250 °C and 168 h at 1200 °C, respectively. The diffusion profiles of the uncapped samples show very little dependence on the $^{28}SiO_2$ thickness as shown in Figs. 5.2(b) and 5.3(b). On the other hand, the silicon nitride capped samples demonstrate a strong dependence on the thickness of the $^{28}SiO_2$ layer as shown in Figs. 5.2(a) and 5.3(a). In the silicon nitride capped samples, the 200-nm-thick $^{28}SiO_2$ layer leads to the broadest diffusion profile. Consequently the thinner the $^{28}SiO_2$ layer is, the broader

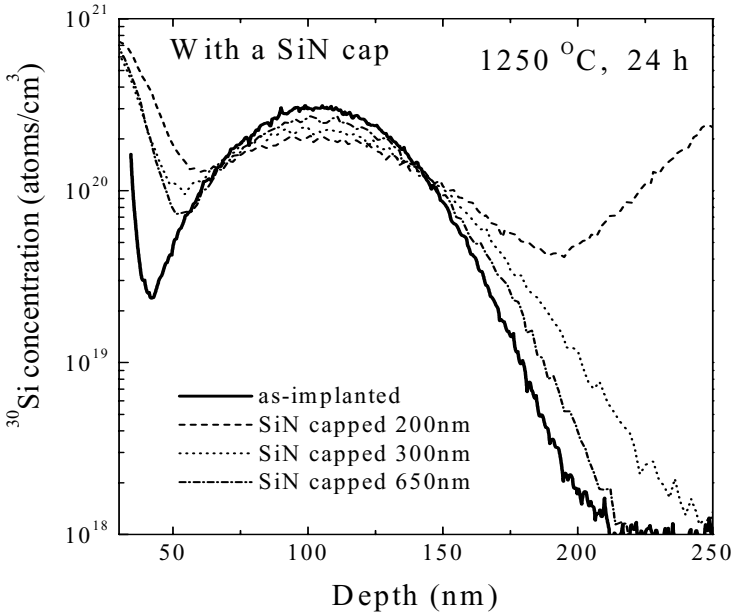

(a)

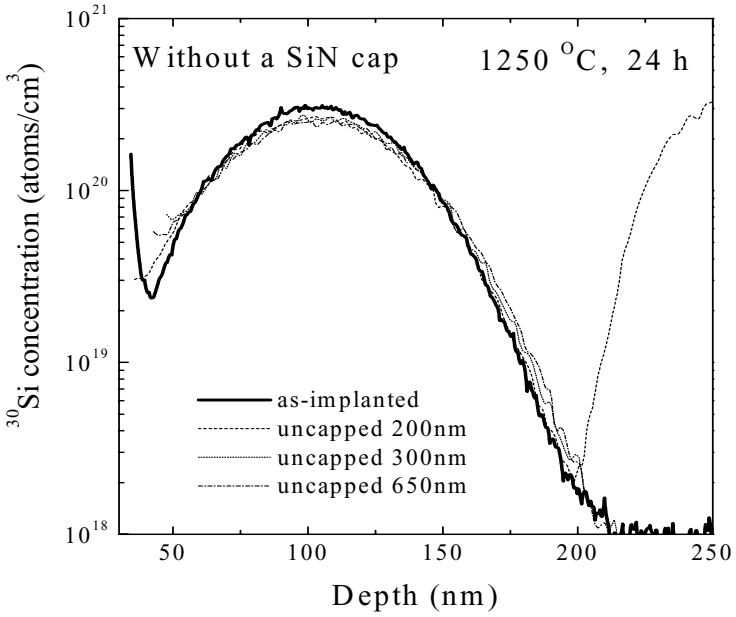

(b)

Figure 5.2: SIMS profiles of before and after annealing at 1250°C for 24 h:(a) of the samples with the SiN cap, (b) without the cap, the profiles are shifted so that the peaks of profiles agree with that of the profile of the samples with the SiN cap .

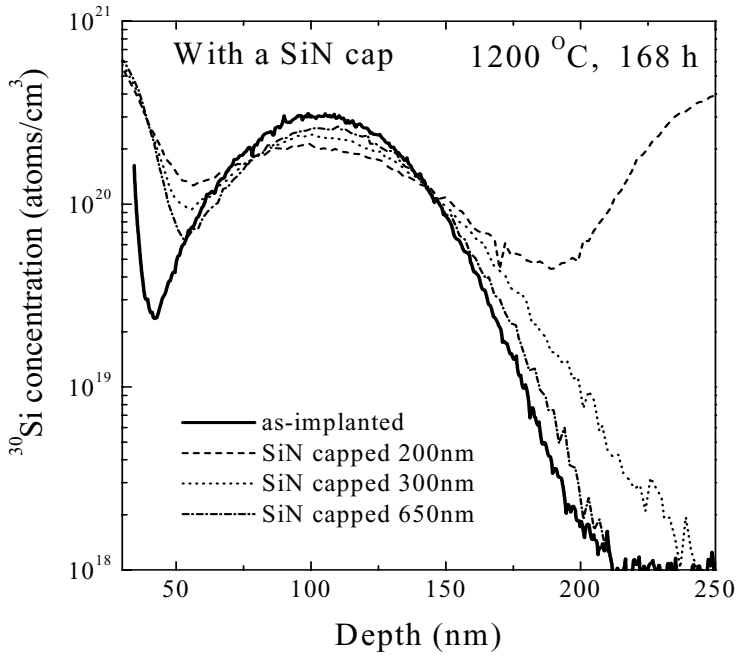

(a)

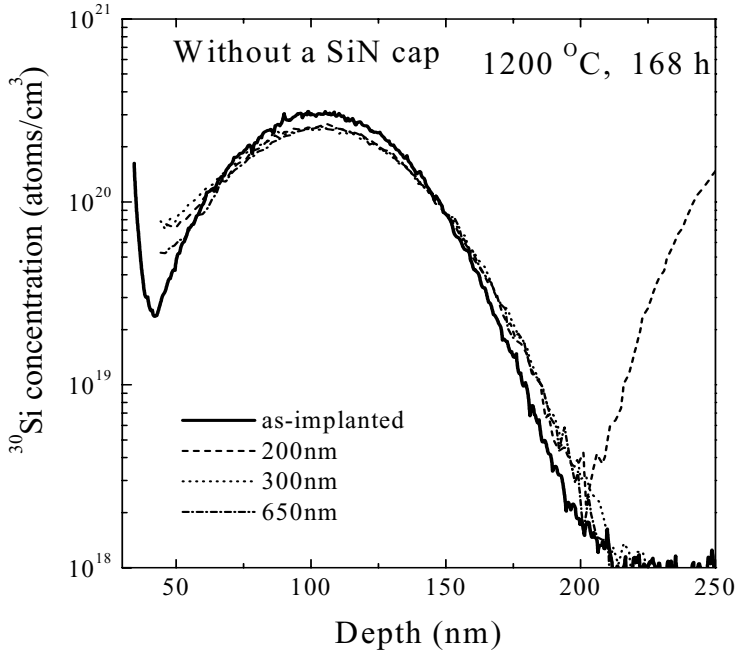

(b)

Figure 5.3: SIMS profiles of before and after annealing at 1200°C for 168 h:(a) of the samples with the SiN cap, (b) without the cap, the profiles are shifted so that the peaks of profiles agree with that of the profile of the samples with the SiN cap.

the diffusion profile becomes. In other words, the shorter the distance from the Si/SiO_2 interface, the higher the diffusivity in the silicon nitride capped sample. This tendency was observed consistently for other temperatures probed in this study.

In the 200 nm sample, the concentration of ^{30}Si increases at both sides, as shown in Figs. 5.2 and 5.3. At left side (the interface between ^{nat}SiN and $^{28}SiO_2$), ^{30}Si diffuse from the ^{nat}SiN layer. On the other hand, at the right side, which is near the $^{28}SiO_2/^{28}$Si interface, the increase of ^{30}Si was due to ^{30}Si which diffuses through the ^{28}Si from the $^{28}Si/^{nat}$Si interface, because Si diffusivity in crystalline Si [54] is much higher than that in SiO_2.

Assuming a constant diffusivity, simulated profiles were fitted to SIMS profiles in order to determine Si self-diffusivity (Fig. 5.4). Estimated Si self-diffusivity for each sample as a function of temperature are shown in Fig. 5.5.

It is shown that the diffusivity values of the uncapped samples are lower than that of silicon-nitride-capped samples with no thickness dependence and that they agree with the $D_{Si}^{SD} = 0.8 \exp(-5.2 \text{ eV/kT}) \text{ cm}^2/\text{s}$ obtained in chapter 4, which was determined using $^{nat}SiO_2/^{28}SiO_2$ structures having $^{28}SiO_2$ thickness (i.e., the distance between diffusing ^{30}Si and Si/$^{28}SiO_2$) equal to 650 nm. This observation eliminates concerns related to diffusion under a non-stoichiometric condition (excess Si in SiO_2) and to implanted damage associated with ^{30}Si implantation into the $^{28}SiO_2$ employed in this study. In order to further assure our equilibrium condition, we studied samples with two implanted doses, $1 \times 10^{14}\text{cm}^{-2}$ and $2 \times 10^{15}\text{cm}^{-2}$, and confirmed that D_{Si}^{SD} remains unchanged.

On the other hand, D_{Si}^{SD} in the capped samples changes with the distance of Si diffusers from the Si/SiO_2 interface. As expected, D_{Si}^{SD} in the capped samples with the 650-nm SiO_2 agrees with that of previous section with no capping layer because theirs is the true equilibrium value of D_{Si}^{SD} in semiconductor-grade SiO_2 as we claimed earlier [9]. Mathiot et al's argument [13] that the D_{Si}^{SD}=0.8 exp(-5.2 eV/kT) cm^2/s of eq. (4.2) represents diffusion in an oxygen-rich condition, not the true equilibrium condition, fails since D_{Si}^{SD} obtained with 650-nm thickness agrees regardless of the presence of silicon-nitride capping and the partial pressure of O_2 in Ar atmospheres. In addition, our data for the capped 200-nm-thick sample, the same thickness investigated by Mathiot et al. [13], are very close to their values 33.2 exp(-5.34 eV/kT) cm^2/s. Mathiot el al. did not take into account the SiO_2 thickness dependence of D_{Si}^{SD}, and this led them to their above argument. Figure 5.5 also shows the data of Tsoukalas et al. [14], which was obtained for a capped 170-nm-thick SiO_2 layer. Their D_{Si}^{SD} is larger than our D_{Si}^{SD} obtained for the capped 200-nm sample

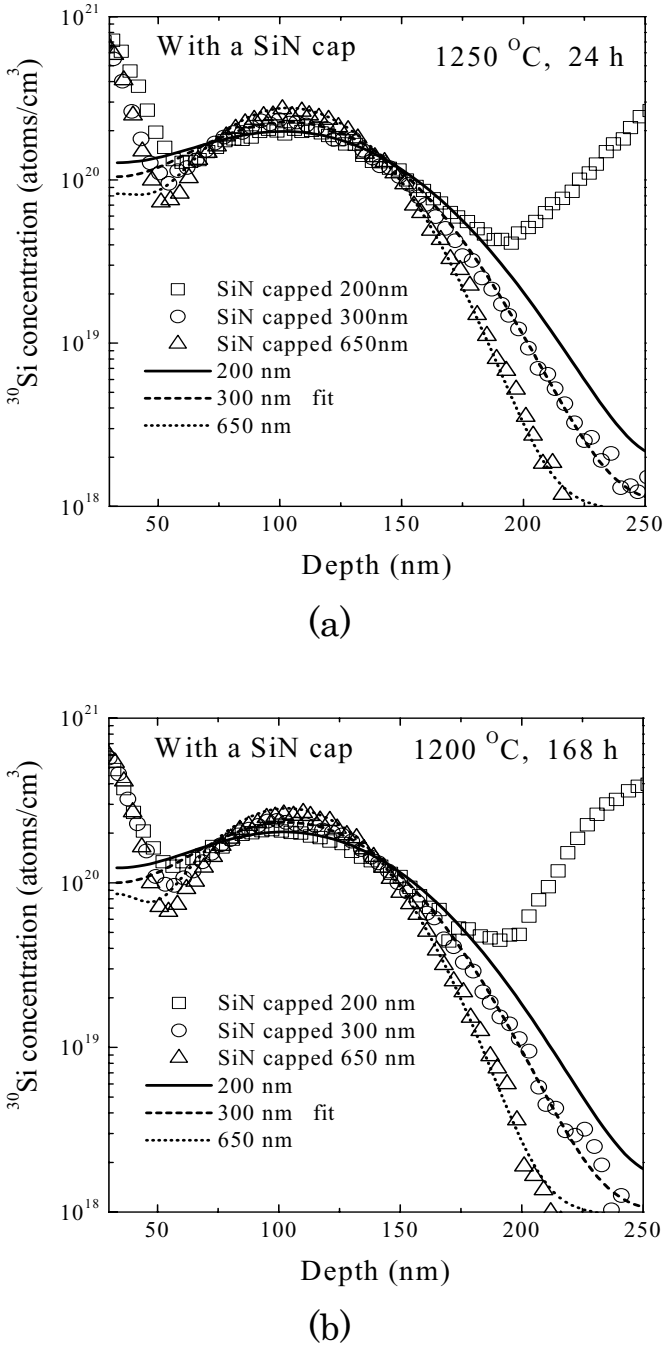

Figure 5.4: Open squares, open circles, and open triangles are SIMS profiles obtained in ^{30}Si-implanted $^{28}SiO_2$ layers of 200 nm, 300 nm, and 650 nm thickness, respectively. Lines are simulated profiles for each experimental profile. These simulated profiles were obtained assuming constant diffusivity.

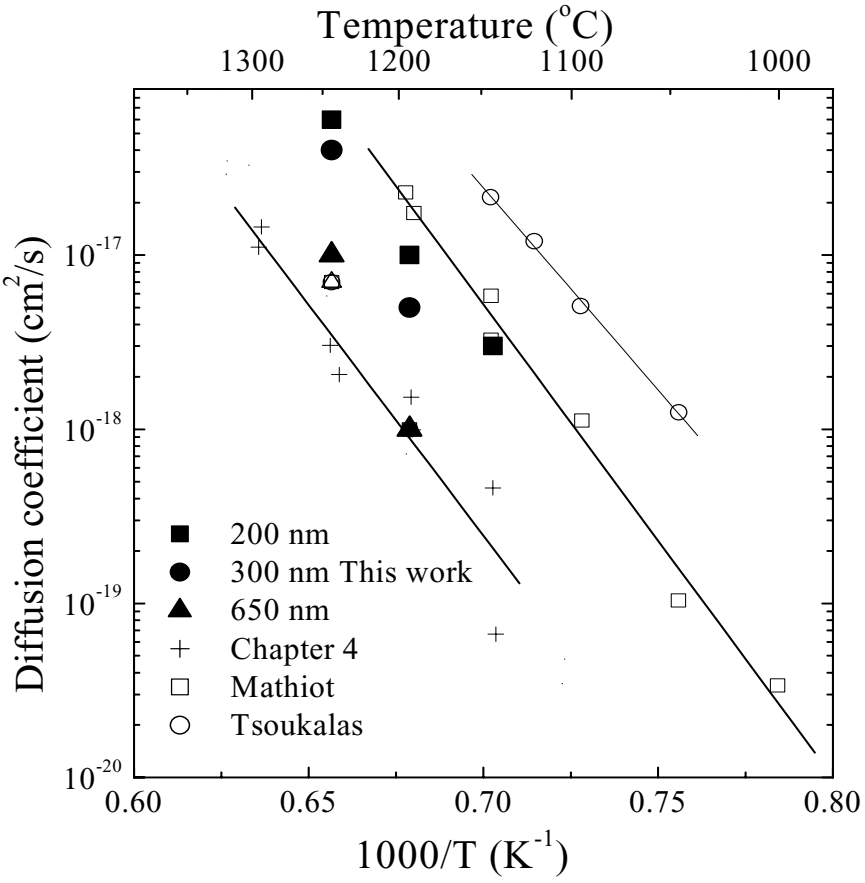

Figure 5.5: Silicon self-diffusion coefficient in SiO_2 :Filled squares, circles and triangles represent the values obtained using ^{30}Si-implanted $^{28}SiO_2$ layer of 200 nm, 300 nm, and 650 nm thickness with SiN capping layers, respectively. + represents the values under the thermal equilibrium condition obtained in chapter 4, and that of Ref 13 (□) and Ref 14 (○) are also shown.

because the distance to the Si/SiO_2 is smaller by 30 nm compared to the 200-nm-thick one.

Let us now discuss why there is thickness dependence of D_{Si}^{SD} for the capped samples but no such dependence for uncapped layers. We obtained the same D_{Si}^{SD} for implanted ^{30}Si and stoichiometric $^{nat}SiO_2/^{28}SiO_2$ heterostructures, which, as mentioned above, eliminated the possibility of non-stoichiometry (excess Si due to implantation). We have also eliminated the possibility of implantation damage for the same reason. On the other hand, it is

possible that the stress on SiO_2 layers changes depending on the presence of the silicon-nitride capping layers. The diffusivity D'^{SD}_{Si} under stress can be described by $D'^{SD}_{Si}=D^{SD}_{Si}$ exp ($-PV_d/kT$), where P is the stress and V_d is the activation volume for diffusion in SiO_2, which has been estimated to be a few ten A^3 for oxygen diffusion [67, 68, 69]. At 1250 °C, we have observed a factor-of-six enhancement of D'^{SD}_{Si} for 200 nm with respect to D^{SD}_{Si} for 650 nm. P$\sim 10^{10}$ dyne/cm^2 of stress is required in order to obtain such enhancement. This required stress of P$\sim 10^{10}$ dyne/cm^2 is unrealistically large for just having a 30 nm-silicon nitride layer on top; the typical stress expected for such a case is much less than 10^{10}dyne/cm^2. For example, the stress of $\sim 10^{10}$ dyne/cm^2 has been reported in the oxidation of Si nano-pillers, where a nano-silicon rod is surrounded completely by SiO_2 [70]. Such a large stress cannot result from capping with a silicon nitride film of only ∼30-nm thickness. We therefore conclude that the stress cannot account for the thickness dependence of D^{SD}_{Si} observed for the capped samples. In addition, we will discuss time dependence of Si self-diffusion in SiO_2 in the following section, which will show that the stress is not origin of the dependence of Si self-diffusion on the oxide thickness.

The only remaining possibility is the effect of Si species emitted at the Si/SiO_2 interface that diffuse into the SiO_2 layer to enhance the ^{30}Si self-diffusivity in SiO_2. In the case of the uncapped sample, oxygen species incorporated into the SiO_2 from the oxygen containing atmosphere diffuse across the thickness of the SiO_2. When oxygen atoms arrive at the Si/SiO_2 interface region, they recombine with the Si species emitted from the Si/SiO_2 to form additional SiO_2. Therefore, Si species emitted at the Si/SiO_2 interface never have an opportunity to reach the region where ^{30}Si diffusion is taking place. Therefore, there is no enhancement of D^{SD}_{Si} when SiO_2 is not capped with the nitride. On the other hand, for the case of the nitride-capped sample, the cappings act as barriers against oxygen incorporation from the annealing atmosphere, i.e., there is no oxygen species coming into the SiO_2. Therefore, Si species emitted from the Si/SiO_2 have no extra oxygen species to recombine with to form additional SiO_2 and diffuse freely into the region where ^{30}Si was implanted and Si self-diffusion was observed. Our belief is that these extra Si species coming from the Si/SiO_2 interface are the source of the enhanced D^{SD}_{Si} for thin SiO_2 samples. Indeed, there have been a number of suggestions based on experimental speculations and theoretical predictions for emission of Si species from the Si/SiO_2 interface to SiO_2 [2, 3, 50, 52, 60, 71]. In our view, SiO generated at the Si/SiO_2 interface via the reaction $Si + SiO_2 \rightarrow 2SiO$ [60, 71] is the most likely candidate as the dominant Si species arriving from the interface. In this context, the present work should be regarded

as the first experimental evidence of Si species emission from the Si/SiO_2 interface to SiO_2 to enhance Si self-diffusion.

It was reported that main desorbing product during decomposition of SiO_2 on Si is SiO, which was shown by using laser-induced fluorescence (LIF) [28] or thermal desorption spectroscopy (TDS) [72]. Furthermore, Kobayashi *et al.*, reported that other species such as H_2, H_2O, CO, O_2, SiO_2, and Si_2O_3 did not show any TDS signals in the range of the SiO desorption temperature [72]. In addition, Tromp *et al.*, [73] and Liehr *et al.*, [74] investigated the decomposition of SiO_2 on Si under ultrahigh-vacuum annealing conditions by means of ion scattering and microscopy techniques, and showed that SiO_2 was not removed from the SiO_2 surface but from the Si/SiO_2 interface by the formation and lateral growth of holes in the oxide, exposing regions of atomically clean Si, while the surrounding oxide retains its initial thickness. It is known that the decomposition rate of SiO_2 is enhanced by the existence of Si beam [75]. Therefore, it is reasonable to conclude that the reaction Si + SiO_2 $\rightarrow$ 2SiO occurs at the Si/SiO_2 interface during the decomposition of SiO_2 on Si.

High temperature annealing in an oxygen-deficient ambient leads to the decomposition of SiO_2 on Si [28]. Therefore, with the SiN cap, which acts as barriers, the reaction occurs at the Si/SiO_2 interface during high temperature annealing.

5.1.4 Time dependence of Si self-diffusion

We have also investigated the time dependence of Si self-diffusion in SiO_2. Figure 5.6 shows the comparison between SIMS profiles after annealing at 1250°C for 6 and 24 h and calculated results. These calculated profiles were obtained by assuming constant diffusivity. The Si self-diffusivity in SiO_2 as a function of annealing duration is listed in table 5.2. Table 5.2 indicates that Si self-diffusivity in SiO_2 obtained for long time annealing is larger than that of short time annealing, in other words, Si self-diffusivity obtained naively in this simple analysis increases with annealing duration.

The dependence of Si self-diffusivity on time can be explained by the effect of SiO molecules generated at the Si/SiO_2 interface and diffusing into the oxide. If SiO molecules do not diffuse in SiO_2 for the given temperature and the duration of annealing, the concentration of SiO molecules in SiO_2 does not spread uniformly over the SiO_2. In this case concentration of SiO in SiO_2 increases with annealing time and Si self-diffusion becomes

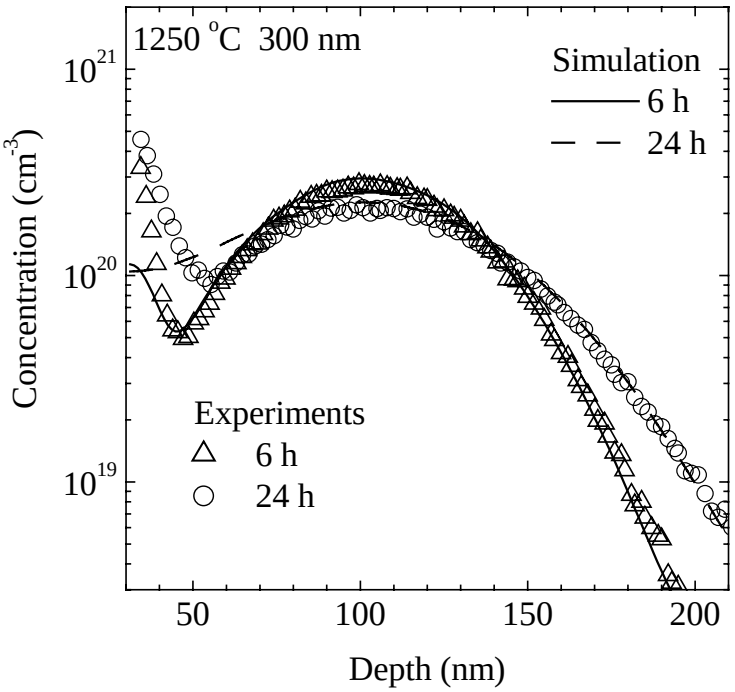

Figure 5.6: Comparison between experimental and fitted profiles of ^{30}Si after 6 or 24 h annealing at 1250 °C in ^{30}Si implanted 300 nm thick $^{28}SiO_2$ with the SiN cap. Solid curves are the fits.

faster as the SiO concentration increases. Therefore, Si self-diffusivity increases with the annealing time. We have constructed a diffusion model of Si in SiO_2 which involves SiO

Table 5.2: Si self-diffusivity obtained by assuming constant diffusivity (300 nm thick sample)

	1200°C	1250°C
Short annealing	3×10^{-18} cm^2/s (72 h)	1×10^{-17} cm^2/s (6 h)
Long annealing	4.5×10^{-18} cm^2/s (168 h)	4×10^{-17} cm^2/s (24 h)

molecules. We will show that the model can explain the dependence of Si self-diffusion on the annealing time quantitatively.

Let us now discuss why we conclude that the stress is not the cause of the dependence of Si self-diffusion on the oxide thickness. If the stress enhances Si self-diffusion, Si self-diffusivity would decrease with time because the stress decreases with time due to the viscosity flow of the oxide. Therefore, the dependence of Si self-diffusion on the oxide thickness is not due to the stress between the SiN/SiO_2 interface.

5.2 Model of Si self-diffusion in SiO_2

These experimental results indicate that Si self-diffusion in SiO_2 is enhanced by SiO molecules generated at the Si/SiO_2 interface. In order to confirm that, we have constructed a model of Si self-diffusion in SiO_2 taking into account SiO molecules. The model is as follows [16].

Fig. 5.7 shows the enhancement of Si self-diffusion in SiO_2 due to the existence of SiO molecules. Without SiO molecules, in other words, far from the Si/SiO_2 interface or in the oxidation ambient, ^{30}Si atoms forming the SiO_2 network moves to an adjacent site with the help of defects as a thermal equilibrium self-diffusion. The process can be described by

$$^{30}\mathrm{Si(sub)} + {}^{28}\mathrm{Si(sub)} \Leftrightarrow {}^{28}\mathrm{Si(sub)} + {}^{30}\mathrm{Si(sub)}, \tag{5.1}$$

where (sub) means atoms which are located substitutionally forming SiO_2 network. In addition, as shown in Fig. 5.7(b), with SiO molecules, ^{28}SiO molecules interact with ^{30}Si atoms forming the SiO_2 network to form ^{30}SiO via the kick-out reaction:

$$^{30}\mathrm{Si(sub)} + {}^{28}\mathrm{SiO(int)} \Leftrightarrow {}^{28}\mathrm{Si(sub)} + {}^{30}\mathrm{SiO(int)}, \tag{5.2}$$

where (int) means molecules which are located in SiO_2 interstitially.

Based on the model, we solve the following diffusion equations for the concentration of ^{30}Si, ^{28}SiO, and ^{30}SiO.

$$\frac{\partial C_{^{30}\mathrm{Si}}}{\partial t} = \frac{\partial}{\partial x}\left(D^{\mathrm{SD}}_{\mathrm{Si\ (th)}} \frac{\partial C_{^{30}\mathrm{Si}}}{\partial x} \right) - R, \tag{5.3}$$

$$\frac{\partial C_{^{30}\mathrm{SiO}}}{\partial t} = \frac{\partial}{\partial x}\left(D_{\mathrm{SiO}} \frac{\partial C_{^{30}\mathrm{SiO}}}{\partial x} \right) + R, \tag{5.4}$$

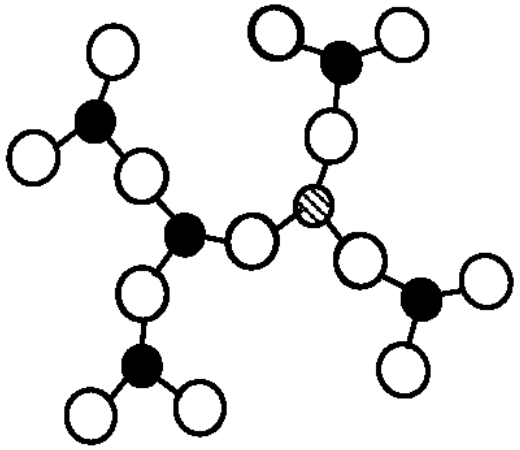

(a)

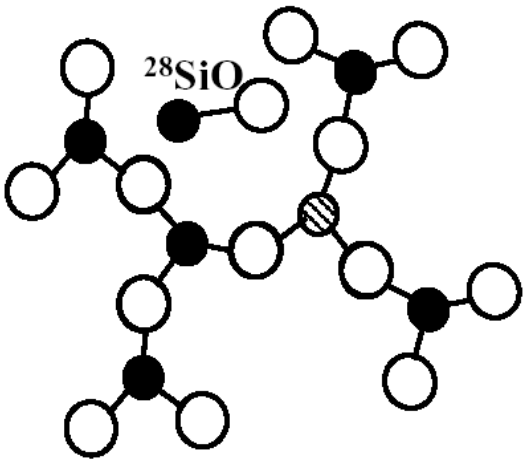

(b)

Figure 5.7: Si diffusion mechanism with SiO molecules: (a) without SiO molecules, ^{30}Si move to an adjacent Si site involving defects. (b) SiO molecules diffuse rapidly with interacting with oxide network, i.e., ^{28}SiO interacts with ^{30}Si to form ^{30}SiO which diffuses faster than Si.

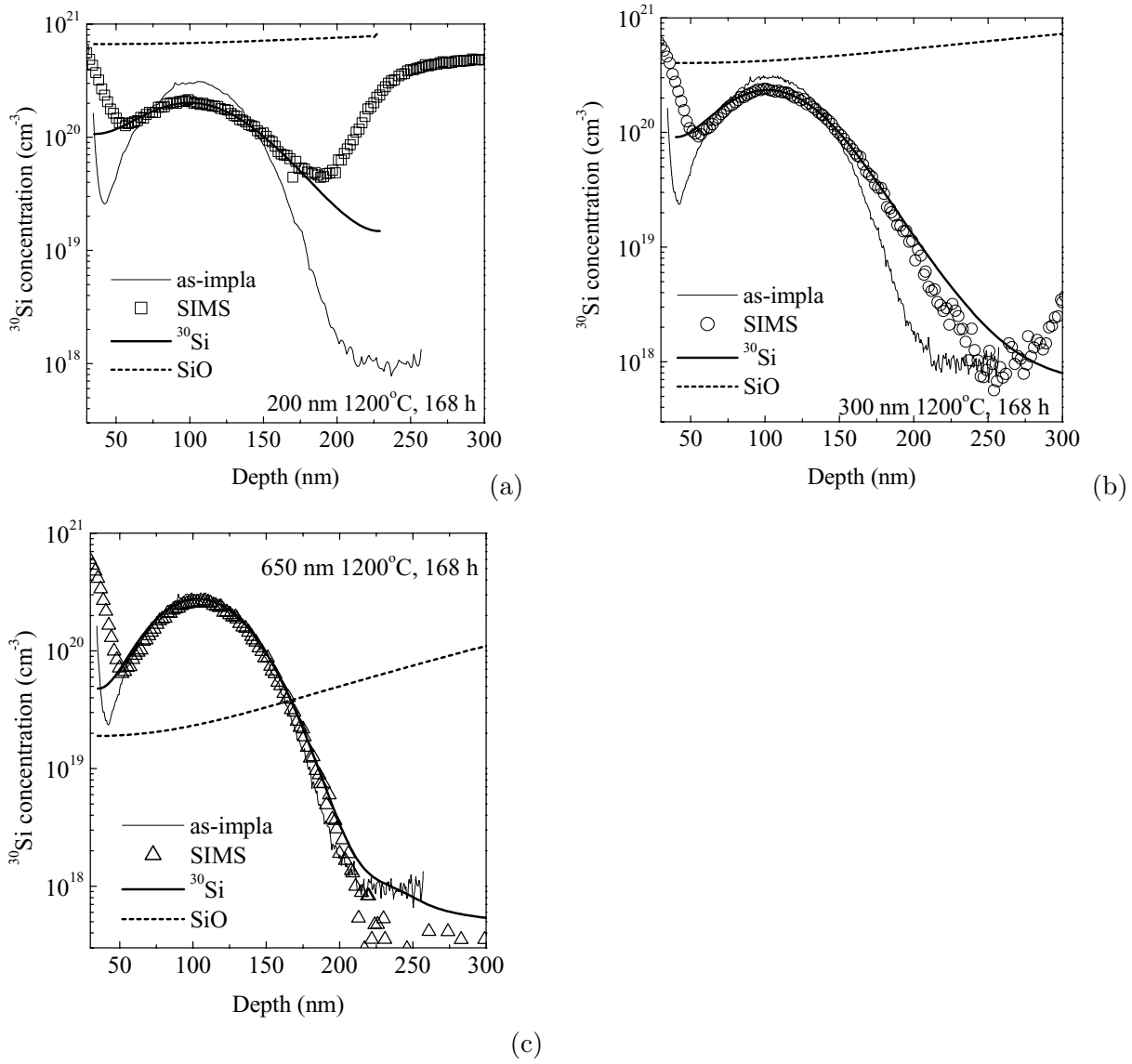

Figure 5.8: Comparison between SIMS profiles of ^{30}Si and simulated profiles taking into account the effect of SiO molecules arriving from $^{28}SiO_2/^{28}$Si interfaces in (a) 200 nm thick sample with the SiN cap, (b) 300 nm thick sample with the SiN cap, and (c) 650 nm thick sample with the SiN cap after annealing 1200 °C for 168 h.

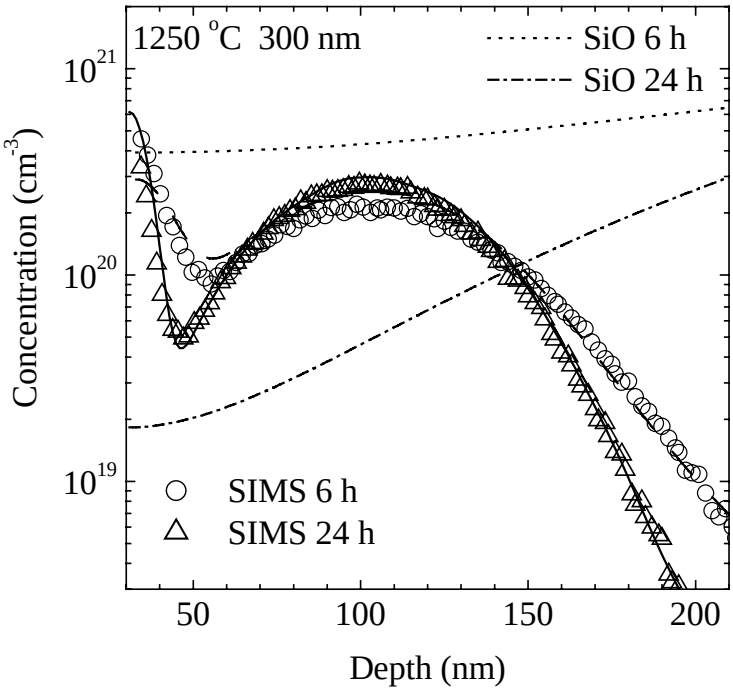

Figure 5.9: Comparison between experimental and simulated results after 6 or 24 h annealing at 1250 °C in ^{30}Si implanted 300 nm thick $^{28}SiO_2$ with the SiN cap. Solid lines are simulated SiO profiles and ^{30}Si profiles.

$$\frac{\partial C_{^{28}\mathrm{SiO}}}{\partial t} = \frac{\partial}{\partial x}\Big(D_{\mathrm{SiO}}\frac{\partial C_{^{28}\mathrm{SiO}}}{\partial x}\Big) - R, \tag{5.5}$$

where R is the reaction term and is described by

$$R = k_f C_{^{30}\mathrm{Si}} C_{^{28}\mathrm{SiO}} - k_b C_{^{30}\mathrm{SiO}}. \tag{5.6}$$

In these equations, C_x (x=^{30}Si,^{28}SiO, and ^{30}SiO) is the concentration of corresponding species, and $\mathrm{D}^{\mathrm{SD}}_{\mathrm{Si(th)}}$ is the Si self-diffusivity under the thermal equilibrium condition, $\mathrm{D}_{\mathrm{SiO}}$ is the diffusivity of SiO molecules, and k_f and k_b are the forward and backward rate constants of eq. (5.2). The Si self-diffusivity is, as a whole, described by

$$D^{\mathrm{SD}}_{\mathrm{Si}} = D^{\mathrm{SD}}_{\mathrm{Si\ (th)}} + D^{\mathrm{SD}}_{\mathrm{SiO}}\frac{C_{^{28}\mathrm{SiO}}}{C^{\circ}_{\mathrm{SiO}}}, \tag{5.7}$$

where $D^{\mathrm{SD}}_{\mathrm{SiO}}$ is the self-diffusivity of Si via SiO molecule and has a following relation

$$D^{\mathrm{SD}}_{\mathrm{SiO}} = D_{\mathrm{SiO}} \frac{C^{\circ}_{\mathrm{SiO}}}{N_{\circ}}, \tag{5.8}$$

where $N_{\circ}$ is the number of SiO_2 molecules in a unit volume of SiO_2. Here, C°_{SiO} denotes the maximum concentration of SiO interstitials in SiO_2 and is described as $C^{\circ}_{\mathrm{SiO}} = 3.6\times10^{24}$ exp(-1.07 eV/kT), which is estimated from the product of the interstitial segregation coefficient for the Si/SiO_2 interface [76] and the equilibrium self-interstitial concentration in Si [77]. The experimentally obtained $D^{\mathrm{SD}}_{\mathrm{Si(th)}}$ (eq. (4.2)) was used for the simulation. In the simulation, the boundary condition for ^{28}SiO(i) at the $^{28}Si/^{28}SiO_2$ interface is given by $C_{^{28}\mathrm{SiO(x=interface)}} = C^{\circ}_{\mathrm{SiO}}$ to describe the generation of SiO at the interface. The amount of ^{30}SiO(i) arriving at the $^{28}Si/^{28}SiO_2$ interface is so small that the mixing of ^{28}Si with ^{30}Si at the interface was neglected. The boundary condition at the nitride-capped surface was represented by a zero-flux condition because the cappings act as barriers. Reaction (5.2) was assumed to be so fast that the local equilibrium of the reaction was established, ($k_f C^{\mathrm{eq}}_{^{30}\mathrm{Si}} C^{\mathrm{eq}}_{^{28}\mathrm{SiO}} = k_b C^{\mathrm{eq}}_{^{30}\mathrm{SiO}}$) and hence the rate constants (k_f and k_b) were set to be large enough. Therefore, that leads to the relationship $k_f = k_b / C^{\mathrm{eq}}_{^{28}\mathrm{Si}}$. In addition, Si and SiO_2 are thermodynamically in equilibrium with SiO with a certain solubility in SiO_2, which only depends on temperature. At the interface, therefore, SiO is generated until this solubility value has been reached and a higher concentration of SiO leads to decomposition of SiO into Si and SiO_2. Interfacial reactions are generally much faster than one-dimensional diffusion away from an interface. Therefore, we assume that the generation rate of SiO at the interface is large enough so that the SiO concentration at the interface is fixed at C°_{SiO}. The only parameter obtained from the simulation to fit the experimental profiles of ^{30}Si is D_{SiO}. Equations (5.3)-(5.6) were solved numerically (see Appendix A).

Figure 5.8 shows simulated and experimental profiles of ^{30}Si after annealing at 1200°C for 168 h. Simulated profiles were obtained using a same D_{SiO}, which was only a fitting parameter, and simulation agreed well with the experimental profiles. This is in contrast to the self-diffusivity obtained assuming a constant diffusion coefficient for each profile, which increases with decrease of the $^{28}SiO_2$ thickness. In Figs. 5.8 and 5.9, the ^{28}SiO concentration obtained in the simulation are plotted. Figs. 5.8 and 5.9 indicate that the difference in the concentration of ^{28}SiO leads to the considerable change of Si self-diffusivity. From the simulation results, we found that the concentration of ^{28}SiO depends on the distance from the Si/SiO_2 interface and annealing time, therefore, the Si self-

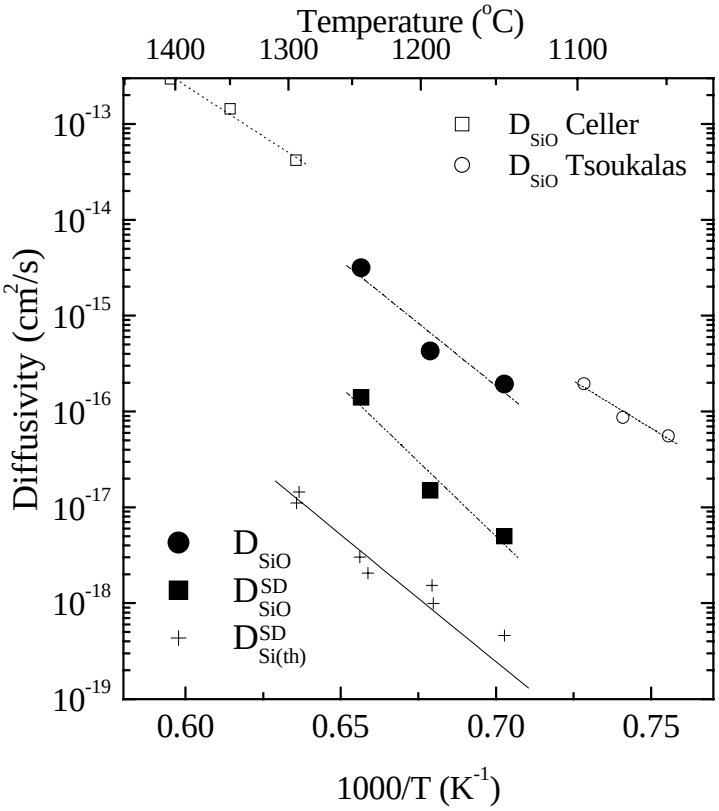

Figure 5.10: Temperature dependencies of the Si diffusion coefficients obtained in this study with those reported previously in the literature. Filled circles (•) and filled squares (■) represent the present results for D_{SiO} and D^{SD}_{SiO}, respectively. $D^{SD}_{Si(th)}$ obtained in chapter 4 are also plotted as (+). The previously reported values are the SiO diffusivities from refs. 60 (□) and 53 (○) (thermally migrated impurities and defect evolutions as markers, respectively).

diffusivity depends on the distance and annealing time. Note that the time dependent diffusivity (Fig. 5.6) which leads to differernt diffusivity as a function of the annealing duration (Table 5.2) using naive analysis can now be fitted very well by present diffusion model using the same set of parameters as shown in Fig. 5.9.

The values of D_{SiO} estimated by the simulation is given by

$$D_{SiO} = 3.4 \times 10^2 \exp\Big(-\frac{5.2\text{eV}}{kT}\Big)(\text{cm}^2/\text{s}), \tag{5.9}$$

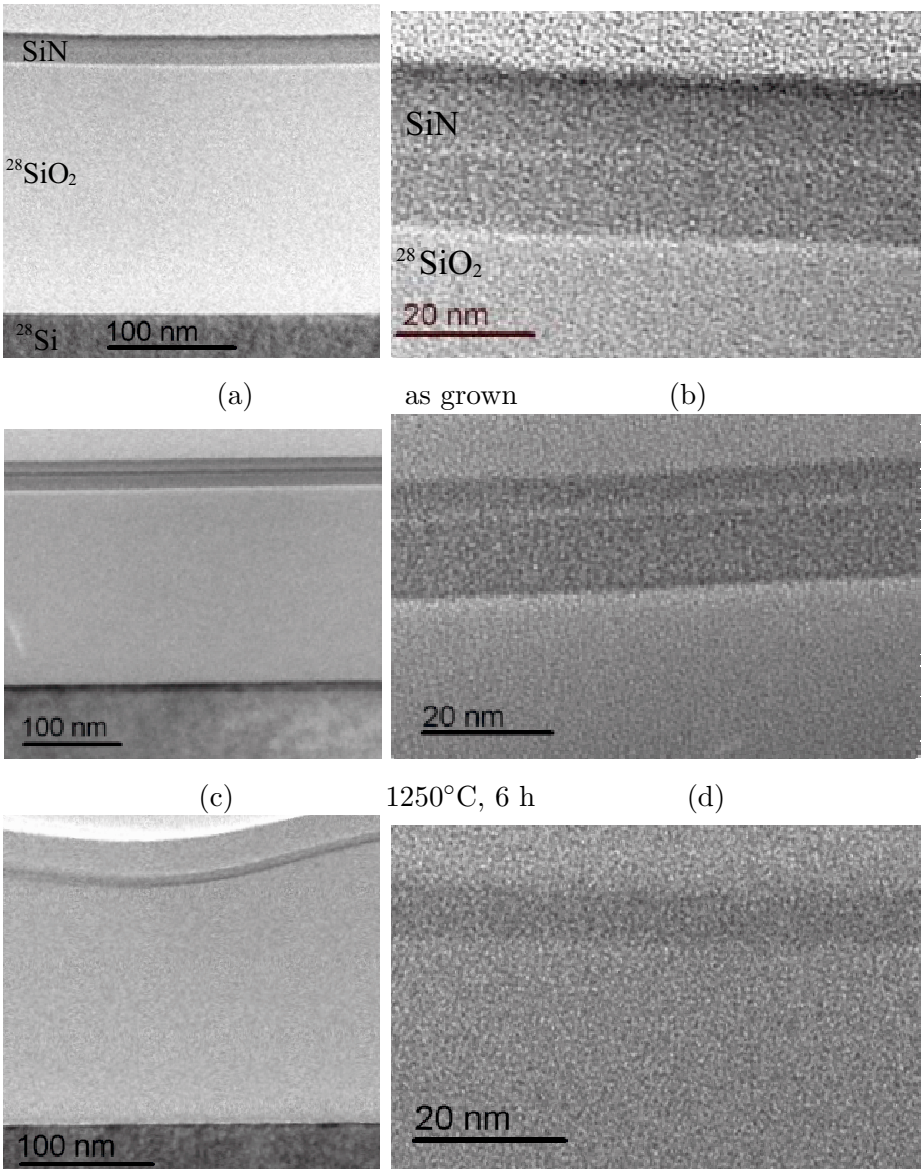

Figure 5.11: Cross-sectional TEM images of 200-nm samples capped with a 30-nm-thick SiN before and after annealing process. Right figures are the magnification of the SiN/$^{28}SiO_2$ interface.

and, are shown in Fig. 5.10. In addition, the values of $D_{\mathrm{SiO}}^{\mathrm{SD}}$ are

$$D_{\mathrm{SiO}}^{\mathrm{SD}} = 4 \times 10^4 \exp\Big(-\frac{6.2\mathrm{eV}}{kT}\Big)(\mathrm{cm}^2/\mathrm{s}), \tag{5.10}$$

which are also shown in Fig. 5.10. The values of D_{SiO} obtained in this work were in agreement with the SiO diffusivities reported by Celler *et al.*[60] and Tsoukalas *et al.* [53]. Celler *et al.*[60] obtained the SiO diffusivity using thermally migrated impurities, and Tsoukalas *et al.* [53] estimated the SiO diffusivity from defect evolution indirectly.

Figure 5.11 shows transmission electron microscopy (TEM) images of 200 nm samples with a SiN cap before and after annealings at 1250°C for 6 and 24 h. After 24-h annealing, the interface between Si and SiO_2 did not become rough, on the other hand, the SiN/SiO_2 interface and the surface were roughened during 24-h annealing. The surface roughness of the samples after annealing was measured with atomic force microscopy (AFM) and the data were applied to the parameter of MRI model. In this way we took the surface roughness into account for the analysis of the SIMS profiles.

We have investigated the nitrogen concentration around the surface using electron energy-loss spectroscopy. As a result, with the exception of the darkest part in Fig. 5.11(f) nitrogen was not detected in the sample after annealing at 1250°C for 24 h. From the surface, the SiN layer was oxidized due to 1% oxygen in the annealing ambient. As a result, the concentration of nitrogen was reduced at the surface.

In our simulation, the concentration of total SiO molecules generated during annealing at 1250 °C for 24 h was $\sim 1.7\times10^{16}$ cm^{-2}, which was obtained by integration of the calculated SiO profile. The areal atomic density of Si(100) are simply estimated to be $\sim 6.8\times10^{14}$ cm^{-2}. Using these values, the number of Si atomic layers which were consumed via the reaction $Si + SiO_2 \rightarrow 2SiO$ was estimated to be ∼13, which corresponds to 1.8 nm of Si. The same number of SiO_2 layers were consumed via the reaction. To provide a comparison, the number of Si layers consumed during rapid thermal annealing (RTA) at 1050 °C for 1 min, which is the general annealing condition for post deposition annealing, was calculated to be ∼0.1 layer.

5.3 Effect of the interface in isotope heterostructures

5.3.1 Introduction

In the previous chapter, we have experimentally shown the dependence of Si self-diffusion in SiO_2 capped with SiN on the distance from the Si/SiO_2 interface using the ^{30}Si-implanted $^{28}SiO_2$ layer of 200, 300, and 650 nm thicknesses [15]. The dependence is as follows. With the SiN layer on the surface, the Si self-diffusivity increases as the $^{28}SiO_2$ thickness decreases. On the other hand, without the SiN layer, the Si self-diffusivity does not depend on the thickness, and the values of the diffusivity agree with the thermal Si self-diffusivity ($D^{SD}_{Si\,(th)}$) [9]. Specifically, with the SiN layer, the values obtained using the samples with the 650-nm-thick $^{28}SiO_2$ layer also showed good agreement with the $D^{SD}_{Si\,(th)}$.

In the present work, using the $^{nat}SiO_2/^{28}SiO_2$ isotope heterostructures, as shown in Fig. 5.12, the effect of the Si/SiO_2 interface was investigated. The objective of this experiment is to experimentally confirm that Si self-diffusion in SiO_2 does not depend on the oxide thickness but on the distance between ^{30}Si diffusers and the Si/SiO_2 interface. In the previous study[15], the oxide thickness was changed in order to vary the distance, while in the isotope heterostructures used in the present study, the total oxide thicknesses were the same (∼750 nm), as shown in Fig. 5.12.

5.3.2 Experiment

The $^{nat}SiO_2/^{28}SiO_2$ isotope heterostructures were grown in the manner shown in § 2.1.3. Note that each sample had the same total SiO_2 thickness (∼750 nm), as shown in Fig. 5.12. The samples were cut into 5×5 mm^2 pieces and annealed at 1200 and 1250°C under flowing Ar with a 1 % oxygen fraction, followed by SIMS measurement under the condition as mentioned above. The surface roughness of each sample before and after annealing was measured with atomic force microscopy (AFM).

5.3.3 Results and discussions

Figures 5.13 and 5.14 show the SIMS profiles of ^{30}Si in the isotope heterostructures after diffusion annealing. In these isotope heterostructures, the total oxide thickness of each sample was almost the same, while the thickness of the $^{28}SiO_2$ layer of each sample was varied: the distance between the $^{nat}SiO_2/^{28}SiO_2$ interface, at which Si self-diffusion

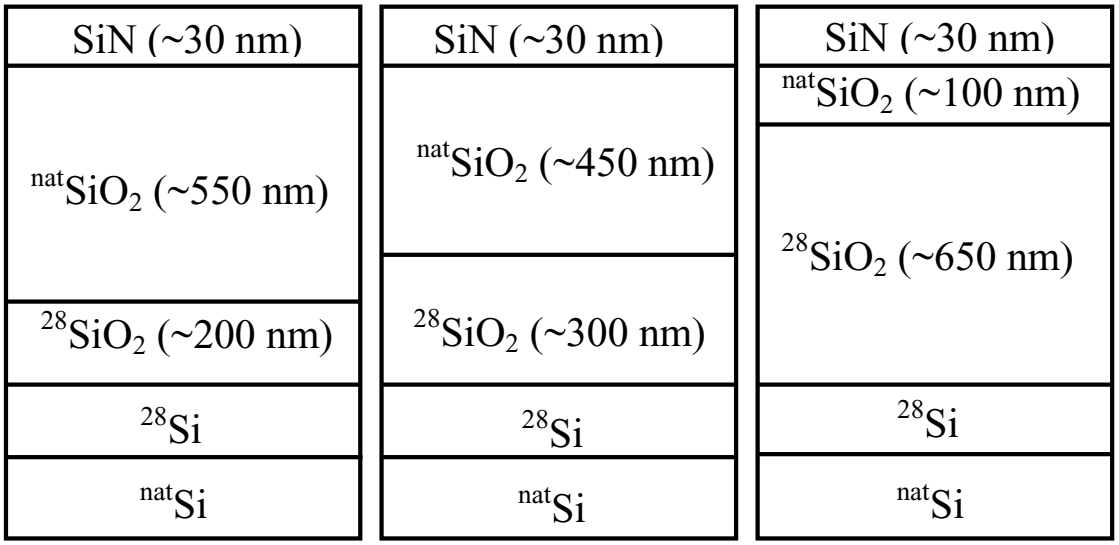

Figure 5.12: Sample structures of $^{28}SiO_2/^{nat}SiO_2$ heterostructures with the constant total oxide thickness of ∼750 nm.

was observed, and the $^{28}Si/^{28}SiO_2$ interface was different. In Figs. 5.13(b) and 5.14(b), the profiles were shifted along the x-axis in order that each $^{nat}SiO_2/^{28}SiO_2$ interface would agree at $x = 0$. Figure 5.13(b) and 5.14(b) indicates that the diffusion length of the sample with the 200-nm-thick $^{28}SiO_2$ layer, the thinnest $^{28}SiO_2$ layer in this work, was longer than that of other samples. This tendency is consistent with the finding that Si self-diffusivity increases as the distance between the Si/SiO_2 interface and the $^{nat}SiO_2/^{28}SiO_2$ interface decreases [15, 16]. As mentioned above, these samples have the same total oxide thickness; therefore, Si self-diffusivity in SiO_2 does not depend on the oxide thickness but on the distance between the diffusers and the Si/SiO_2 interface, as mentioned in chapter 5 and refs. 15 and 16.

The mechanism of the dependence of Si self-diffusion is interpreted as follows [16]. SiO molecules are generated at the interface via $Si + SiO_2 \rightarrow 2SiO$[60, 71] and diffuse into oxides, which has been predicted by various studies [3, 50, 52, 60, 71]. SiO diffusion is not such that the concentration of SiO molecules becomes uniform in the 200-nm-thick oxide but is much faster than Si self-diffusion [16, 53, 60]. Therefore, the diffusion of Si atoms via SiO is faster than the thermal Si self-diffusion where Si atoms do not diffuse via SiO, and

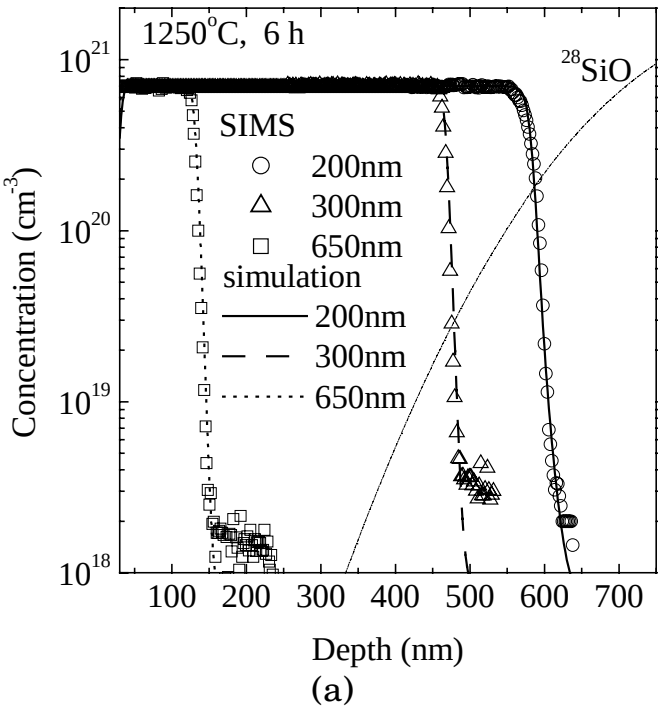

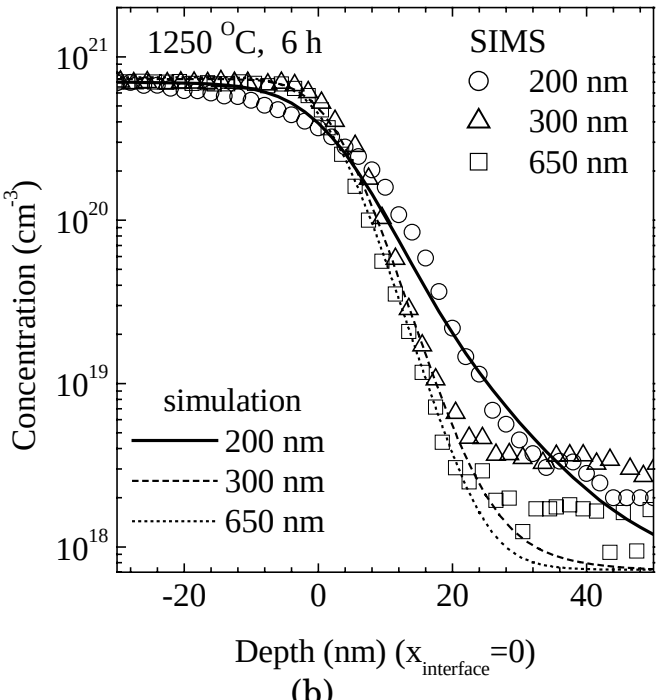

Figure 5.13: SIMS results for the isotope hetero-structures with a constant total oxide thickness after annealing at 1250°C for 6 h. (a) raw profiles are (b) shifted along x-axis so that each interface between $^{nat}SiO_2$ and $^{28}SiO_2$ agrees at $x = 0$. Open circles, open triangles, and open squares represent the SIMS depth profiles of the samples with 200-, 300-, and 650-nm-thick $^{28}SiO_2$ layers. The chain line is the profile of ^{28}SiO molecules obtained by the simulation. The rest of the lines are simulated ^{30}Si profiles for each structure.

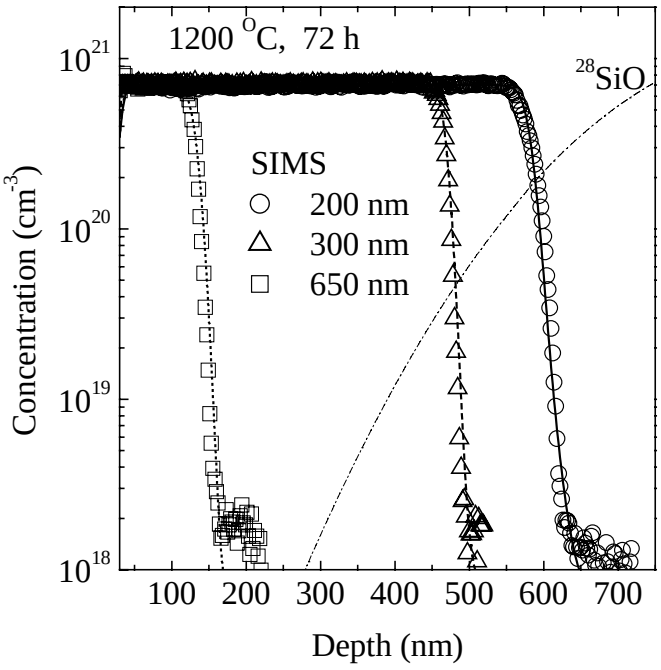

Figure 5.14: SIMS results for the isotope hetero-structures with a constant total oxide thickness after annealing at 1200°C for 72 h. (a) raw profiles are (b) shifted along x-axis so that each interface between $^{nat}SiO_2$ and $^{28}SiO_2$ agrees at $x = 0$. Open circles, open triangles, and open squares represent the SIMS depth profiles of the samples with 200-, 300-, and 650-nm-thick $^{28}SiO_2$ layers. The chain line is the profile of ^{28}SiO molecules obtained by the simulation. The rest of the lines are simulated ^{30}Si profiles for each structure.

the higher the SiO concentration, the faster the diffusion of Si atoms. The concentration of SiO decreases with the distance from the interface at which SiO molecules are generated. As a result, Si self-diffusion is enhanced near the interface, where the concentration of SiO molecules is high.

An analysis of Si self-diffusion was conducted in a manner similar to that in § 5.2. The diffusion equations for ^{30}Si, ^{30}SiO, and ^{28}SiO were solved numerically [16]. In the simulation, the effect of SiO molecules were taken into account as eq. (5.2). Equation (5.2) indicates that Si atoms substituted into Si sites of SiO_2 diffuse via the kick-out mechanism, reacting with diffusing SiO molecules in interstitial sites. In addition, Si atoms diffuse via a mechanism which does not involve SiO. The Si self-diffusivity is therefore described by

$$D_{\mathrm{Si}}^{\mathrm{SD}} = D_{\mathrm{Si\,(th)}}^{\mathrm{SD}} + D_{\mathrm{SiO}}^{\mathrm{SD}} C_{^{28}\mathrm{SiO}} / C_{\mathrm{SiO}}^{\circ}, \tag{5.11}$$

where C_{SiO}° is the maximum concentration of SiO in SiO_2 and is described as $C_{\mathrm{SiO}}^{\circ} = 3.6\times10^{24}\exp(-1.07\,\mathrm{eV/kT})$. [16]. $D_{\mathrm{SiO}}^{\mathrm{SD}} = D_{\mathrm{SiO}} C_{\mathrm{SiO}}^{\circ} / N_o$ is the self-diffusivity of silicon via SiO molecules, where N_o denotes the number of SiO_2 molecules in a unit volume of SiO_2. $D_{\mathrm{Si\,(th)}}^{\mathrm{SD}}$ is the Si self-diffusivity via the mechanism which does not involve SiO molecules, and $D_{\mathrm{Si\,(th)}}^{\mathrm{SD}} = 0.8\exp(-5.2\ \mathrm{eV/kT})\ \mathrm{cm^2/s}$ [9, 10] was used in the present study. The boundary condition for ^{28}SiO(int) at the ^{28}Si/$^{28}SiO_2$ interface is given by $C_{^{28}\mathrm{SiO}} = C_{\mathrm{SiO}}^{\circ}$ to describe the generation of SiO at the interface. The amount of ^{30}SiO(int) arriving at the ^{28}Si/$^{28}SiO_2$ interface is so small that the mixing of ^{28}Si with ^{30}Si at the interface can be neglected. The boundary condition at the nitride-capped surface is represented by a zero-flux condition because the caps act as barriers. It is reasonable to assume that reaction (5.2) is so fast that the local equilibrium of the reaction is established, and hence, the rate constants are set to be sufficiently large. The only parameter obtained from the simulation to fit the experimental profiles of ^{30}Si is D_{SiO}. In addition, in our calculation, the broadening of SIMS profiles caused by surface roughness and mixing by SIMS sputtering was taken into account using the method developed by Hoffman [58].

The method was developed starting with a simple model for the mixing influence and extending it to include surface roughness and information depth, i.e., a model from mixing, roughness, and information depth [58, 59]. Therefore, the model is called MRI model. MRI model is explained in detail in Appendix B

Simulated results show good agreement with the experimental profiles, as shown in Figs. 5.13 and 5.14. Therefore, the dependence of Si self-diffusion in the isotope heterostructures on the distance can be explained by taking into account SiO molecules.

The diffusivity of SiO (D_{SiO}) obtained in the present work agrees with $D_{\mathrm{SiO}} = 3.4{\times}10^2$ $\exp(-5.2\,\mathrm{eV/kT})$ cm^2/s of ref. 16, as shown in Fig 5.15. Si self-diffusion in the isotope heterostructures and in the ^{30}Si-implanted $^{28}SiO_2$ layers can be simulated by using the same values of D_{SiO}. The samples used in the present work had almost the same total oxide thickness; the only difference among the samples was the distance from the $^{28}Si/^{28}SiO_2$ interface. Therefore, the distance has a significant effect on Si self-diffusion, as mentioned [15, 16]. Experimentally, we have confirmed that Si self-diffusion in SiO_2 does not depend on the total oxide thickness but on the distance between ^{30}Si diffusers and the Si/SiO_2 interface.

The calculated profiles of ^{28}SiO are also shown in Figs. 5.13(a) and 5.14(a). After the annealing at 1200°C for 72 h, the concentration of SiO molecules arriving from the Si/SiO_2 interface was $\sim 10^{20}$ cm^{-3} at the $^{\mathrm{nat}}SiO_2/^{28}SiO_2$ interface of the sample with the 200-nm-thick $^{28}SiO_2$ layer. As a result, Si self-diffusion was enhanced by the high concentration of SiO molecules. For the sample with the 650-nm-thick $^{28}SiO_2$ layer, few SiO molecules arrived at the $^{\mathrm{nat}}SiO_2/^{28}SiO_2$ interface. Since enhancement of Si self-diffusion by SiO molecules is negligible, the analysis assuming a constant Si self-diffusivity is valid for the samples. The diffusivity obtained for the samples agrees with the $D_{\mathrm{Si}}^{\mathrm{SD}} = 0.8\,\exp(-5.2\,\mathrm{eV/kT})$ cm^2/s of eq. (4.2) as shown in Fig. 5.15. The results were obtained with the SiN layer, which acts as barrier to oxygen diffusion, and the diffusivity agrees with the value of Si self-diffusivity reported in refs. 9 and 10. Therefore, the oxygen in an ambient does not have an influence on Si self-diffusion in SiO_2, as mentioned above.

As we argued in chapter 5, it is confirmed here that there is no effect of the stress between the SiN layer and SiO_2 on Si self-diffusion since the same value of $D_{\mathrm{SiO}}^{\mathrm{SD}}$ can be used for the simulation of all the samples with various distances between the SiN/SiO_2 interface and the $^{\mathrm{nat}}SiO_2/^{28}SiO_2$ interface.

5.4 Si self-diffusion in SiO_2 under CVD grown SiN capping layers

The effect of the distance of Si diffusers from the Si/SiO_2 interface on Si self-diffusion in SiO_2 gives the answer to the origin of the difference between ours and Mathiot's [13]. However, the values of Mathiot *et al.*[13] were twice as high as ours. There still exists the difference in the experimental condition which is the method of SiN capping. We employed

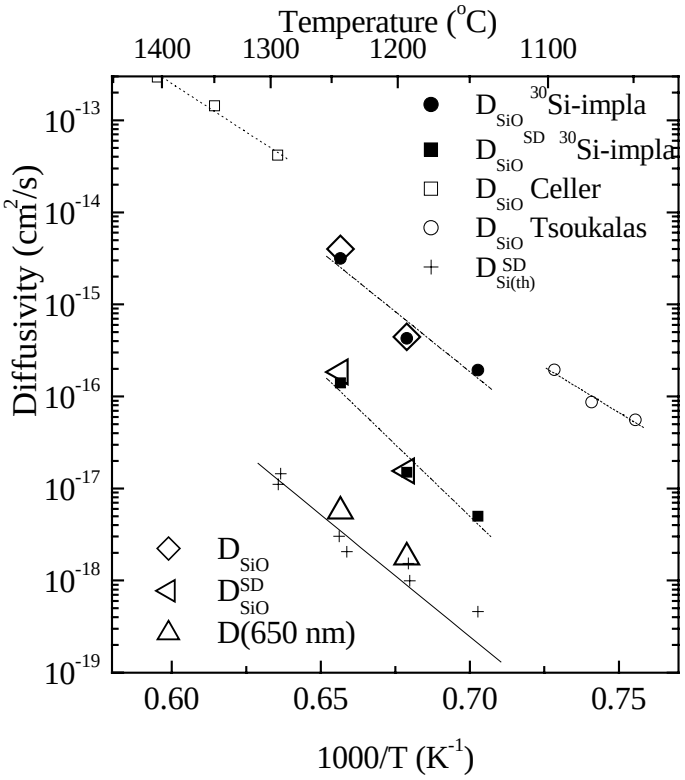

Figure 5.15: Temperature dependencies of the Si diffusion coefficients obtained in this study with those reported previously in the literature. $\diamond$, $\triangleleft$, and $\triangle$ are the present results for D_{SiO}, D^{SD}_{SiO}, and D^{SD}_{Si} obtained with $^{28}SiO_2$ of 650 nm thickness, respectively. Filled circles ($\bullet$) and filled squares ($\blacksquare$) represent the results obtained with ^{30}Si-implanted samples for D_{SiO} and D^{SD}_{SiO}, respectively. $D^{SD}_{Si(th)}$ obtained in chapter 4 are also plotted as (+). The previously reported values are the SiO diffusivities from refs. 60 ($\square$) and 53 ($\circ$) (thermally migrated impurities and defect evolutions as markers, respectively).

sputtering while Mathiot *et al*. used CVD to deposit SiN layers on SiO_2 [13]. This section investigates an influence of the SiN capping method on Si self-diffusion in SiO_2.

5.4.1 Experiment

The $^{nat}SiO_2/^{28}SiO_2$ isotope heterostructures were fabricated in a manner similar to

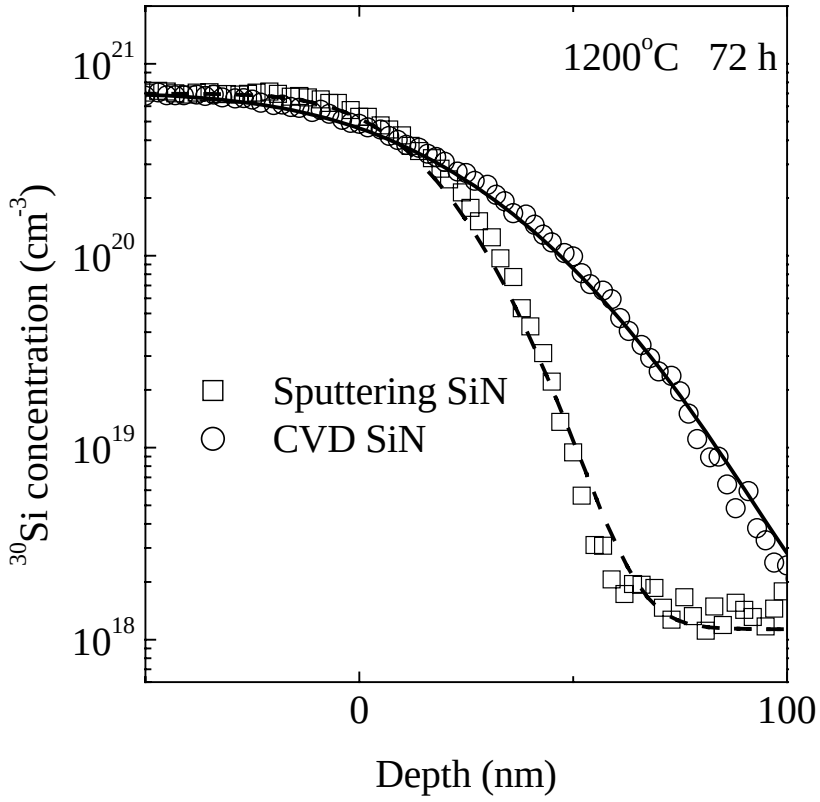

Figure 5.16: SIMS results of ^{30}Si in a sample with a sputtered SiN layer (□) and a CVD grown SiN layer (◯) after annealing at 1200 °C for 72 h. Curves are calculated profiles of ^{30}Si assuming a constant diffusivity.

that described in §2.1.3. ^{28}Si epilayers were thermally oxidized in dry O_2 to form $^{28}SiO_2$ of 200-nm thickness, and $^{nat}SiO_2$ of 550-nm thickness was deposited on the surfaces of $^{28}SiO_2$, by LPCVD. Finally, a 30-nm-thick silicon nitride layer was deposited on top of the samples by means of rf magnetron sputtering or CVD, as shown in Fig. 5.12(a). Both samples were cut into 5×5 mm^2 pieces and were annealed at 1200 and 1250°C. The diffusion profiles were obtained by SIMS using the same condition as mentioned above. The surface roughness of each sample before and after annealing was measured by AFM.

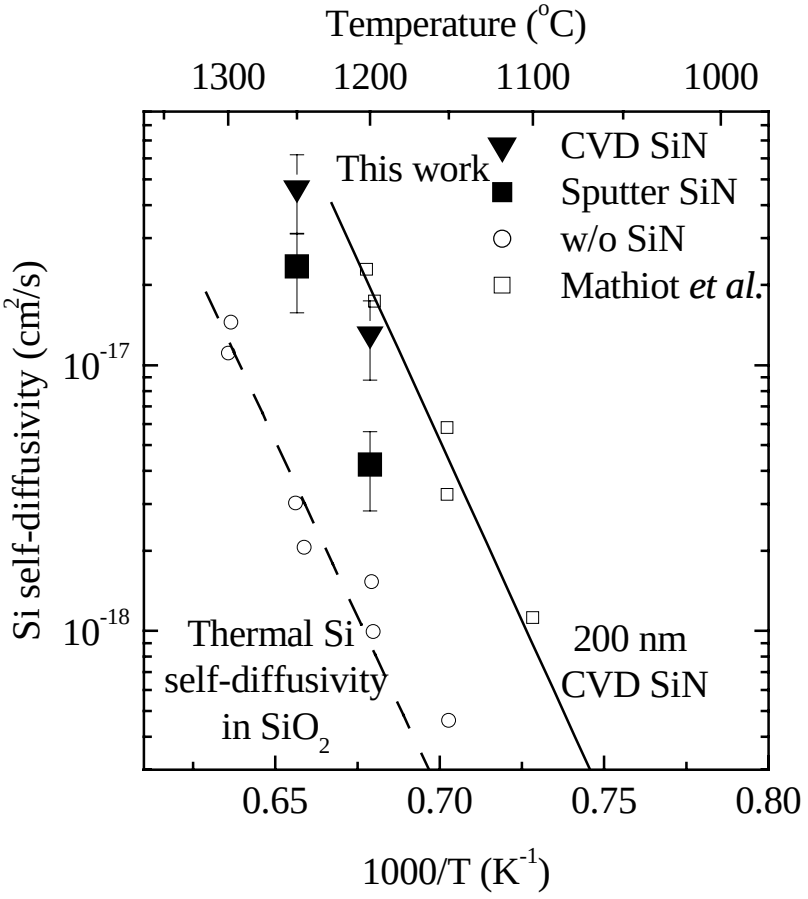

Figure 5.17: Si self-diffusivity in $^{28}SiO_2$ capped with a sputtered SiN (filled squares) layer and a CVD grown SiN layer (filled triangles).

5.4.2 Results and discussions

SIMS profiles obtained for the sputtered SiN layer capped sample and CVD SiN layer capped sample after annealing at 1200°C for 72 h are shown in Fig.5.16. In the same figure, simulated ^{30}Si profiles obtained assuming a constant diffusivity for each sample are plotted. Figure 5.16 indicated clearly that Si self-diffusion in the samples capped with the CVD SiN layer is faster than that in the samples capped with the sputtered SiN layer.

The Si self-diffusivity obtained from fitting by eq. (4.1) to the SIMS profiles of ^{30}Si in both the samples are shown in Fig. 5.17. The error bars, which was estimated from the accuracy of measurement of the SIMS crater, are also shown.

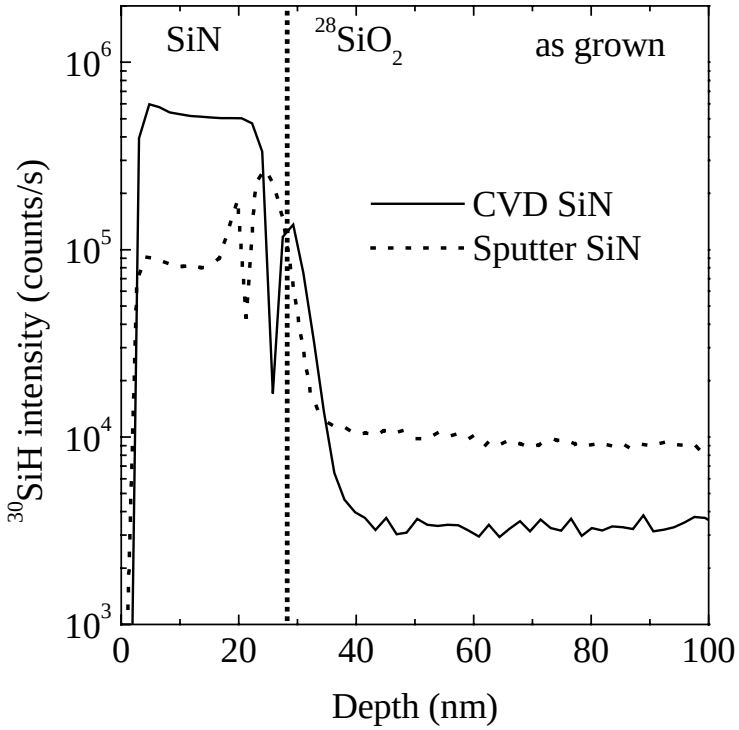

Figure 5.18: SIMS results of ^{30}SiH in a sample with a sputtered SiN layer and a CVD grown SiN layer.

The Si self-diffusivity in the samples with the CVD grown SiN was higher than that in the samples with the SiN deposited by sputtering. In addition, the Si self-diffusivity of the samples with CVD grown SiN agreed with that reported by Mathiot *et al.* using 200-nm thick $^{28}SiO_2$ capped with a CVD grown SiN layer.

Let us now discuss why the Si self-diffusivity in the SiO_2 with a SiN cap grown by CVD is higher than that in the SiO_2 with a SiN cap deposited by sputtering. It has been reported that boron diffusion through the thin gate oxide is enhanced by hydrogen from a SiN layer. The concentration of hydrogen depends on the method growing the SiN layer [79].

We investigated the concentration of hydrogen in both sets of samples before diffusion annealing using SIMS. We obtained profiles of ^{30}SiH in both the samples in order to compare the hydrogen concentration. Secondary ion intensities of ^{30}SiH in each sample were plotted in Fig. 5.18. As the figure shows, the concentration of hydrogen in the

CVD grown SiN layer was higher than that in the SiN layer grown by sputtering. In the subsequent diffusion annealing, more hydrogen from SiN is introduced into SiO_2 for the case of CVD SiN than sputtered SiN, and enhance Si self-diffusion in SiO_2. Tanaka *et al.* reported that hydrogen forming SiH in SiN decomposes at high temperature and diffuses into the oxide to enhance boron diffusion in the oxide [79].

Chapter 6

Boron diffusion in SiO_2

6.1 Introduction

We showed that SiO molecules are generated at the Si/SiO_2 interface. This chapter discusses whether SiO molecules have an influence on boron diffusion since the penetration of boron through SiO_2 is the most important issue in application.

In this section, we have investigated the effect of the Si/SiO_2 interface on B diffusion using the B implanted samples shown in Fig. 6.1. Originally, we have co-implanted ^{30}Si with B in order to investigate the effect of B diffusion on Si self-diffusion in SiO_2. However, we have found recently that Si self-diffusion is affected by B of concentration larger than 10^{20} cm^{-3} [26]. Therefore, we employed ^{30}Si with implanted B of concentration less than

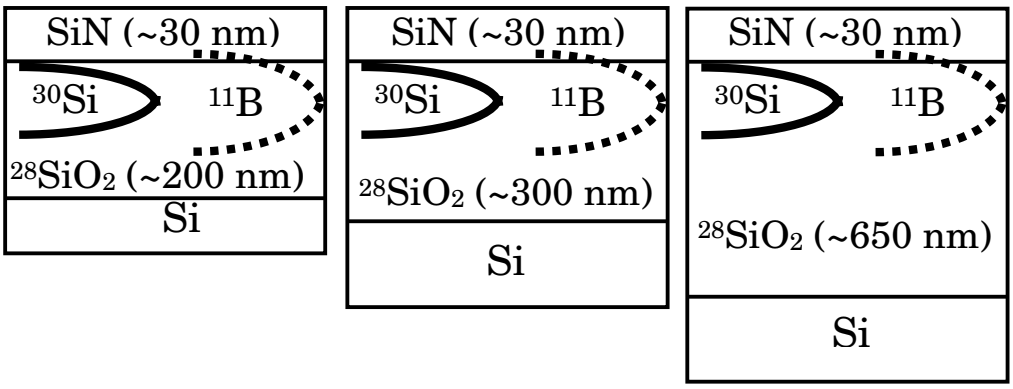

Figure 6.1: Sample structures of ^{30}Si- and B-implanted $^{28}SiO_2$ layers.

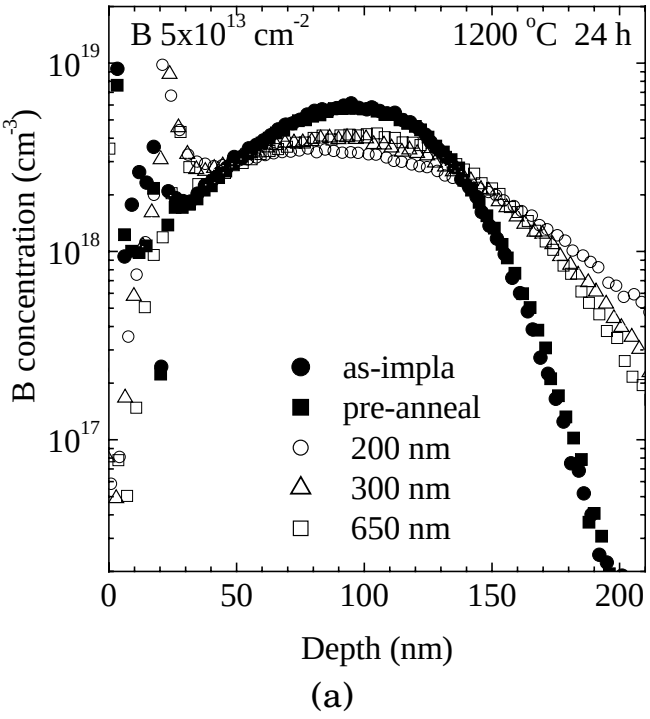

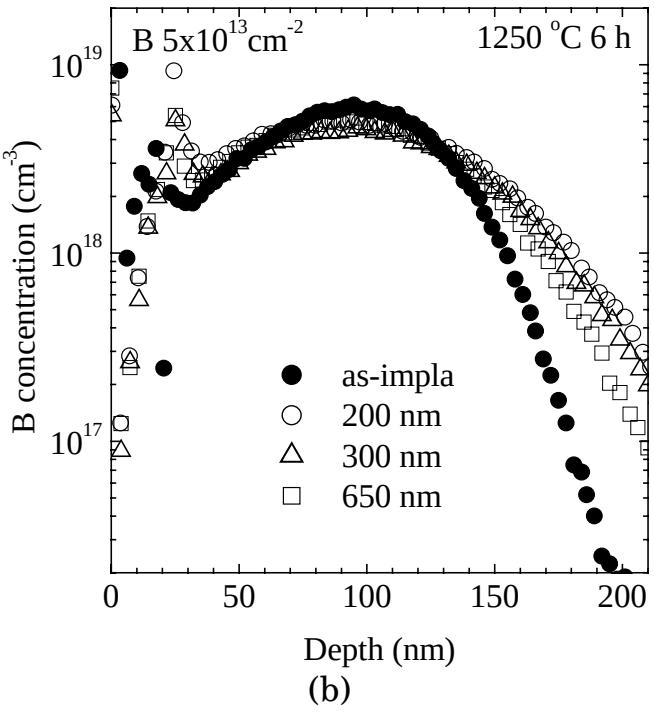

Figure 6.2: SIMS profiles of before and after annealing:(a) at 1200°C for 24 h and (b) at 1250°C for 6 h in the 200 nm thick sample (○), 300 nm thick sample (△), and 650 nm thick sample (□). The profiles of boron before annealing and after preannealing at 1000 °C for 30 min are plotted as (●) and (■), respectively.

10^{19} cm^{-3} to ensure the accuracy of our experiments.

6.2 Experiment

The boron-implanted samples were fabricated in a manner as described in § 2.1.4. These samples were cut into 5×5 mm^2 pieces and were pre-annealed at 1000°C for 30 min to eliminate implantation damages, and annealed at various temperatures in the range of 1150-1250°C. The profiles of B and Si were obtained by SIMS, and the depth of SIMS craters were measured by a profilometer. The surface roughness of each sample before and after annealing was measured by AFM.

6.3 Results and discussions

Figures 6.2(a) and (b) shows the depth profiles of ^{11}B before and after annealing at 1200°C for 24 h and 1250°C for 6 h, respectively. The profiles after the pre-annealing agree with the as-implanted profiles within the experimental error of our SIMS measurements.

The profiles of ^{11}B became broader with decreasing $^{28}SiO_2$ layer thickness, i.e., B diffusivity increased with decreasing distance from the Si/SiO_2 interface, as shown in Fig. 6.2. The dependence of B diffusion in SiO_2 on the distance from the Si/SiO_2 interface is similar to that of Si self-diffusion in SiO_2 (chapter 5). As mentioned above, Si self-diffusion is enhanced by SiO molecules generated at the interface and diffusing into the oxide. The shorter the distance between implanted B and the interface becomes, the broader the B diffusion profiles become. In order to confirm whether the origin of the B diffusion enhancement is due to SiO molecules, we have constructed the model of B diffusion taking into account SiO molecules, and compared the results of the simulation to experiments.

In the present work, ^{30}Si diffusion profiles in the B-implanted $^{28}SiO_2$ layers agreed fairly with that of the $^{28}SiO_2$ layers without B implantation [15], as shown in Fig. 6.3. Implanted B and B diffusion do not have an influence on Si self-diffusion at the concentration employed in the present work since the B concentration was lower than 10^{20} cm^{-3} [26].

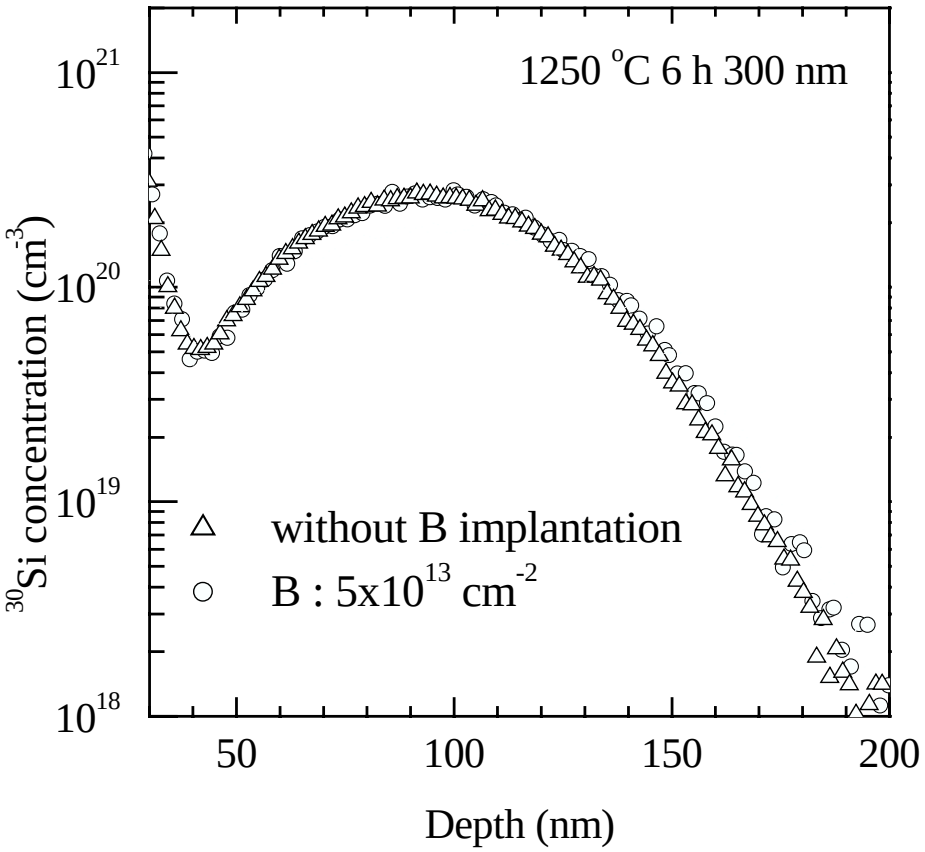

Figure 6.3: The depth profiles of ^{30}Si in the 300 nm thick samples with and without boron implantation after annealing at 1250° for 6 h.

6.4 Boron diffusion model

A boron diffusion model was proposed as a natural extension of a previously proposed model of Si self-diffusion described in § 5.2. The results in Fig. 6.2 indicate that B diffuses via a mechanism that involves SiO in addition to one that does not involve SiO. An evidence for the existence of two mechanisms is that very few SiO molecules arrived from the interface in the 650-nm-thick samples. B diffusion via SiO can be described as

$$\mathrm{B(sub) + SiO(int) \Leftrightarrow Si(sub) + BO(int),} \tag{6.1}$$

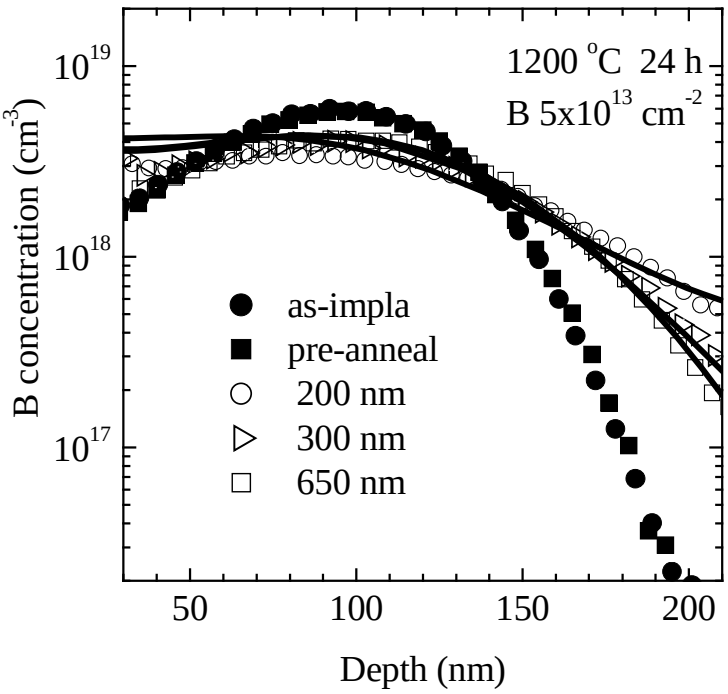

Figure 6.4: SIMS profiles of before (•) and after annealing at 1200°C for 24 h in the 200 nm thick sample (○), 300 nm thick sample (△), and 650 nm thick sample (□).

in a similar manner to B diffusion in Si via the kick-out mechanism, where BO(int) may be a complex of Si-B-O [21]. In eq. (6.1), interstitial SiO molecule (SiO(int)) pushes substitutional B atom (B(sub)) and into BO(int). In addition, boron diffusion which does not involve SiO molecules, Si self-diffusion via SiO molecules, and Si self-diffusion which does not involve SiO molecules are described by

$$\mathrm{B(sub)} + \mathrm{B'(sub)} \Leftrightarrow \mathrm{B'(sub)} + \mathrm{B(sub)}, \tag{6.2}$$

$$^{30}\mathrm{Si(sub)} + {}^{28}\mathrm{SiO(int)} \Leftrightarrow {}^{28}\mathrm{Si(sub)} + {}^{30}\mathrm{SiO(int)}, \tag{6.3}$$

$$^{30}\mathrm{Si(sub)} + {}^{28}\mathrm{Si(sub)} \Leftrightarrow {}^{28}\mathrm{Si(sub)} + {}^{30}\mathrm{Si(sub)}. \tag{6.4}$$

In eq. (6.3), substitutional Si atom (Si(sub)) diffuses via kick-out reaction with diffusing SiO molecules (SiO(int)). Equations (6.2) and (6.4) represent B and Si diffusion which do not involve SiO molecules. The SiO concentration is high near the interface during annealing. Therefore, the large contribution of relatively rapid B diffusion via SiO leads to higher total B diffusivity.

From the model, the diffusion equations were constructed. The diffusion equations are described by

$$\frac{\partial C_{\mathrm{B_s}}}{\partial t} = \frac{\partial}{\partial x}\Big(D^{\mathrm{eff}}_{B\ (\mathrm{th})}\frac{\partial C_{\mathrm{B_s}}}{\partial x}\Big) - R_1, \tag{6.5}$$

$$\frac{\partial C_{\mathrm{B_i}}}{\partial t} = \frac{\partial}{\partial x}\Big(D_{\mathrm{B_i}}\frac{\partial C_{\mathrm{B_i}}}{\partial x}\Big) + R_1, \tag{6.6}$$

$$\frac{\partial C_{^{30}\mathrm{Si}}}{\partial t} = \frac{\partial}{\partial x}\Big(D^{\mathrm{SD}}_{\mathrm{Si}\ (\mathrm{th})}\frac{\partial C_{^{30}\mathrm{Si}}}{\partial x}\Big) - R_2, \tag{6.7}$$

$$\frac{\partial C_{^{30}\mathrm{SiO}}}{\partial t} = \frac{\partial}{\partial x}\Big(D_{\mathrm{SiO}}\frac{\partial C_{^{30}\mathrm{SiO}}}{\partial x}\Big) + R_2, \tag{6.8}$$

$$\frac{\partial C_{^{28}\mathrm{SiO}}}{\partial t} = \frac{\partial}{\partial x}\Big(D_{\mathrm{SiO}}\frac{\partial C_{^{28}\mathrm{SiO}}}{\partial x}\Big) - R_1 - R_2, \tag{6.9}$$

where R_1 and R_2 are the Reaction terms and are described by

$$R_1 = k_{f_1} C_{\mathrm{B_s}} C_{^{28}\mathrm{SiO}} - k_{b_1} C_{\mathrm{B_i}}, \tag{6.10}$$

$$R_2 = k_{f_2} C_{^{30}\mathrm{Si}} C_{^{28}\mathrm{SiO}} - k_{b_2} C_{^{30}\mathrm{SiO}}. \tag{6.11}$$

In these equations, C_x is the concentration of the corresponding species in eqs. (6.1)-(6.4). $D^{\mathrm{eff}}_{B\ (\mathrm{th})}$, $D_{\mathrm{B_i}}$, $D^{\mathrm{SD}}_{\mathrm{Si}\ (\mathrm{th})}$, and D_{SiO} are the effective diffusivity of B, which does not involve SiO, the diffusvity of B(int), Si self-diffusivity under thermal equilibrium, and the diffusivity of SiO, respectively. k_f and k_b are the forward and backward rate constants of eqs. (6.1) and (6.3). In the same manner as described in § 5.2, reactions (6.1)-(6.4) are assumed to be so fast that the local equilibrium of the reaction is established, and hence the rate constants (k_{f_1}, k_{b_1}, k_{f_2}, and k_{b_2}) are set to be large enough. $D^{\mathrm{eff}}_{B\ (\mathrm{th})} = 3.12 \times 10^{-3} \exp(-3.93\mathrm{eV/kT})\ \mathrm{cm^2/s}$ obtained experimentally [80] was used

in this simulation. $D^{\mathrm{SD}}_{\mathrm{Si\,(th)}} = 0.8\ \exp(-5.2\mathrm{eV/kT})\ \mathrm{cm}^2/\mathrm{s}$ obtained in chapter 4 and $D_{\mathrm{SiO}} = 3.4\exp(-5.2\mathrm{eV/kT})\ \mathrm{cm}^2/\mathrm{s}$ obtained in chapter 5 were employed in this simulation. The boundary condition at the $\mathrm{SiN/SiO_2}$ interface was a zero-flux condition since the SiN cappings acted as barriers. The boundary condition for $^{28}\mathrm{SiO(int)}$ at the $^{28}\mathrm{SiO_2}/^{28}\mathrm{Si}$ interface was given by $C_{^{28}\mathrm{SiO(x=interface)}} = C^{\circ}_{\mathrm{SiO}}$.

These diffusion equations were numerically solved by the partial differential equation solver ZOMBIE [81], and simulated profiles of $^{11}\mathrm{B}$ were compared with these experimental profiles.

Taking into account the two mechanisms, the total effective B diffusivity is described by

$$D^{\mathrm{eff}}_{\mathrm{B}} = D^{\mathrm{eff}}_{\mathrm{B\,(th)}} + D^{\mathrm{eff}}_{i}\frac{C_{\mathrm{SiO}}}{C^{\circ}_{\mathrm{SiO}}}, \tag{6.12}$$

where $D^{\mathrm{eff}}_{\mathrm{B\,(th)}}$ and $D^{\mathrm{eff}}_{\mathrm{i}}$ are the effective diffusivity of thermal B diffusion and the effective diffusivity of B diffusion via the mechanism that involves SiO molecules. $D^{\mathrm{SD}}_{\mathrm{SiO}} = 4 \times 10^4 \exp(-6.2\ eV/kT)\ \mathrm{cm}^2/\mathrm{s}$[16] was applied in this simulation. As a result, the only parameter to be obtained by fitting is $D^{\mathrm{eff}}_{\mathrm{i}}$.

Figure 6.4 shows that the simulation results for the all $^{28}\mathrm{SiO_2}$ thicknesses agree with the experimental results. Therefore, the dependence of B diffusion on the distance from the $\mathrm{Si/SiO_2}$ interface can be explained by taking into account SiO molecules. However, the experimentally obtained B profiles near the $\mathrm{SiN/SiO_2}$ interface in $\mathrm{SiO_2}$ do not agree perfectly with the simulated profiles. This may be due to boron segregation at the $\mathrm{SiN}/^{28}\mathrm{SiO_2}$ interface as reported previously [82].

Chapter 7

Conclusions and future works

7.1 Conclusions

We have performed experimental investigations of Si and B diffusions in thermal SiO_2 formed on Si wafers followed by complete numerical modeling of the data. The following conclusions have been derived from the results and analyses.

We have determined precisely the Si self-diffusivity in SiO_2 without surface silicon nitride layers and shown further that it does not depend on the partial pressure of oxygen in the annealing ambient. Si self-diffusivity obtained without surface nitride does not depend on the thickness of the SiO_2 film and agrees with the previously reported values of Si self-diffusivity in the bulk quartz and the vitreous silica.

This situation was found to change dramatically when surface silicon nitride (SiN) layers are placed on top of SiO_2. We have investigated the effect of the Si/SiO_2 interface on Si self-diffusion in SiO_2 with SiN layers using ^{30}Si-implanted $^{28}SiO_2$ and isotope heterostructures with a constant total oxide thickness. With the SiN layer, Si self-diffusivity increased with the decreasing distance between ^{30}Si diffusers and the Si/SiO_2 interface. In other words, Si self-diffusion was enhanced near the interface. In order to understand this phenomenon quantitatively, we proposed a new picture in which SiO molecules generated at the Si/SiO_2 interface, due to $SiO_2+Si \rightarrow 2SiO$ reaction, diffuse into the SiO_2 layer and enhance the Si self-diffusivity. Numerical simulations conducted based on this model for our variety of experimental conditions yield very good quantitative agreement with the experimental results. These experimental and simulated results clearly show that SiO molecules are generated at the Si/SiO_2 interface and diffuse into the oxide.

Next, we have investigated the influence of the deposition method of the nitride layers on the Si self-diffusion in SiO_2. The Si self-diffusivity in SiO_2 with the CVD grown SiN layer was higher than that with the sputtered SiN layer. The effect of the SiO molecules generated at the Si/SiO_2 interface and the dependence on the SiN deposition method explain together previously published experimental values of Si self-diffusivity in SiO_2, which appeared to disagree with one another.

Moreover, we have shown that B diffusion in SiO_2 is also enhanced by SiO when SiN surface layers are placed. By taking into account SiO molecules, a simulation was performed for Si and B diffusion, and the results showed good agreement with the experimental profiles. Therefore, both B and Si diffusions are enhanced by the SiO molecules generated at the interface and diffusing into SiO_2. SiO diffusion is faster than Si self-diffusion in SiO_2, but is not fast enough for the SiO concentration to reach constant throughout the SiO_2 layer. Since the concentration of SiO molecules is higher near the interface, the enhancement of Si self-diffusion and B diffusion in SiO_2 is larger near the interface.

7.2 Future works

In the future, behavior of silicon in high-k gate dielectrics should be investigated in a similar manner described in this work. It is known that poly-Si/high-k insulator/SiO_2/Si systems degrade due to silicidation during postdeposition annealing (PDA). This degradation is suspected to cause by Si outdiffusing from the either thin interfacial SiO_2 layer or Si substrate [83]. Understanding of Si behavior during PDA can be achieved using silicon isotopes as performed in this study.

In order to understand the behavior of the SiO molecules generated at the Si/SiO_2 interface further, oxygen diffusion in SiO_2 using ^{18}O should be conducted. For this investigation, $^{28}Si^{18}O_2/^{nat}Si^{nat}O_2$ isotope heterostructures can be fabricated as follows. The ^{28}Si epilayer of ~30 nm thickness will be grown on Si substrate, followed by thermal oxidation in dry $^{18}O_2$ to form $^{28}Si^{18}O_2/^{nat}Si$ of ~60 nm thickness. Subsequent oxidation in $^{nat}O_2$ completes a $^{28}Si^{18}O_2/^{nat}Si^{nat}O_2$ structure.

We have discussed the influence of the method of SiN cappings on Si self-diffusion in chapter 5, and found that the concentration of hydrogen in CVD SiN layers was higher than that in sputtered SiN layers. The problem is difficulty of detecting hydrogen. In order to investigate the effect of hydrogen on Si self-diffusion, we should take advantage

of deuterium instead of hydrogen. Deuterium implanted into the $^{nat}SiO_2/^{28}SiO_2$ isotope heterostructures or into ^{30}Si implanted $^{28}SiO_2$ will allow for simultaneous probing of the ^{30}Si and deuterium concentrations with SIMS.

Appendix A

Numerical method solving diffusion equations

A.1 Finite discrete method

In this work, Crank-Nicolson implicit method was used for the analysis of Si self-diffusion in SiO_2. The diffusion equation is described by

$$\frac{\partial u(x,t)}{\partial t} = D\frac{\partial^2 u(x,t)}{\partial x^2}, \tag{A.1}$$

where D is an appropriate diffusion coefficient.

Let the range in x be divided into equal intervals Δx and the time into intervals Δt, as shown in Fig. A.1. Let the coordinates of a representative grid point $(x,\ t)$ be $(i\Delta x,\ j\Delta t)$, where i and j are integers. The value of concentration u at the point $(i\Delta x,\ j\Delta t)$ is denoted by $u_{i,j}$ with corresponding values at neighboring points labeled as in Fig. A.1. Replacing $\partial^2 u/\partial x^2$ by the mean of its finite-difference representations on the jth and $(j+1)$th time rows we can approximated eq. (A.1) by

$$\frac{u_{i,j+1} - u_{i,j}}{\Delta t} = \frac{D}{2}\left(\frac{u_{i-1,j+1} + u_{i,j+1} + u_{i+1,j+1}}{(\Delta x)^2} + \frac{u_{i-1,j} + u_{i,j} + u_{i+1,j}}{(\Delta x)^2}\right). \tag{A.2}$$

We can write eq. (A.2) in the form

$$-ru_{i-1,j+1} + (2+2r)u_{i,j+1} - ru_{i+1,j+1} = ru_{i-1,j} + (2-2r)u_{i,j} + ru_{i+1,j}, \tag{A.3}$$

where $r = D\frac{\Delta t}{(\Delta x)^2}$.

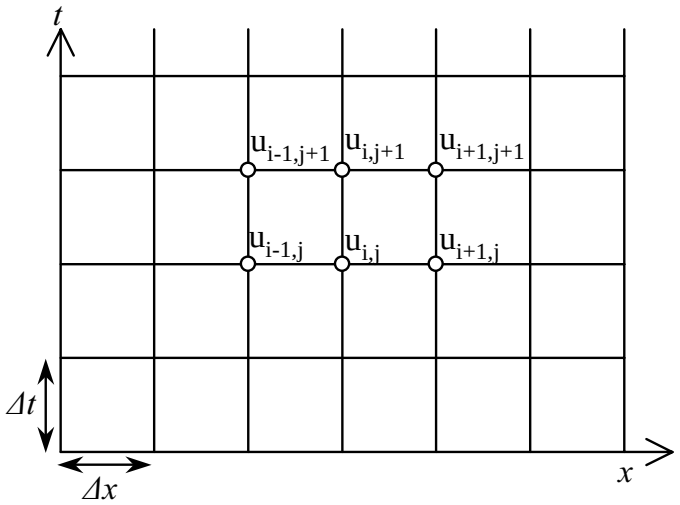

Figure A.1: Time vs. position mesh for calculation of D.

$$
\begin{pmatrix}
-r & 2+2r & -r & & & & \\
 & -r & 2+2r & -r & & & \\
 & & \cdots\cdots & & & & \\
 & & \cdots\cdots & & & & \\
 & & \cdots\cdots & & & & \\
 & & & & -r & 2+2r & -r \\
 & & & & & -r & 2+2r & -r
\end{pmatrix}
\begin{pmatrix} u_{1,j+1} \\ \cdots \\ u_{i-1,j+1} \\ u_{i,j+1} \\ u_{i+1,j+1} \\ \cdots \\ u_{n,j+1} \end{pmatrix}
$$

$$
= \begin{pmatrix}
r & 2-2r & r & & & & \\
 & r & 2-2r & r & & & \\
 & & \cdots\cdots & & & & \\
 & & \cdots\cdots & & & & \\
 & & \cdots\cdots & & & & \\
 & & & & r & 2-2r & r \\
 & & & & & r & 2-2r & r
\end{pmatrix}
\begin{pmatrix} u_{1,j} \\ \cdots \\ u_{i-1,j} \\ u_{i,j} \\ u_{i+1,j} \\ \cdots \\ u_{n,j} \end{pmatrix} \tag{A.4}
$$

The boundary condition is as follows. At $x = 0$, which is the interface between SiN

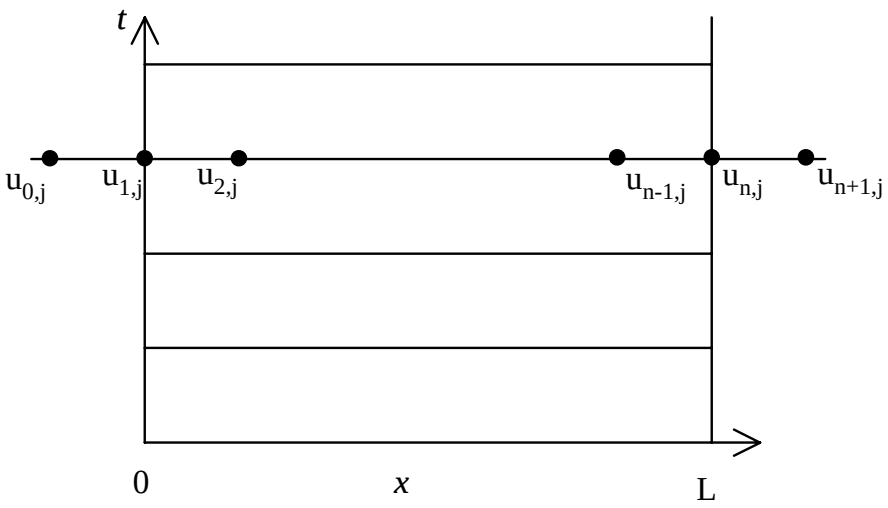

Figure A.2: Derivation of derivative boundary conditions. Fictitious concentration $u_{0,j}$ and $u_{n+1,j}$ are at the external grid points $(-\Delta x, j\Delta t)$ and $(n\Delta x, j\Delta t)$, respectively.

and $^{28}SiO_2$, no-flow boundary condition (see next section) is described by

$$\left.\frac{\partial u(x,t)}{\partial x}\right|_{x=0} = 0, \tag{A.5}$$

Introducing a fictitious concentration $u_{0,j}$ at the external grid points $(-\Delta x, j\Delta t)$ (Fig. A.2), we can obtain a relatively accurate replacement of eq. (A.5).

$$\frac{u_{2,j} - u_{0,j}}{2\Delta x} = 0. \tag{A.6}$$

Substituting $i = 1$ into eq. (A.3), we can obtain

$$-ru_{0,j+1} + (2 + 2r)u_{1,j+1} - ru_{2,j+1} = ru_{0,j} + (2 - 2r)u_{1,j} + ru_{2,j}. \tag{A.7}$$

Elimination of $u_{0,j}$ from eqs. (A.6) and (A.7) gives

$$(2 + 2r)u_{1,j+1} - 2ru_{2,j+1} = (2 - 2r)ru_{1,j} + 2ru_{2,j}. \tag{A.8}$$

At $x = L$, using similar manner that for the boundary at $x = 0$, we can obtain the no-flow boundary condition described by

$$\left.\frac{\partial u(x,t)}{\partial x}\right|_{x=L} = 0. \tag{A.9}$$

This equation can be approximated by

$$\frac{u_{n+1,j} - u_{n-1,j}}{2\Delta x} = 0. \tag{A.10}$$

Substituting $i = n$ into eq. (A.3), we can obtain

$$-ru_{n-1,j+1} + (2+2r)u_{n,j+1} - ru_{n+1,j+1} = ru_{n-1,j} + (2-2r)u_{n,j} + ru_{n+1,j} \tag{A.11}$$

Elimination of $u_{0,j}$ from eqs. (A.10) and (A.11) gives

$$-2ru_{n-1,j+1} + (2+2r)u_{n,j+1} = 2ru_{n-1,j} + (2-2r)u_{n,j} \tag{A.12}$$

Finally the simultaneous equations to be solved were described by

$$\begin{pmatrix} 2+2r & -2r & & & & & & \\ -r & 2+2r & -r & & & & & \\ & -r & 2+2r & -r & & & & \\ & \cdots & \cdots & \cdots & & & & \\ & \cdots & \cdots & \cdots & & & & \\ & & & -r & 2+2r & -r & & \\ & & & & -r & 2+2r & -r & \\ & & & & & -2r & 2+2r \end{pmatrix} \begin{pmatrix} u_{1,j+1} \\ u_{2,j+1} \\ \cdots \\ u_{i,j+1} \\ \cdots \\ u_{n-1,j+1} \\ u_{n,j+1} \end{pmatrix}$$

$$= \begin{pmatrix} 2-2r & 2r & & & & & & \\ r & 2-2r & r & & & & & \\ & r & 2-2r & r & & & & \\ & \cdots & \cdots & \cdots & & & & \\ & \cdots & \cdots & \cdots & & & & \\ & & & r & 2-2r & r & & \\ & & & & r & 2-2r & r & \\ & & & & & 2r & 2-2r \end{pmatrix} \begin{pmatrix} u_{1,j} \\ u_{2,j} \\ \cdots \\ u_{i,j} \\ \cdots \\ u_{n-1,j} \\ u_{n,j} \end{pmatrix} \tag{A.13}$$

A.1.1 Boundary condition

Impervious diffusion boundaries are equivalent to adiabatic walls in heat transfer. Diffusion species approaching the leftmost boundary must also be reflected in the opposite direction. Since SiN layers act as barriers, no-flow boundary condition was applied for the boundary condition at the interface between a SiN layer and SiO_2 layer.

Fick's first law can be invoked to show that the mirrorlike reflection of diffusion species reaching such a boundary is equivalent to $J_{\text{boundary}} = 0$. Therefore, the no-flow boundary condition is represented by a gradient at that plane, i.e.,

$$\frac{\partial u(x,t)}{\partial x} = 0 = -\frac{J_{\text{boundary}}}{D}. \tag{A.14}$$

Appendix B

MRI model

B.1 MRI model

The model described in the following is based on the three parameters of atomic Mixing (w), surface roughness (σ) and information depth (λ) [58].

B.1.1 Atomic mixing: w

The mathematical description of the sputter profiling process is based on the simple approximation of atomic mixing to generate instantaneously a compositionally homogeneous zone of limited depth w by complete atomic redistribution. Assuming constant sputtering rate, we obtain the change of the concentration C with sputtered depth x: Mixing, roughness and information depth (MRI) method, which is utilized for correction of sputtering broadening, was developed by Hofmann [58]. Atomic mixing due to ion sputtering was considered as follows. Atomic mixing : w

$$\frac{dC(x)}{dx} = \frac{C^0(x+w) - C(x)}{w} \tag{B.1}$$

where $C^0(x+w)$ is the original, unaltered concentration at a distance w in front of the instantaneous surface at x.

B.1.2 Surface roughness : σ

In the most simple case, the surface roughness term can be approximated by an error function like distribution. It is taken into account by superposition of a normalized Gaussian function broadening as described by

$$C(x) = \frac{1}{\sqrt{2\pi}\sigma} \int_{x-3\sigma}^{x+3\sigma} C^0(x') exp\Big[\frac{-(x-x')^2}{2\sigma^2}\Big] dx' \tag{B.2}$$

where σ is the standard deviation.

B.1.3 Information depth : λ

In this work, the depth profiles were obtained by SIMS, therefore, there is no broadening due to the information depth. On the other hand, in AES or XPS profiling, the information depth is larger than the first monolayer and has to be taken into account by the usual exponential decay with the electron escape depth λ. For constant λ, a layer of thickness w contributes to the measured, normalized intensity I/I° by

$$\Big(\frac{I}{I^\circ}\Big)_t = C^t\Big[1 - \exp\Big(-\frac{w}{\lambda}\Big)\Big]. \tag{B.3}$$

Equation (B.3) is for the trailing edge while for the leading edge an additional contribution of the original layer beyond the distance $x + w$ from the surface has to be considered,

$$\Big(\frac{I}{I^\circ}\Big)_l = C^l\Big[1 - \exp\Big(-\frac{w}{\lambda}\Big)\Big] + \exp\Big(-\frac{w}{\lambda}\Big) C^\circ\Big[1 - \exp\Big(-\frac{x_2 - x - w}{\lambda}\Big)\Big]. \tag{B.4}$$

B.2 Deconvolution and convolution of profiles

Generally the true depth distribution of a profile can be obtained by calibrating the depth scale and the intensity scale, and then by deconvolution of the measured profile with an appropriate deconvolution function. It is often easier to assume a true profile and to convolute the profile with the resolution function and then to compare the obtained calculated profile with the measured profile.

For SIMS profiles, the parameter w, which is related to ion mixing, does not depend on the sample, but depends on the condition of SIMS measurement, i.e. the energy of primary ion beam, incident angle, etc. Therefore, with the same measurement condition, same value of w can be applied for MRI calculation. On the other hand, the parameter σ, which is related to the surface roughness, depends on the sample since the surface roughness of the sample is determined by the sample structure, the annealing condition, etc. Therefore, we determined the parameter σ from the AFM measurement of each sample.

In Fig. B.1, triangles are the SIMS profiles of ^{30}Si in the as grown simple isotope heterostructure. As we mentioned before, although the interface between $^{nat}SiO_2$ and

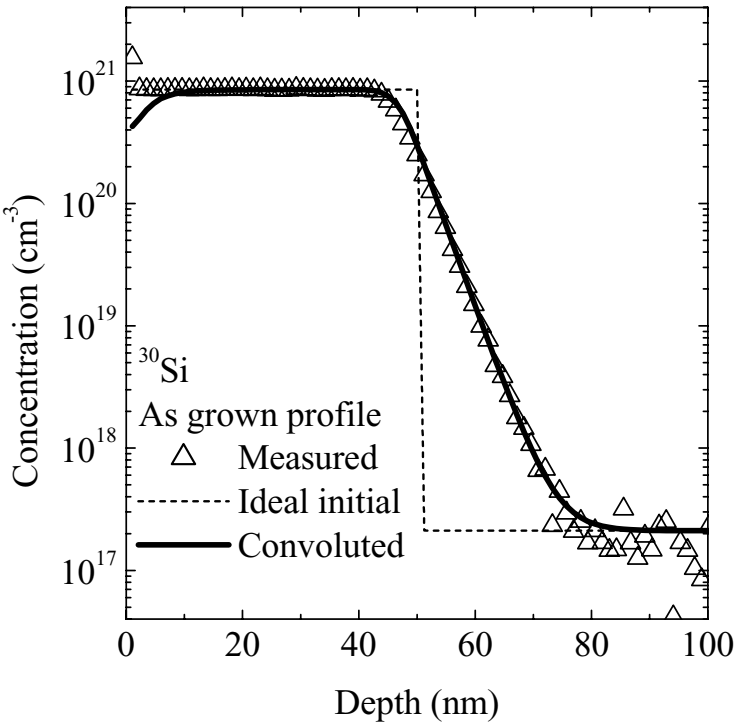

Figure B.1: Initial profiles obtained by SIMS and by MRI calculation. An ideal initial profile, which was used for MRI calculation, is also shown as dotted line. In this calculation, w=3.3 nm and σ= 1.6 nm were used.

$^{28}SiO_2$ is assumed to be abrupt, the profile is broadened at the interface due to atomic mixing. Convoluting the ideal initial profile shown as a dotted line in Fig. B.1, we fitted the calculated profile with the measured initial profile to obtain the parameter $w = 3.3$ nm, as a result, the convoluted profile using MRI calculation is good agreement with the measured initial profile as shown in Fig. B.1. As mentioned above, $w = 3.3$ nm can be used for all MRI calculation in this work since the same measurement condition was employed for all SIMS measurement in this work.

Bibliography

[1] A. I. Kingon, J. P. Maria and S. K. Streiffer: Nature **406**, 1032 (2000).

[2] H. Kageshima and K. Shiraishi: Phys. Rev. Lett. **81**, 5936 (1998).

[3] H. Kageshima, K. Shiraishi and M. Uematsu: Jpn. J. Appl. Phys. **38**, L971 (1999).

[4] M. Uematsu, H. Kageshima and K. Shiraishi: Jpn. J. Appl. Phys. **39**, L699 (2000).

[5] K. Suzuki, A. Satoh, T. Aoyama, I. Namura, F. Inoue, Y. Kataoka, Y. Tada and T. Sugii: J. Electrochem. Soc. **142**, 2786 (1995).

[6] T. Aoyama, K. Suzuki, H. Tashiro, Y. Tada and H. Arimoto: Tech. Dig. Int. Electron Devices Meet. IEDM-97 p. 627 (1997).

[7] M. Cao, P. Vande Voorde, M. Cox and W. Greene: IEEE Electron Device Lett. **19**, 291 (1998).

[8] Semiconductor Industry Association. *International Technology Roadmap for Semiconductors* 1999 edn http://www.itrs.net/ntrs/publntrs.nsf.

[9] T. Takahashi, S. Fukatsu, K. M. Itoh, M. Uematsu, A. Fujiwara, H. Kageshima, Y. Takahashi and K. Shiraishi: J. Appl. Phys. **93**, 3674 (2003).

[10] S. Fukatsu, T. Takahashi, K. M. Itoh, M. Uematsu, A. Fujiwara, H. Kageshima, Y. Takahashi and K. Shiraishi: Jpn. J. Appl. Phys. **42**, L1492 (2003).

[11] G. Brebec, R. Seguin, C. Sella, J. Bevenot, and J. C. Martin: Acta Metall. **28**, 327 (1980).

[12] O. Jaoul, F. Bejina, F. Elie and F. Abel: Phys. Rev. Lett. **74**, 2038 (1995).

[13] D. Mathiot, J. P. Schunck, M. Perego, M. Fanciulli, P. Normand, C. Tsamis and D. Tsoukalas: J. Appl. Phys. **94**, 2136 (2003).

[14] D. Tsoukalas, C. Tsamis and P. Normand: J. Appl. Phys. **89**, 7809 (2001).

[15] S. Fukatsu, T. Takahashi, K. M. Itoh, M. Uematsu, A. Fujiwara, H. Kageshima, Y. Takahashi, K. Shiraishi and U. Gösele: Appl. Phys. Lett. **83**, 3897 (2003).

[16] M. Uematsu, H. Kageshima, Y. Takahashi, S. Fukatsu, K. M. Itoh, K. Shiraishi and U. Gösele: Appl Phys Lett. **84**, 876 (2004).

[17] S. Fukatsu, K. M. Itoh, M. Uematsu, H. Kageshima, Y. Takahashi, and K. Shiraishi: Jpn. J. Appl. Phys. **43**, 7837 (2004).

[18] T. Aoyama, Y. Komatsu, K. Saito, S. Matsumoto, Y. Sato, I. Yamamoto and Y. Yamashita: Jpn. J. Appl. Lett. **39**, L955 (2000).

[19] T. Aoyama, K. Suzuki, H. Tashiro, Y. Toda, T. Yamazaki, K. Takahashi and T. Ito: J. Appl. Phys. **77**, 417 (1995).

[20] K. A. Ellis and R. A. Buhrman: Appl. Phys. Lett. **74**, 967 (1999).

[21] M. Otani, K. Shiraishi and A. Oshiyama: Phys. Rev. Lett. **90**, 075901 (2003).

[22] M. Otani, K. Shiraishi and A. Oshiyama: Phys. Rev. B **68**, 184112 (2003).

[23] M. Otani, K. Shiraishi and A. Oshiyama: Appl. Surf. Sci. **216**, 490 (2003).

[24] R. B. Fair: J. Electrochem. Soc. **144**, 708 (1997).

[25] R. B. Fair: IEEE Electron. Device Lett. **17**, 242 (1996).

[26] M. Uematsu, H. Kageshima, Y. Takahashi, S. Fukatsu, K. M. Itoh and K. Shiraishi: Appl. Phys. Lett. **85**, 221 (2004).

[27] M. Uematsu, H. Kageshima, Y. Takahashi, S. Fukatsu, K. M. Itoh and K. Shiraishi: J. Appl. Phys. **96**, 5513 (2004).

[28] R. E. Walkup and S. I. Raider: Appl. Phys. Lett. **53**, 888 (1988).

[29] J. Crank: *The Mathematics of Diffusion,* Second Edition, Oxford University Press (1975).

[30] P. Shewmon: *Diffusion in Solids,* Second Edition, The Minerals, Metals & Materials Society (1979).

[31] M. E. Glicksman: *Diffusion in Solids,* John Wiley & Sons, INC. (2000).

[32] P. M. Fahey, P. B. Griffin and J. D. Plummer: Rev. Mod. Phys. **61**, 289 (1989).

[33] U. M. Gösele: Ann. Rev. Mater.Sci. **18**, 257 (1988).

[34] U. Gösele, W. Frank and A. Seeger: Appl. Phys. **23**, 361 (1980).

[35] A. Ural, P. B. Griffin and J. D. Plummer: Phys. Rev. Lett. **406**, 1032 (2000).

[36] K. C. Pandey: Phys. Rev. Lett. **57**, 2287 (1986); A. Antonelli, S. Ismail-Beigi, E. Kaxiras and K. C. Pandey: Phys. Rev. B **53**, 1310 (1996).

[37] A. Ural, P. B. Griffin and J. D. Plummer: J. Appl. Phys. **85**, 6440 (1999).

[38] M. Uematsu: J. Appl. Phys. **82**, 2228 (1997).

[39] T. Y. Tan and U. Gösele: Appl. Phys. A, **37**, 1 (1985).

[40] P. Fahey, G. Barbuscia, M. Moslehi and R. W. Dutton: Appl. Phys. Lett. **46**, 784 (1985).

[41] W. Frank, U. Gösele, H. Mehrer and A. Seeger: in *Diffusion in Crystalline Solids*, edited by G. E. Murch and A. S. Nowick (Academic, New York, 1984), p. 63.

[42] A. Stesman and V. V. Affanas'ev: Phys. Rev. B **57**, 10030 (1998).

[43] C. R. Helms and E. H. Poindexter: Rep. Prog. Phys. **57**, 791 (1994).

[44] J. C. Mikkelsen: Appl. Phys. Lett. **45**, 1187 (1984).

[45] G. Roma, Y. Limoge and S. Baroni: Phys. Rev. Lett. **86**, 4564 (2001).

[46] I. J. R. Baumvol: Surf. Sci. Rep. **36**, 1 (1999).

[47] R. B. Fair: IEEE Electron. Device Lett. **20**, 466 (1999).

[48] K. Suzuki and R. Sudo: Solid-state Electronic **44** , 2253 (2000).

[49] B. E. Deal and A. S. Grove: J. Appl. Phys. **36**, 3770 (1965).

[50] A. M. Stoneham, C. R. M. Grovenor and A. Cerezo: Philos. Mag. B, **55**, 201 (1987).

[51] S. T. Dunham: J. Appl. Phys. **71**, 685 (1992).

[52] Y. Takakuwa, M. Nihei and N. Miyamoto: Appl. Surf. Sci. **117/118**, 141 (1997).

[53] D. Tsoukalas, C. Tsamis and J. Stoemenos: Appl. Phys. Lett. **63**, 3167 (1993).

[54] H. Bracht, E. E. Haller and R. Clark-Phelps: Phys. Rev. Lett. **81**, 393 (1998).

[55] H. D. Fuchs, W. Walukiewicz, E. E. Haller, W. Dondl, R. Schorer, G. Abstreiter, A. I. Rudnev, A. V. Tikhomirov and V. I. Ozhogin: Phys. Rev. B **51**, 16817 (1995).

[56] L. Wang, L. Hsu, E. E. Haller, J. W. Erickson, A. Fischer, K. Eberl and M. Cardona: Phys. Rev. Lett. **76**, 2342 (1996).

[57] L. Wang, J. A. Wolk, L. Hsu, E. E. Haller, J. W. Erickson, M. Cardona, T. Ruf, J. P. Silveira and F. Briones: Appl. Phys. Lett. **70**, 1831 (1997).

[58] S. Hofmann: Surface and Interface Analysis, **21**, 673 (1994).

[59] S. Hofmann and J. Schubert: J. Vac. Sci. Technol. A, **16**, 1096 (1998).

[60] G. K. Celler and L. E. Trimble: Appl. Phys. Lett. **54**, 1427 (1989).

[61] E. L. Williams: J. Am. Ceram. Soc. **48**, 190 (1965).

[62] R. Jaccodine: Mater. Res. Soc. Symp. Proc. **716**, 59 (2002).

[63] W. Orellana, A. J. R. da Silva and A. Fazzio: Phys. Rev. Lett. **87**, 155901 (2001).

[64] Y. -G. Jin and K. J. Chang: Phys. Rev. Lett. **86**, 1793 (2001).

[65] D. R. Hamann: Phys. Rev. Lett. **81**, 3447 (1998).

[66] A. M. Stoneham, M. A. Szymanski and A. L. Shluger: Phys. Rev. B **63**, 241304 (2001).

[67] D.-B. Kao, J. P. McVittle, W. D. Nix and K. C. Saraswat: IEEE Trans. Electron Devices **35**, 25 (1998).

[68] C. S. Rafferty: Ph.D. thesis, Stanford University, 1990.

[69] T. Uchida, M. Fujinaga, N. Kotani, S. Kawazu and H. Miyoshi: Jpn. J. Appl. Phys., Part 1 **35**, 4265 (1996).

[70] H. I. Liu, D. K. Biegelsen, N. M. Johnson, F. A. Ponce and R. F. W. Pease: J. Vac. Sci. Technol. B **11**, 2532 (1993).

[71] T. Y. Tan and U. Gösele: Appl. Phys. Lett. **40**, 616 (1982).

[72] Y. Kobayashi, Y. Shinoda and K. Sugii: Jpn. J. Appl. Phys. **29**, 1004 (1990).

[73] R. Tromp, G. W. Rubloff, P. Balk, F. K. LeGoues and E. J. van Loenen: Phys. Rev. Lett. **55**, 2232 (1985).

[74] M. Liehr, J. E. Lewis and G. W. Rubloff: J. Vac. Sci. Technol. A **5**, 1559 (1987).

[75] D. C. Streit and F. G. Allen: J. Appl. Phys. **61**, 2894 (1987).

[76] A. M. Agarwal and S. T. Dunham: J. Appl. Phys. **78**, 5313 (1995).

[77] H. Bracht, N. A. Stolwijk and H. Mehrer: Phys. Rev. B **52**, 16542 (1995).

[78] A. Stesman, B. Nouwen and V. V. Affanas'ev: Phys. Rev. B **66**, 045307 (2002).

[79] M. Tanaka, S. Saida, I. Mizushima, F. Inoue, M. Kojima, T. Tanaka, T. Nakanishi, K. Suguro and Y. Tsunashima: IEEE. Trans. Electron Dev. **49**, (2002) 1526.

[80] T. Aoyama, H. Tashiro and K. Suzuki: J. Electrochem. Soc. **146**, 1879 (1999).

[81] W. Jüngling, P. Pichler, S. Selberherr, E. Guerrero and H. W. Pötzel: IEEE Trans. Electron Devices **32**, 156 (1985).

[82] G. Charitat and A. Martinez: J. Appl. Phys. **55**, 2869 (1984).

[83] K. Muraoka: J. Appl. Phys. **96**, 2292 (2004).